PhD Thesis

Study of Phase Drift Compensation for RF Reference Distribution System at SuperKEKB Injector LINAC

SuperKEKB入射器における高周波基準分配システムの位相ドリフト補償に関する研究

Na LIU

DOCTOR OF PHILOSOPHY

Department of Accelerator Science

School of High Energy Accelerator Science

SOKENDAI

Tsukuba, 2019

Supervisor:	Prof. Takako Miura
Examiners:	Prof. Zhigao Fang
	Prof. Toshihiro Matsumoto
	Prof. Tetsuya Kobayashi
	Prof. Feng Qiu
	Prof. Hirokazu Maesaka
Day of Final Evaluation:	20th of August 2019
Day of Submission:	2nd of December 2019

For my family
and all who supported me for my Ph.D. work.

Abstract

The stabilization of radio-frequency (RF) reference phase for long distance transmissions is very important for stable machine operation, especially in large accelerator facilities such as SuperKEKB. This thesis is devoted to stabilizing the RF reference phase of the SuperKEKB injector linear accelerator (LINAC) for stable RF operation and compensating the phase drift between the LINAC master oscillator (LMO) and ring MO (RMO) for stable beam injection.

The injector LINAC comprises 600 m beam lines that have eight sectors (sector A-C,1-5). A 2856 MHz RF reference signal is distributed from the LINAC MO to each sector using phase-stabilized optical fiber (PSOF). The requirement of the RF reference phase stability is 0.2° (rms) at 2856 MHz corresponding to 195 fs, including the short-term timing jitter and long-term phase drift. The timing jitter was measured to be less than 150 fs (rms) such that the long-term phase drift is required to be stabilized within 100 fs (rms). The PSOF is distributed in the LINAC gallery, where the temperature is stabilized within ±1 °C using air conditioner but the humidity is not controlled, with a fluctuation from 10%RH to 50%RH during one year. Owing to temperature and humidity fluctuations, a phase drift of several degrees was observed during long transmissions (such as 380 m from LMO to sector 5) at the injector LINAC without phase regulation. To satisfy the requirement, several schemes of RF reference phase stabilization system using optic circulator or wavelength division multiplexing (WDM) devices were proposed and their performance were evaluated. The RF reference phase can be stabilized to the 50 fs (pk-pk) level, which fulfilled the requirement.

The injector LINAC that has a positron damping ring (DR) delivers low emittance electron and positron beams to the main rings. The beam injection phase from the LINAC to the rings should be stabilized to ±0.1° at 571.2 MHz for the long-term stable beam injection. The frequencies of LMO and RMO are 571.2 MHz and 508.9 MHz, respectively. These two different frequency signals are monitored using the direct sampling technique with a common sampling rate. A phase drift of several degrees was observed between the LMO and RMO. For stable beam injection, a phase drift compensation system is implemented at the LINAC. The system performance was evaluated through beam energy stability after the bunch compression system (BCS) from DR to LINAC (RTL).

Contents

Chapter 1

Introduction

1.1 SuperKEKB Injector LINAC

The SuperKEKB accelerator is a 7 GeV electron-4 GeV positron double-ring collider aiming at seeking new physics beyond the Standard Model. It has been upgraded from KEKB for a peak luminosity of $8 \times 10^{35} cm^{-2} s^{-1}$, which is 40 times higher than that of KEKB [1]. High-current and low-emittance beams are required in the SuperKEKB. As shown in Fig. 1.1, the SuperKEKB accelerator consists of a 7 GeV electron (e^-) ring (high-energy ring, HER), a 4 GeV positron (e^+) ring (low-energy ring, LER), and an injector linear accelerator (LINAC) with a 1.1 GeV positron damping ring (DR) [2]. The DR is designed and constructed to make the emittance of the injected positron beam small enough for the aperture of LER [3, 4]. The electron and positron beams collide at the interaction point and are detected using the Belle II detector [5].

The layout of the radio frequency (RF) drive system for injector LINAC is shown in Fig. 1.3. The J-shaped LINAC consists of straight lines with lengths 124.8 m and 488.3 m. They have eight sectors (sector A-C and 1-5). Sector A consists of two sub-harmonic bunchers (SHB): SHB1 operated at 114.24 MHz and SHB2 operated at 571.2 MHz, a pre-buncher, and a buncher operated at 2856 MHz (S-band) [6]. The other seven sectors are also operated at 2856 MHz as the regular accelerating sectors that comprise an amplifier, high-power klystron, pulse compressor (SLAC energy doubler, SLED [7]), and normal conducting accelerator structure, as shown in Fig. 1.2. In each sector, a 60 kW sub-booster klystron (SB) is installed as an amplifier to drive several klystrons (max. 8) as shown in Fig. 1.2(a). In some places, where the RF phase is required to be changed individually, a 600 W solid-state amplifier (SSA) is installed to drive one klystron, as shown in Fig. 1.2(b). A

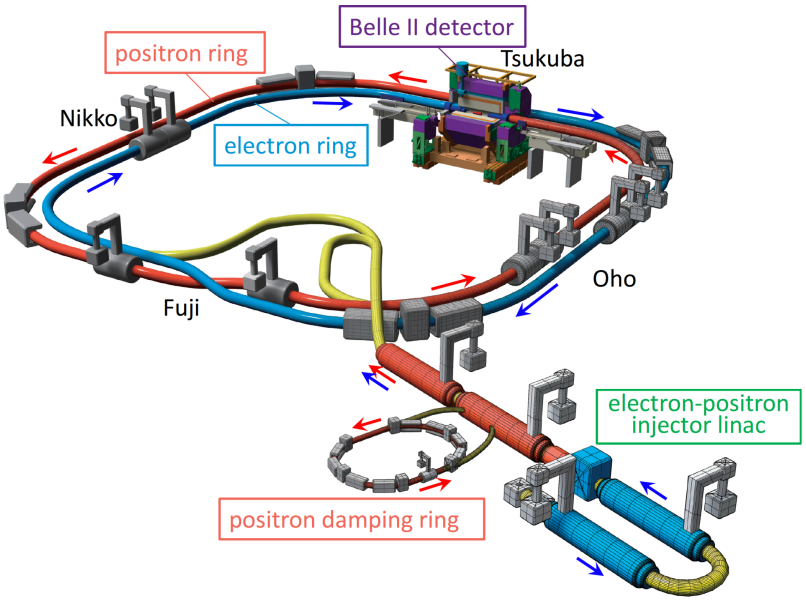

Figure 1.1: Layout of SuperKEKB facility.

40 MW klystron feeds the RF power to an accelerating unit, including four accelerating structures [8].

At injector LINAC, many devices are distributed along 600 m long beam lines for RF control, monitoring, and beam diagnostics. All distributed devices require a common timebase for stable beam operation. The LINAC master oscillator (LMO) is operated at 571.2 MHz, which is generated by a signal generator (Keysight, E8663DHY2). Three reference signals (114.24 MHz, 571.2 MHz, and 2856 MHz) are generated by the reference signal generator (RSG) based on LMO. The 114.24 MHz and 571.2 MHz reference signals are delivered to the bunching section by the coaxial cable. The 2856 MHz reference signals are distributed to each sector through phase-stabilized optical fiber (PSOF). In this system, there is no phase regulation for the RF reference signals between MO and each sector. The reference phase drifts due to the temperature and humidity fluctuations in the environment. Thus, the reference phase drift has a significant effect on the beam performance. Thus, the stabilization of the RF reference phase becomes a critical issue at injector LINAC.

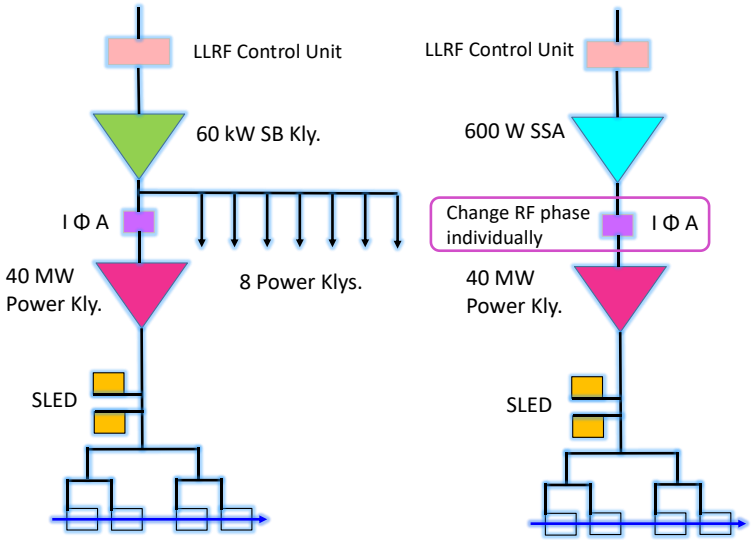

(a) SB klystron as an amplifier. (b) SSA as an amplifier.

Figure 1.2: Configuration of RF power driver for each accelerating unit.

1.2 Requirement of Phase Stability for RF Reference

In the SuperKEKB project upgraded from the KEKB facility, many components at injector LINAC have been upgraded for the low-emittance and high-current beam. The required injector beam parameters of KEKB and SuperKEKB are listed in Table 1.1 [9, 10]. For SuperKEKB, the requirement of energy spread at the end of injector LINAC is higher and a more stable reference phase is required. So far, the requirement for RF reference phase is not clear. In this section, the RF reference phase requirement is estimated based on the requirement of the electron energy spread (0.07%) at the end of injector LINAC.

Table 1.1: Required injector beam parameters of KEKB and SuperKEKB (final).

Stage	KEKB		SuperKEKB	
Beam	e+	e−	e+	e−
Energy	3.5 GeV	8.0 GeV	4.0 GeV	7.0 GeV
Energy Spread	0.125%	0.125%	0.16%	0.07%
Bunch Charge	1 nC	1 nC	4 nC	5 nC
No. of bunch / pulse	2	2	2	2
Repetition rate	50 Hz	50 Hz	50 Hz	50 Hz

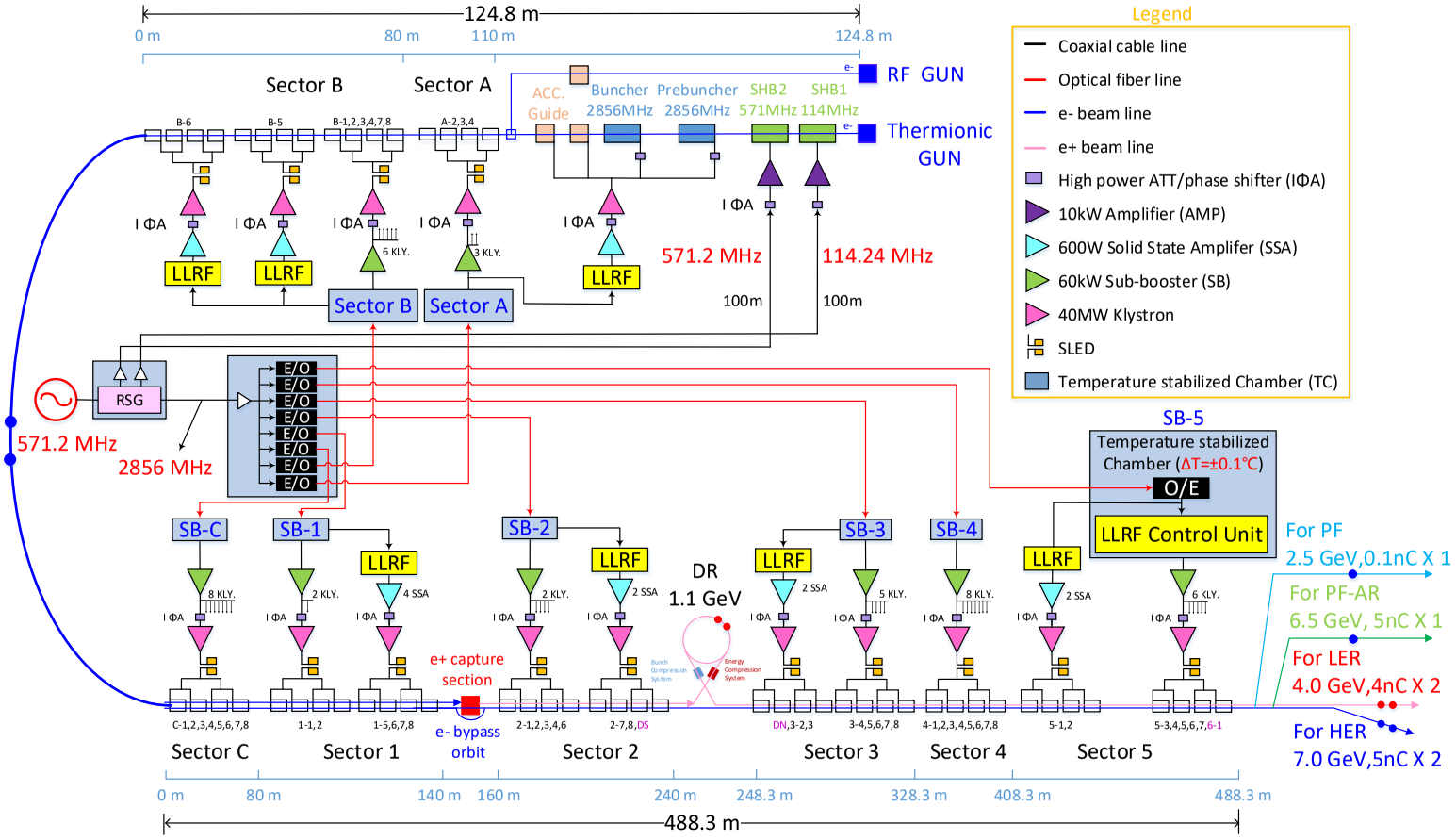

Figure 1.3: Layout of RF system for injector LINAC.

For the total energy spread (σ_{total}), the following main sources are considered: intra-bunch energy spread caused by wake-field (σ_{wake}), high voltage fluctuation in the klystron (σ_{khv}), low level RF (LLRF) control unit (σ_{llrf}), and RF reference phase (σ_{ref}). The total energy spread should be less than 0.07%. The RF reference phase requirement can be calculated as

$$\sigma_{ref} = \sqrt{\sigma_{total}^2 - \sigma_{wake}^2 - \sigma_{khv}^2 - \sigma_{llrf}^2} \tag{1.1}$$

- Intra-bunch energy spread caused by wake-field

  The longitudinal wake-field causes an energy spread within a bunch as well as a decrease in the average energy, depending on the bunch length (BL) and acceleration beam phase [11]. To estimate the effects of the longitudinal wake-field, formulas with several beam parameters were obtained in [12]. The rectangular beam with 4 nC bunch charge will be accelerated in the near future. Accordingly, the energy spread caused by the bunch length and acceleration beam phase is calculated in Fig. 1.4. The optimum bunch length and acceleration beam phase are 7.34 ps and $-10°$ off-crest, respectively. The energy spread was evaluated to be 0.0223% (rms).

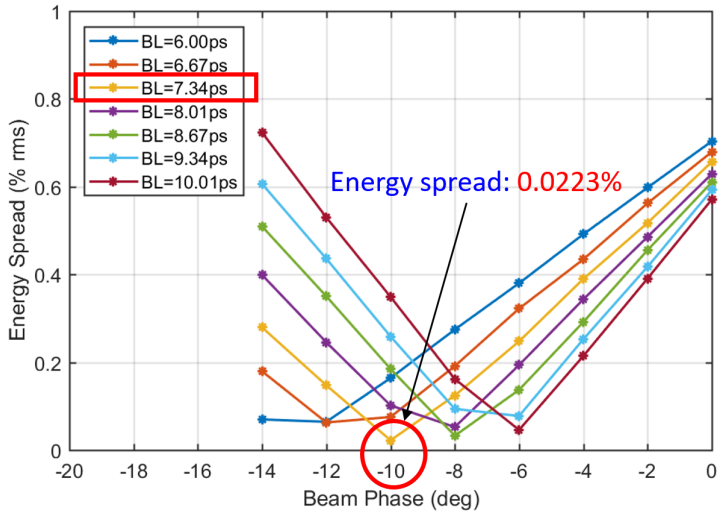

Figure 1.4: Relation between beam phase and energy spread for each length of rectangular bunch shape.

- High voltage fluctuation of the klystron

The klystron high voltage fluctuation ($\frac{\Delta V}{V}$) is 0.05% (rms). The RF field error caused by the high voltage fluctuation per klystron can be calculated as

$$\frac{\Delta A}{A} = \frac{5}{4} \cdot \frac{\Delta V}{V} = 0.0632\% \tag{1.2}$$

$$\Delta\theta = -\frac{4}{\%} \cdot \frac{\Delta V}{V} = -0.2^\circ \tag{1.3}$$

where $\frac{\Delta A}{A}$ and $\Delta\theta$ are the amplitude error and phase error of the RF field, respectively.

The energy spread is estimated to be 0.088% (rms) at -10° off-crest. In the injector LINAC, there are 50 klystrons for electron. Assuming that the power supplies are uncorrelated, the uncorrelated energy spread caused by the klystron high-voltage fluctuation is compressed to 0.0124% by $1/\sqrt{N}$ (N is the number of klystrons).

- LLRF control unit

  The RF operation point is located at the RF saturation point of the klystron to ensure that the RF field is insensitive to the amplitude error. Only the phase error is considered here. There is no feedback control to the RF filed due to the short pulse beam. The phase stability of the LLRF control unit is 0.1° (rms). The energy spread due to the LLRF control unit is 0.031% (rms). The LLRF control unit is located at each sector and there are eight sectors for the electron beam. The uncorrelated energy spread caused by the LLRF control unit is compressed to 0.011% by $1/\sqrt{8}$.

Thus, the requirement of the RF reference phase is estimated as

$$\sigma_{ref} = \sqrt{0.07\%^2 - 0.0223\%^2 - 0.0124\%^2 - 0.011\%^2} = 0.0642\%$$

Assuming that the amplitude and phase error are in Gaussian distribution, the influence of small correlated amplitude and phase error on the energy spread is given by the formula [13]

$$\sigma_{total} = \frac{1}{\cos\phi_b}\sqrt{\frac{1}{2}(1+\cos 2\phi_b)(\frac{\sigma_A}{A}^2) + \frac{1}{2}(1-\cos 2\phi_b)\sigma_\phi^2 + \frac{1}{4}(3\cos 2\phi_b - 1)\sigma_\phi^4} \tag{1.4}$$

where ϕ_b is the optimum acceleration beam, $\frac{\sigma_A}{A}$ is the relative amplitude error in rms, and σ_ϕ is the phase error in rms.

The amplitude error and phase error of the RF reference signal can be evaluated according to the required energy spread (0.0642%), as shown in Fig. 1.5. The amplitude is insensitive to the energy spread, thus, the reference phase requirement is up to 0.2° corresponding to 195 fs (rms) at 2856 MHz, including the short-term timing jitter and long-term phase drift over days. The timing jitter is less than 150 fs (rms) (see Section 3.1), therefore, the required long-term phase drift is less than 100 fs (rms) at 2856 MHz.

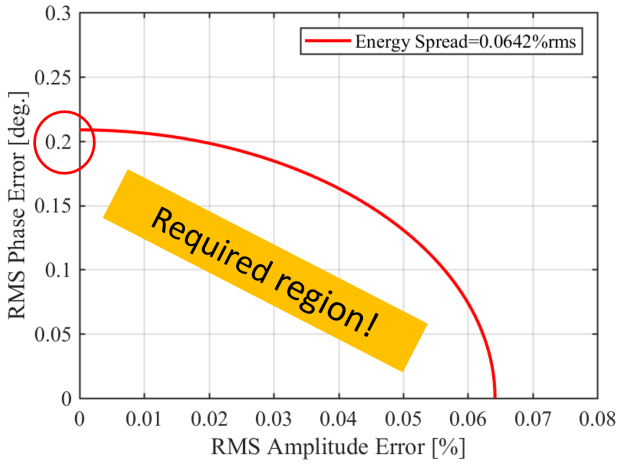

Figure 1.5: Amplitude error and phase error of the RF reference signal with the energy spread requirement of 0.0642%.

1.3 Motivation of this Study

The goal of this thesis is to stabilize the RF reference phase for SuperKEKB injector LINAC and compensate the phase drift between LINAC MO and ring MO for stable beam injection.

First, the delivery of a stable RF phase reference over optical fiber from MO to each sector at the SuperKEKB injector LINAC is dealt with. A special optical fiber, called phase stabilized optical fiber, is used to deliver the reference signal at injector LINAC and its thermal propagation time delay is as low as 5 ps/km/°C. The PSOF is distributed in the LINAC gallery where the temperature is stabilized within ±1 °C using air conditioner but the humidity is not controlled. The reference signal suffers a phase drift during long transmissions. In the case of 380 m PSOF from MO to sector 5, the

2° phase drift at 2856 MHz is caused by the ±1 °C temperature fluctuation. Furthermore, humidity also contributes to the reference phase drift. This phase drift cannot fulfill the requirement of 0.1° (rms) at 2856 MHz.

First, the reference phase drift should be measured at the LINAC gallery. The causes of this phase drift, such as the temperature and humidity dependency, should be analyzed. To estimate the phase drift, the temperature and humidity coefficients of the optical components (e.g., PSOF) should be measured. Finally, a RF reference phase stabilization system should be proposed to fulfill the requirement. Several techniques or designs have been developed that can fulfill the given stability requirements. However, they are relatively complex and often use some self-built components, which are not available commercially. This makes the stabilization system very expensive and difficult to implement. A new phase stabilization system should be specific to the current system at injector LINAC. It should be simpler to implement and have low cost using commercial components. A reference phase stabilization system using optic circulator and the wavelength division multiplexing (WDM) technique was implemented in the test hall and its performance was evaluated. In this case, the transmitted reference phase stability was observed using a phase monitor system with high precision. Some methods were implemented to reject the phase drift in the monitoring system.

Second, the phase drift between LMO and RMO should to compensated. The injector LINAC that includes the positron DR delivers low-emittance electron and positron beams to the main rings. The LMO is operated at 571.2 MHz and located in the LINAC gallery. The DR MO and MR MO are operated at 508.9 MHz and located in the SuperKEKB control room, which is several hundred meters away from LINAC gallery. The LMO, DR MO, and MR MO are synchronized with the 10 MHz trigger. The DR MO and MR MO (collectively called RMO) are phase locked within ±0.1° at 508.9 MHz; however, the LMO and RMO are not phase regulated. This MO phase drift significantly affected the beam energy stability after the bunch compression system from LINAC to DR and beam injection phase tuning from LINAC to MR had to be conducted frequently, because the beam injection background has been a critical problem for the SuperKEKB Belle II detector. To maintain a stable beam injection, an MO phase drift compensation system was developed. The phase stability between LMO and RMO was required to be less than ±0.1° in peak to peak (pk-pk) at 571.2 MHz.

1.4 Structure of Thesis

The thesis consists of eight chapters. A brief introduction to each chapter is given below.

- Chapter 2 gives an overview of the RF reference distribution system for different large facilities in operation. The RF reference distribution over the optical link and coaxial cable are introduced. The schematic design and long-term performance are summarized.
- Chapter 3 details the measurement result of the phase noise and phase drift in the RF reference signal at each sector. A new phase monitor using the oversampling technique is implemented and the contribution of phase drift is analyzed.
- Chapter 4 discusses the causes of phase drift (e.g., temperature, humidity). A test system is constructed to measure the temperature and humidity coefficients of the RF components.
- Chapter 5 describes the phase drift of the monitoring system and its causes. Three methods (two-tone calibration, drift compensation module, and reference tracking) are introduced to suppress the system phase drift and their long-term performances are compared.
- Chapter 6 demonstrates the different schemes of the RF reference phase stabilization system using the WDM technique and optic circulator. The schematic design and long-term performance is shown.
- Chapter 7 illustrates the principle of the direct sampling technique and implementation of the phase drift compensation system for stable beam injection. The long-term performance is evaluated using the beam energy stability at DR.
- Chapter 8 summarizes the thesis and proposes the possible configuration of the RF reference phase stabilization system for the SuperKEKB injector LINAC.

Chapter 2

Overview of RF Reference Distribution System

Several techniques have been implemented to send stable reference signals over optical fiber with average uncertainties of several hundred femtoseconds to under 10 fs [14, 15, 16, 17, 18, 20]. The phase stabilization system over the coaxial cable has been demonstrated [21, 22, 23, 24]. Next, we provide an overview of the SuperKEKB ring, SPring-8 Angstrom compact laser (SACLA), and European X-Ray free-electron laser (XFEL). Those RF reference distribution systems were implemented with different techniques and are currently being operated at the facilities.

2.1 RF Reference Distribution at SuperKEKB Ring

The SuperKEKB main ring is a storage ring that consists of a HER for electrons and LER for positrons, and each ring has a circumference of 3016 m. The accelerating frequency of MR is 508.9 MHz with continuous wave (CW) operation. The requirement of the RF referenec phase is $\pm 0.3^\circ$ (pk-pk) at 508.9 MHz [14]. However, the target of the RF reference phase stability is $\pm 0.1^\circ$ (pk-pk). The RF reference is distributed in a star topology from the MR MO to seven RF stations and DR optically by PSOF with a maximum distance up to 2 km. Over long distance transmission, the reference phase drifts of the optical link owing to the effects of temperature and humidity.

A reference phase stabilization system with the WDM technique was implemented to compensate the slow drift of each transmission line. This stabilization method was established in [16, 17] and successfully applied at the SuperKEKB MR [14]. The 508.9 MHz reference signal is generated by the

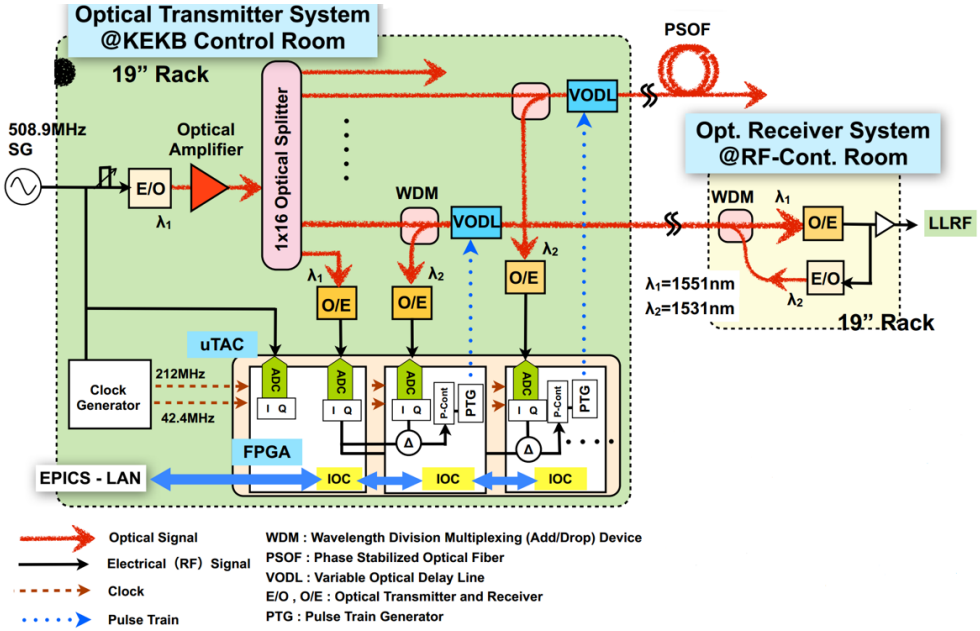

Figure 2.1: RF reference phase stabilization system for SuperKEKB MR [14].

signal generator (SG) and converted to the optical signal with a wavelength of 1551 nm using an electrical/optical converter (E/O). The optical signal is amplified and fed into a 16-channel optical splitter. The split optical signals are distributed to different locations and received by an optical/electrical converter (O/E) as the reference to the LLRF system at the receiver side. To measure the phase drift of the optical link over long distance transmission, two WDM devices with wavelengths of 1551 nm and 1531 nm are installed. The transmitted electrical signal is converted to the optical signal by another E/O with 1531 nm wavelength, which is different from 1531 nm in the forward path. This optical signal is transmitted to the transmitter side by WDM and converted to the electrical signal again by another O/E at the transmitter side, as shown in Fig. 2.2(a). The O/E with peltier for stable temperature and the WDM device are assembled into a module based on the nuclear instrument module (NIM) standard. By using the WDM technique, the forward and backward optical signals with wavelengths of 1531 nm and 1551 nm, respectively, can be multiplexed and transmitted over the same optical fiber. The returned signal experiences the round-way optical paths, thereby doubling the phase drift.

To reduce the monitor system phase drift, the RF phase is detected using the direct sampling method based on a filed programmable gate array

(FPGA) board [26]. In this method, the RF signal is directly measured using an analog-to-digital converter (ADC) without the down-conversion stage to reduce the long-term measurement error of the monitor system. Furthermore, the transmitter and receiver systems are placed in the 19-inch rack where the temperature is controlled within ±0.1 °C by air conditioner. The RF phase is calculated by the *in-phase* component (I) and *quadrature-phase* component (Q). The measurement error can also be reduced by the averaging effect of the IQ algorithm. The direct sampling method with non-IQ detection is explained in Section 7.2. In the case of SuperKEKB ring, the 508.9 MHz RF signal is directly measured by a 14-bit ADC (ADS5474, 400 MSPS speed, 1.4 GHz bandwidth) with a sampling clock (212 MHz). To improve the phase stability, an infinite impulse response (IIR) low-pass filter (LPF) is applied. Phase drift is observed in the optical link with round-trip paths.

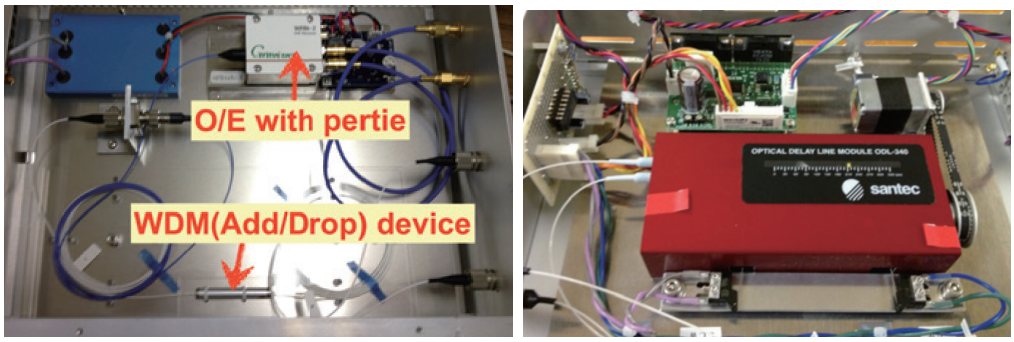

(a) NIM module: O/E with peltier for stable temperature and the WDM device.

(b) VODL (Santec Corp., ODL-340) driven by a stepping motor, equipped with two position limit switches.

Figure 2.2: Optical devices used in the phase stabilization system of SuperKEKB ring [14].

The PSOF is located in the tunnel and the temperature fluctuation is ±5 °C during one year. According to the temperature coefficient of PSOF (< 1 ppm/°C) [25], the returned phase drift is as large as ±9° over a transmission of 2 km. To compensate the slow phase drift caused by temperature and humidity fluctuations, a wide-range variable optical delay line (VODL) is used. The delay range is up to 340 ps corresponding to 62° phase range at 508.9 MHz. This VODL is driven by a stepping motor, as shown in Fig. 2.2(b). According to the measured phase drift with the round-trip path, the pulse train is sent to the stepping motor to adjust the optical path length to ensure that the phase drift is compensated.

A 100 m normal optical fiber with a thermal coefficient of 1.7°/100 m/°C is

tested in the laboratory. The feedback system is installed and the transmitted phase is monitored by a vector volt meter (VVM), as shown in Fig. 2.3. The temperature is changed from 40 °C to 10 °C and up to 40 °C. With the feedback, 0.2° phase jump was found between 20 °C and 30 °C, as shown in Fig. 2.3(a). After optimizing the working position of the VODL, the delay-offset is avoided. Finally, a stability of ±0.1° (pk-pk) at 508.9 MHz was obtained, which fulfilled the requirement, as shown in Fig. 2.3(b).

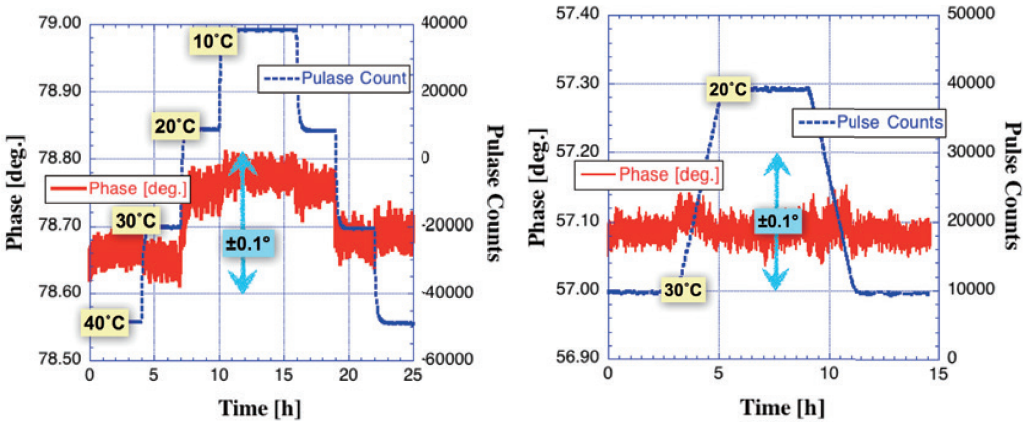

Figure 2.3: Transmitted phase stability at SuperKEKB ring [14].
(a) Transmitted phase measured by VVM (red solid line), pulse count of the stepping motor to move the VODL (blue dashed line), with the VODL control.
(b) Transmitted phase stability with the same measurement setup but the position of the VODL was optimized to avoid the delay-offset.

2.2 Optical Timing and RF Reference Distribution System at SACLA

SACLA is a facility of XFEL for generating coherent X-rays with a peak power of more than 10 GW and a very short pulse below 30 fs [27]. Usually, the pump-probe experiments require synchronization between the pulsed lasers and the RF accelerating fields. The timing stability of such synchronization is required to be 50 fs throughout the 700 m long SACLA facility [18]. A 5712 MHz RF reference signal is generated by an MO and distributed to each acceleration component by PSOF with a propagation time delay as low as 5 ps/km/K. To minimize the phase drift in the PSOF due to environment change, these PSOFs are situated in the water-cooled thermal ducts

with regulated temperature within 0.4 °C (pk-pk). All electronics are also enclosed in the water-cooled 19-inch racks with regulated temperature within 0.4 °C (pk-pk). A timing drift of more than 100 fs has been observed by many instruments at SACLA. To achieve the required timing stability of 50 fs, an RF reference phase stabilization system using a wavelength region of 1550 nm was developed to mitigate the environmental effects on the optical links, such as temperature and humidity changes.

To compensate the phase drift, the OptRef system using the Michelson interferometry method [28] was developed, as shown in Fig. 2.4. This system uses two length standards for two optical length control loops. One is the coarse length control loop based on the wavelength of a 91.4 GHz RF signal, which is the difference between two optical wavelength signals of 1552.15 nm and 1552.89 nm. It has a wide dynamic range of 3.3 mm corresponding to 11 ps. The other is the fine length control loop based on an optical wavelength of 1548.96 nm, with a narrow dynamic range of 1.5 µm corresponding to 5 fs [18, 27]. In the coarse control loop, an external cavity laser diode (ECLD) generates a reference light of 1552.52 nm, further modulated by a 45.7 GHz RF signal, which is generate by 8 times of 5712 MHz signal, to get two side-band light beams ($\lambda_+ = 1552.15$ nm and $\lambda_- = 1552.89$ nm). The frequency difference between them is 91.4 GHz (millimeter wave). In the fine control loop, a frequency stabilized laser generates the reference light with a wavelength of 1548.96 nm (193 THz).

The procedure of measuring the phase drift in the PSOF is as follows. The lights are split into two parts: one part is modulated by an acoustic optical modulator (AOM) with 238 MHz as reference light, the other passes through a polarization beam splitter (PBS) and piezo-driven fiber stretchers (PDFS), and are then fed into the PSOF for transmission. This transmitted optical signal is reflected back by a Faraday rotating mirror (FRM) at the remote station, with an orthogonal polarization with respect to the forward reference light. In the interferometer, the reference and reflected lights are mixed using an optical coupler. The optical signals with different length standards are separated by a band-pass filter (BPF) and detected using a photo-diode (PD). A 238 MHz beat signal is obtained from the PD as an interferometry signal. The optical phase of the fine loop is reproduced as the phase difference between the beat signal and the AOM input signal from MO. The phase of the millimeter-wave signal in the coarse loop is detected by comparing the phases of the PD signals from the two optical signals, f_+ and f_-. The phase of the 238 MHz beat signal is detected using a phase frequency discriminator (PFD). The detected phase is fed into each optical fiber stretcher to stabilize the optical length of the PSOF. A proportional–integral–derivative (PID) controller is applied for precise control.

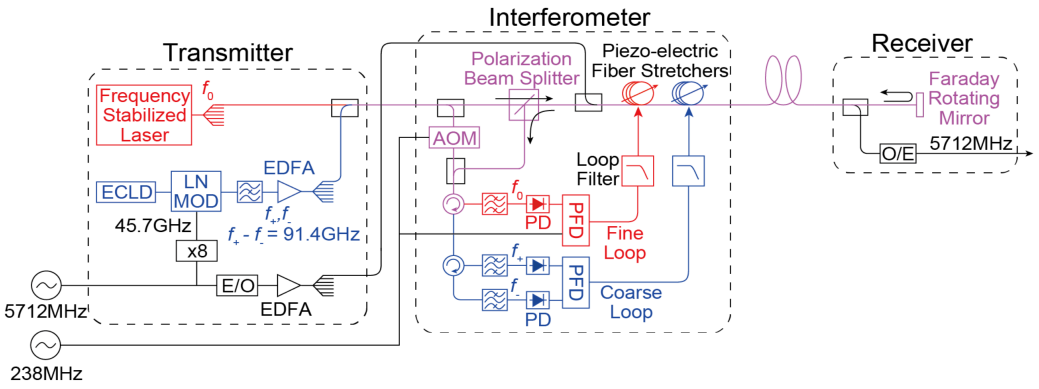

Figure 2.4: Block diagram of the optical fiber length stabilization system with interferometer, including a coarse length control and fine length control subsystems [18].

A 5712 MHz RF signal is converted to the optical signal by E/O and transmitted through the OptRef system with stable phase. This optical signal is converted to the electrical signal and sent to a phase detector. The output signal (5712 MHz) of the optical RF receiver is also sent to the phase detector. The detected phase drift is used to drive a piezo-electric fiber stretcher before the receiver. The optical length drift is compensated by this stretcher and a very precise stable reference is obtained for the RfRef system.

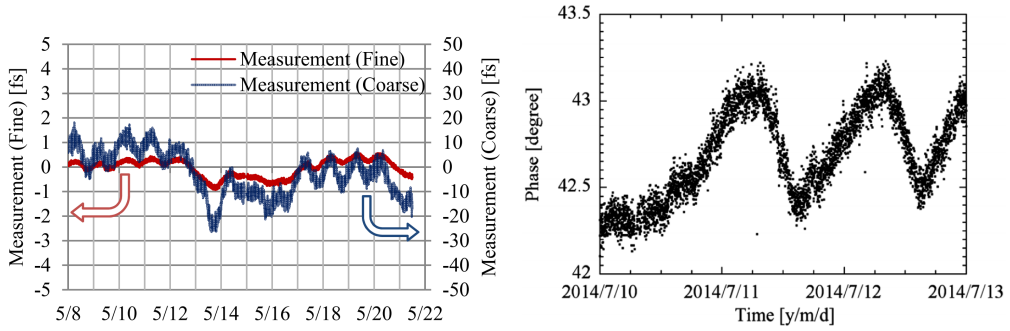

(a) Timing stability of the RF reference for 400 m long PSOF [18].

(b) Beam arrival time drift at the end part of beam line 3 [19].

Figure 2.5: Long-term performance of the RF reference and the beam arrival time drift at beam line 3.

Figure 2.5 represents the long-term timing stability of the RF reference system and the beam arrival time drift at the experimental hall. Figure 2.5(a) shows the performance of 400 m PSOF regulation. Only the fine feedback

loop is applied and the coarse loop is used as a monitor. The timing stability detected by the fine loop is suppressed within 2 fs for two weeks. However, the timing stability detected by the coarse loop is 50 fs (pk-pk). Thus, we can conclude that the timing stability of the RF reference can achieve an accuracy of 50 fs with several hundreds meters long PSOF. In Fig. 2.5(b), the beam arrival time drift is observed at beam line 3 in the experimental hall. The drift is less than 1° at 4760 MHz for three days corresponding to 580 fs. These data include the long-term drift of the timing system, the LLRF system, and the beam position monitor (BPM) detection circuit.

2.3 RF Reference Distribution at European XFEL

Future accelerators require high accuracy reference signal to synchronize the RF stations and experimental devices over long distance, especially for the free-electron laser (XFEL). The European XFEL [29] was constructed at Deutsches Elektronen-Synchrotron (DESY) and consists of an injector, a booster, the main LINAC, undulators, and photon beam lines with the length of 3.3 km. There are $\sim$ 30 RF stations (RFS) and 32 cavities in each RF station. A very stable 1.3 GHz phase reference signal has to be distributed to each RF station and several thousands of RF and optical devices should be synchronized, such as the LLRF system at each RF station, BPMs at the undulator, and photon beam lines. The required phase stability at 1.3 GHz for each location is listed in Table 2.1. It requires an extremely stable phase and time synchronization. Most critical subsystems are located in the injector area with high requirements of 10 fs for short-term and 100 fs for long-term. The synchronization requirement between X-ray and pump-probe laser is 60 fs and 10 fs point-to-point [22].

Table 2.1: Phase stability requirement at 1.3 GHz for European XFEL [22].

Location	**Short-term**	**Long-term**
Injector	10 fs	100 fs
Booster (L1,L2)	30 fs	300 fs
Main LINACS (L3)	100 fs	<1 ps
Cavity BPM	60 fs	not specified
Reentrant BPM	5.8 ps	<10 ps

Figure 2.6 shows a simplified layout of the RF reference distribution for synchronization. The synchronization system consists of four subsystems:

the RF MO system, optical synchronization system with the master laser oscillator (MLO), RF phase reference distribution system (PRDS), and the timing distribution system [22]. All systems are synchronized and phase locked to the RF MO. The MLO distributes the reference signal using the optical link with a stability of less than 10 fs. Owing to the high cost of such a system, femtosecond stable optical links are only limited to the most phase critical accelerating sections, arrival time diagnostics, and optical lasers such as the photo-injector laser and the pump-probe laser. In each remote location, a laser-to-RF (L2RF) module [31] is developed as a precise phase detector to synchronize the RF signal to the optical pulses. Due to the complexity of this optical stabilization system, high reliability cannot be guaranteed. Therefore, RF coaxial cable distribution with interferometer is redundantly used in the most critical subsystems with a short-term jitter of sub-100 fs and long-term drift of sub-1 ps. The same coaxial cable distribution system with interferometer is also utilized in local distribution with two different RFs (1.3 GHz for injector and booster, 216 MHz for main LINAC).

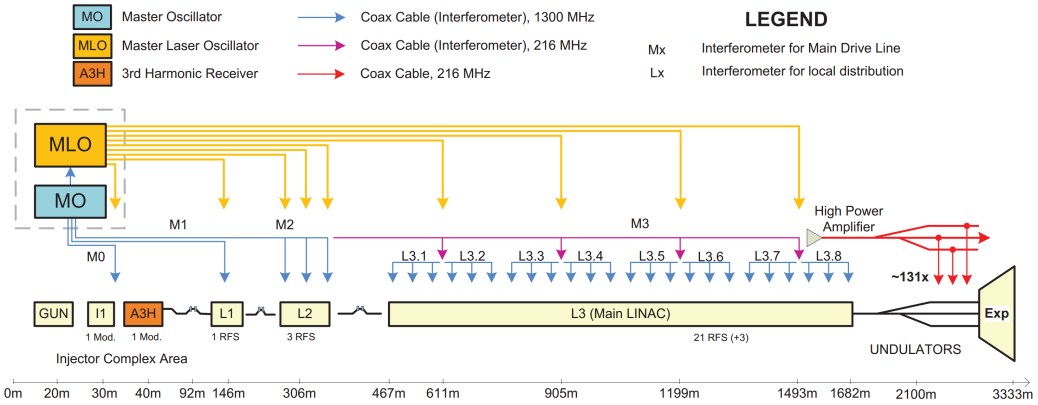

Figure 2.6: Simplified layout of the RF phase reference distribution system for European XFEL [22].

2.3.1 Optical Link-based Distribution

Laser based synchronization systems are based on the stabilized short pulse MLO to deliver the pulse trains with femtosecond accuracy [30]. Figure 2.7 shows the simplified diagram of the laser synchronization scheme. The MLO is synchronized and phase locked to the RF MO. The reference light is split into several channels by free-space distribution (FSD). The reference phase of each channel is stabilized by the link stabilization unit (LSU). The output

of LSU is used as a reference for the bunch-arrival-time monitors, L2RF stations, and laser-to-laser synchronization modules. All optical components are located in a humidity- and temperature-stabilized synchronization room to minimize the system phase drift.

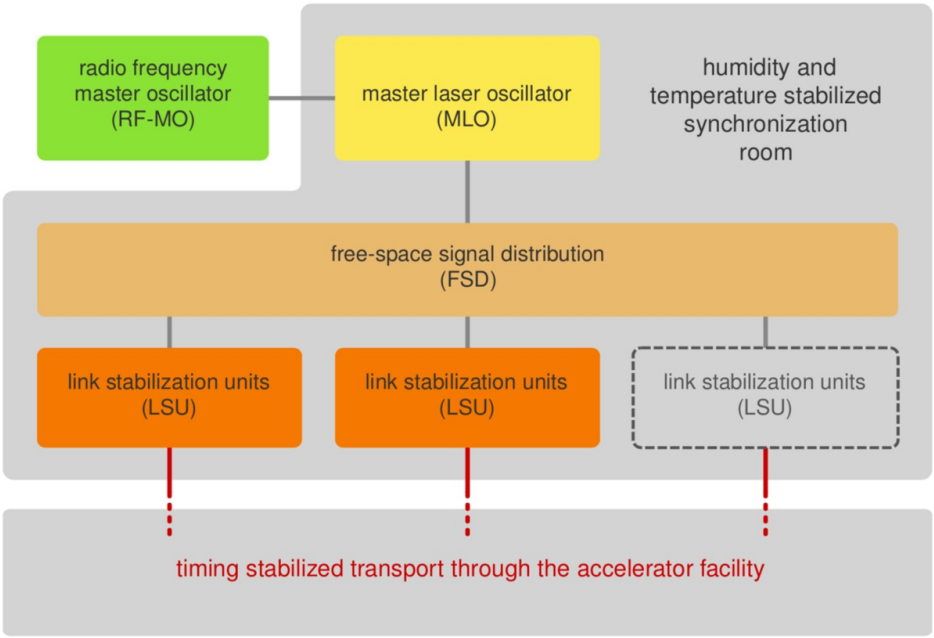

Figure 2.7: Laser synchronization scheme [30].

Figure 2.8 shows the optical phase stabilization with LSU. The polarized light from MLO is split into two: the coupled portion is used as the reference light and the main portion is used for transmission. The reference light in one direction (red line) is distributed through a long polarization-maintaining (PM) optical fiber to the far-end station. Part of the light is reflected back to LSU by a semitransparent mirror in the orthogonal direction (green line) with respect to the reference light. The remaining light is delivered as a stable reference to the synchronize stations. The reflected light and the reference light coupled at the LSU are compared using a balanced optical cross-correlator (OXC). This signal is used to compensate the phase drift of the long PM fiber. To control the optical length, a self-built optical delay line (ODL) is used for coarse control with a wide dynamic range of 4 ns and a piezo-driven fiber stretcher is used for fine control with a narrow dynamic range of 3.5 ps but high resolution. A spool of matched dispersion-compensating fiber is also used.

Figure 2.9 shows long-term stability with the out-loop measurement at

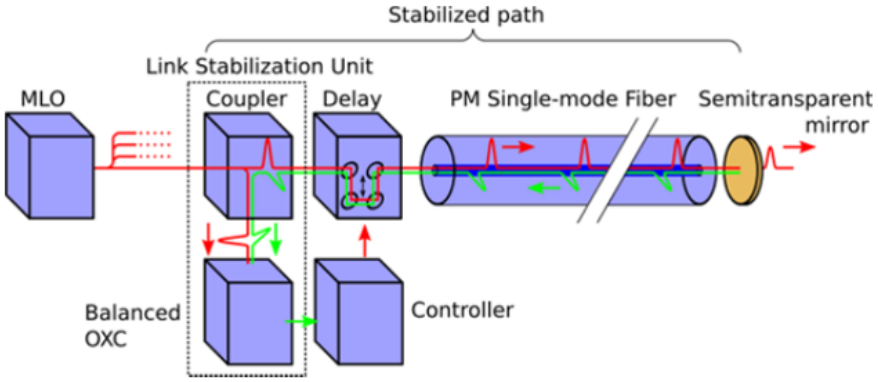

Figure 2.8: Optical phase stabilization with LSU [30].

the European XFEL [32]. The temperature fluctuation was 1 °C (pk-pk) and the phase drift of the optical link was observed to be 200 ps. With LSU compensation, the timing jitter was less than 500 attoseconds and the slow drift was less than 3.3 fs (filtered raw data) for 24 hours.

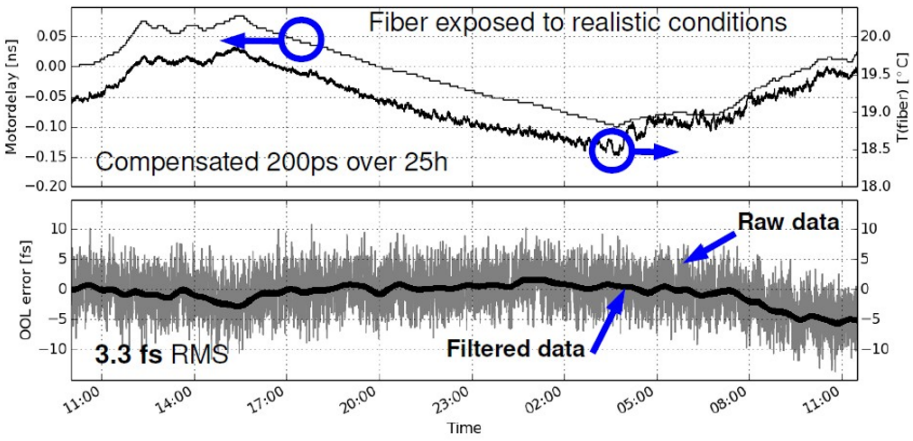

Figure 2.9: Long-term stability with out-loop measurement at European XFEL [32].

2.3.2 Coaxial Cable-based Distribution

Beside optical fiber, coaxial cables are commonly used to distribute the reference signal over a large facility to synchronize electronic systems. The PRDS based on the coaxial cable is used to distribute the stable reference of European XFEL at both remote and local location. The most challenging task is to overcome the phase drifts in the long cable due to the environmental effect and power loss during long transmission.

The original idea of the phase averaging reference line (PARL) design concept was proposed by J. Frisch, D. Brown, and E. Cisneros in [21]. The schematic diagram of PARL for NLC is shown in Fig. 2.10. The RF reference signal is phase locked to the RF MO through the optical stabilization system. At each station, where a stable reference phase is required, the coupled forward and backward signals are combined. The average of the forward and backward phase should not depend on the phase changes caused by the changes in the length of the coaxial cable. However, the reflections from the directional couplers degrade the accuracy of system, which has not yet been calculated.

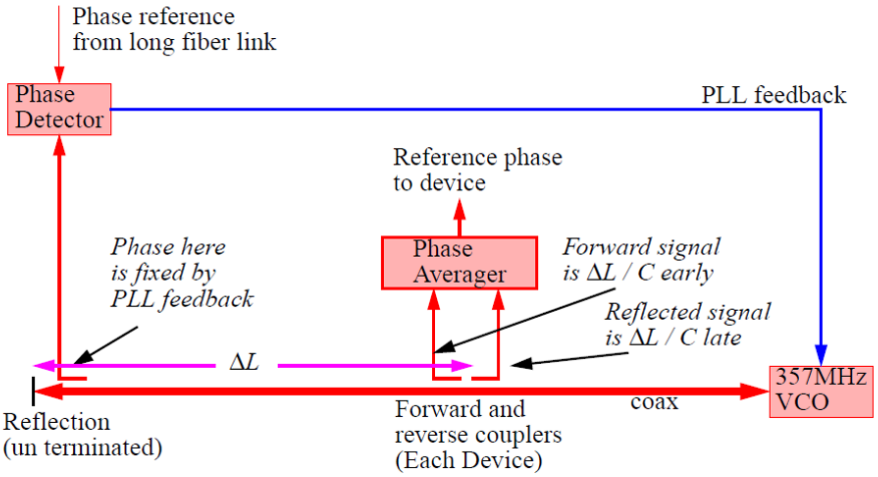

Figure 2.10: Orignal idea of the phase averaging reference line design concept for Next Linear Collider (NLC) [21].

This study was continued by Brian Chase and Ed Cullerton in [33, 34, 35, 36]. Figure 2.11 shows the 1.3 GHz phase averaging reference line for the Fermilab superconductiong RF beam test facility. It consists of directional couplers and coaxial cables. The reference line is shorted at the end of the line to provide reflected signal for phase average. At each directional coupler,

the coupled forward and backward signals are summed by a combiner. To minimize the impedance mismatches between the directional coupler and the coaxial cable, a 3 dB attenuator and a variable attenuator are inserted in the forward and backward lines, respectively. Simulation were conducted to verify the design procedure. The performance of the reference line are limited by two key factors:

- Impedance mismatches between the directional coupler and the coaxial line

  The cable length between the directional couplers should be carefully adjusted such that the averaged signals are on a peak of the phase ripple caused by the reflections and impedance mismatches.

- Phase drifts in the combiner circuit

  The combiner circuit consists of a directional coupler, a power combiner, a 3 dB attenuator, and a variable attenuator. Careful selection for the critical parameter and proper arrangement of each component are requested.

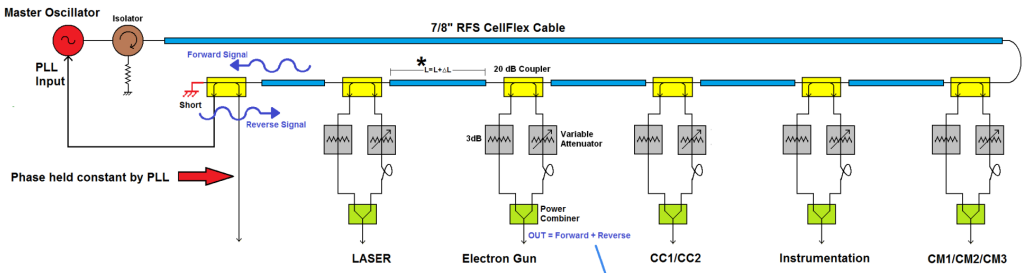

Figure 2.11: 1.3 GHz phase averaging reference line for Fermilab superconductiong RF (SRF) beam test facility [36].

It demonstrated that the phase drift of the long coaxial cable can be significantly suppressed. The long-term RF reference phase stability at one tap point of the Fermilab SRF beam test facility achieved 150 fs (pk-pk) in [35]. The performance was limited by the power loss in the cable and the isolation of the coupler. The main disadvantage [37] of the concept is

- The cable length has to be adjusted manually between the adjacent directional couplers and very precise work has to be done to set up the link. Furthermore, it is very time consuming and difficult to adjust in the tunnel with many taps (e.g., $\sim$ 70 tap points in total at the European XFEL)

- There is no control on the settings of the reference line after its operations have started. All setup and adjustment depend on the operation point. During machine operation, too many factors (such as aging, temperature, and humidity variations) could influence the component parameter, which could decrease the performance of the reference line.

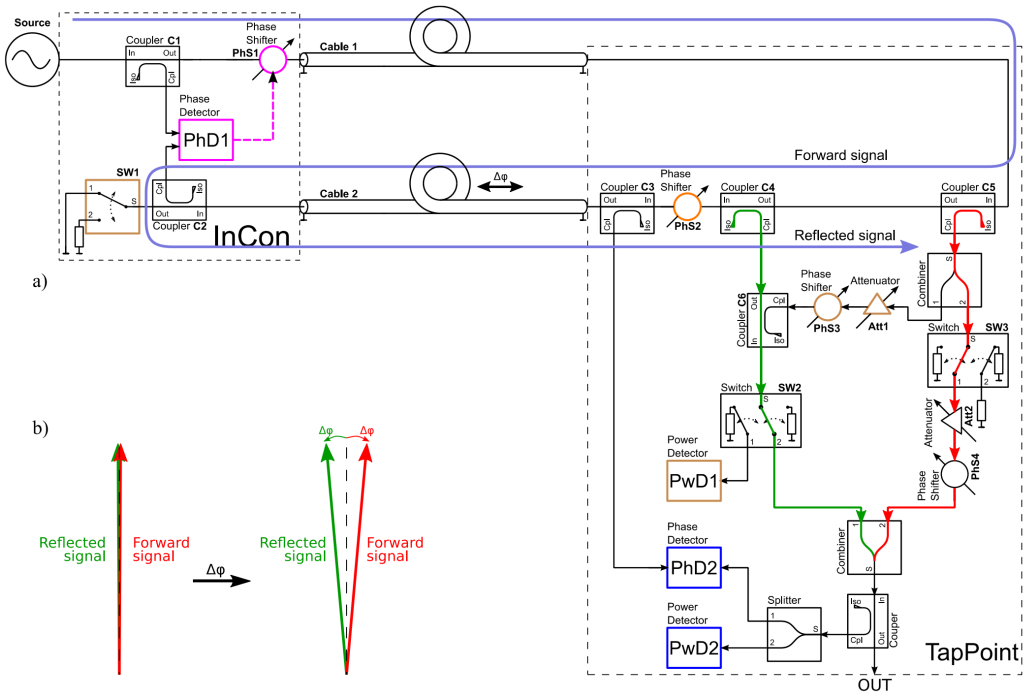

Figure 2.12: Concept design of the interferometric phase stabilization system over coaxial cable [37].

A prototype of the active phase stabilization system based on the interference phenomenon is proposed and developed to provide fully automatic adjustments of parameters and more reliable operation. It allows setting the interferometer link to an operating point with a maximum suppression factor (SF), which is defined as the ratio of unsuppressed to suppressed phase drift values, and adjusting it anytime. We evaluate the system performance from the SF. Figure 2.12 shows the concept design of the interferometric phase stabilization system over coaxial cable. The interferometric phase stabilization system is composed of a transmitter called an InCon (Interferometer Controller) and a receiver called a TapPoint. A phase reference signal from the source is distributed through the InCon, Cable 1, TapPoint, and Cable 2 (main coaxial cable) to the GND short at InCon. This is the forward signal,

which is reflected from the GND short and then goes back to the TapPoint, where fractions of the forward and reflected signals are coupled out from the main line by couplers C4 and C5. Both signals interfere an RF power combiner to cancel the phase drifts appearing in the main coaxial cable (Cable 2 between InCon and TapPoint). The adjustment procedure, hardware design, and algorithm are explained in detail in [37].

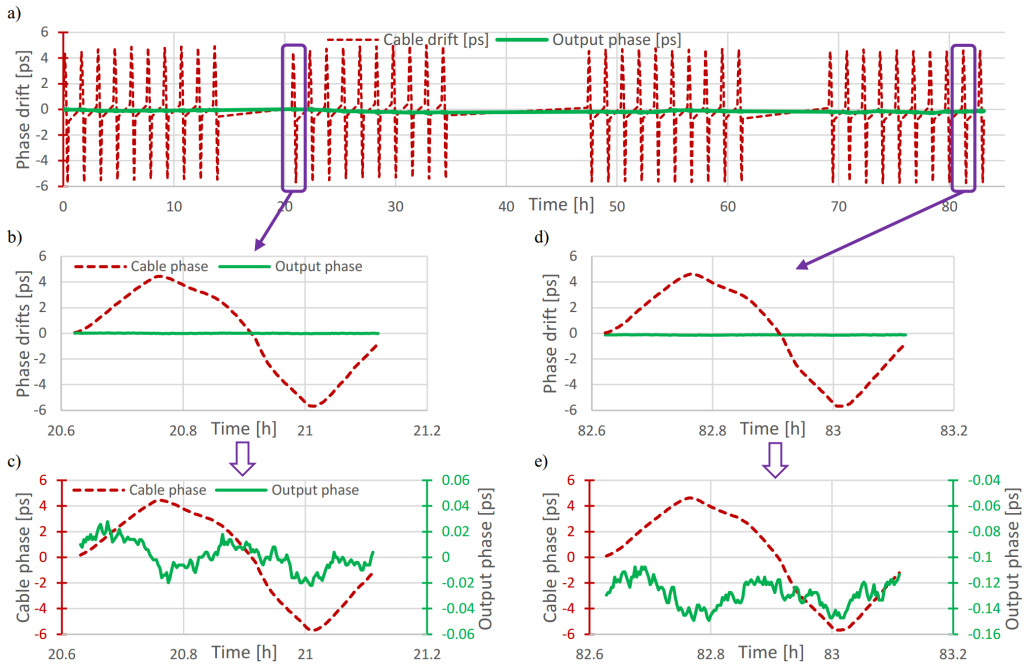

Figure 2.13: Interferometer test results: main coaxial cable phase drifts and interferometer output phase drifts vs. time [37].
a) Results over entire 85 h test.
b) Results picked from phase change cycle at 21th h.
c) Results picked from phase change cycle at 21th h with zoomed output phase drifts.
d) Results picked from phase change cycle at 83rd h.
e) Results picked from phase change cycle at 83rd h with zoomed output phase drifts.

The main cable was located inside the climate chamber to ensure that the RF phase of the cable drifts due to the temperature fluctuation. During the test, the phase drift in the main coaxial cable was roughly 10 ps from the operating point, which is comparable to the real phase drift of 12.3 ps in the accelerator tunnel for two days. The long-term (85 hours) measurement result is shown in Fig. 2.13. It is evident to see that the phase drift in the

main coaxial cable is significantly suppressed by monitoring the phase drift in the interferometer link output. It is less than 50 fs (pk-pk) corresponding to a suppression factor of 200.

In comparison to the demonstration at Fermilab, the improvements of the automatic interferometer are

- Precise and automatic cable length adjustment

  The appropriate cable length between the directional couplers (C4 and C5) of InCon and TapPoint can be adjusted by a phase shifter (PhS2) in the TapPoint.

- Equal amplitude and phase adjustment for the forward and backward signals

  Equal amplitudes and phase shifts against the signal source of the forward and reflected signals can be adjusted using a variable attenuator (Att2) and variable phase shifter (PhS4) at the TapPoint, respectively.

- Isolation improvement for coupler C4 and C5

  The isolation of the directional coupler significantly influences the system performance. High isolation ($>$ 30 dB) is required in C4 and C5 (typical isolation in the market is between 20 dB and 30 dB). Isolation can be improved by using two switches (SW1, SW2) and a circuit consisting of a phase shifter (PhS3), attenuator (Att1), and directional coupler (C6) used as a power combiner. The details can be found in [37].

- Phase relationship measurement without disconnection

  In the phase averaging reference line of Fermilab, the phase relationship between the forward and backward signals are adjusted manually and the link had to be disconnected at the right side input of the C5 coupler. This leads to the errors from this disconnecting and not suitable for practical machine operation. By adding a coupler (C3), which provides a fraction of the forward signal to the TapPoint, the coupled forward and reflected signal parameters can be adjusted.

An advanced phase stabilization system with interferometer is successfully developed and the prototype in the laboratory shows that the phase drift in the long coaxial cable can be automatically calibrated with a stability of sub-100 fs. It can be used into the European XFEL facility and can also be implemented as a good solution for other large facilities.

2.4 Comparison of RF Reference Distribution Systems

For remote reference distribution over several hundreds of meters and a few kilometers, most phase stabilization systems are based on optical fiber and many techniques are applied to achieve a stability of sub-10 fs to hundreds femtoseconds level. Table 2.2 shows a comparison of the design scheme and system performance for the RF reference distribution system over optical fiber at SuperKEKB ring, SACLA, and European XFEL. The phase stabilization system is applied in the operated machines instead of being demonstrated in the laboratory or the test stand. The RF reference distribution scheme varies from facility to facility. The advantages and disadvantages of the different schemes are also discussed in Table 2.2. According to the requirement, there is a trade-off between cost, complexity of implementation, commercialization of devices, and performance. For local reference distribution, the coaxial cable is widely used for different facilities. A popular solution is based on the "phase averaging" method. An interferometric phase stabilization system is proposed and demonstrated by DESY. A stability of less than 50 fs (pk-pk) is achieved and the suppression factor is up to 200.

Table 2.2: Comparison of RF RDS over optical fiber.

Facility	**SuperKEKB ring**	**SACLA**	**European XFEL**
Requirement	±1.5 ps (pk-pk)	50 fs (pk-pk)	10 fs (rms)
Operation Mode	CW	Pulse	Pulse
RF Frequency	508.9 MHz	5712 MHz	1300 MHz
Dist. Length	1000 m	700 m	3400 m
Trans. Medium	PSOF	PSOF	PM fiber
Temp. fluctuation	±5 °C	±0.2 °C	±0.5 °C
Technique	WDM	Interferometer	Interferometer
Actuators	VODL	PDFS	ODL+PDFS
Feedback Loop	1	2 (coarse+fine)	2 (slow+fast)
Performance	±546 fs (pk-pk)	50 fs (pk-pk)	3.3 fs (rms)
Advantages and Disadvantages	simple commercialized low cost lower stability	complicated commercialized high cost high stability	very complicated self-built very high cost very high stability

Chapter 3

RF Reference Phase Drift Measurement at Injector LINAC

3.1 Phase Noise

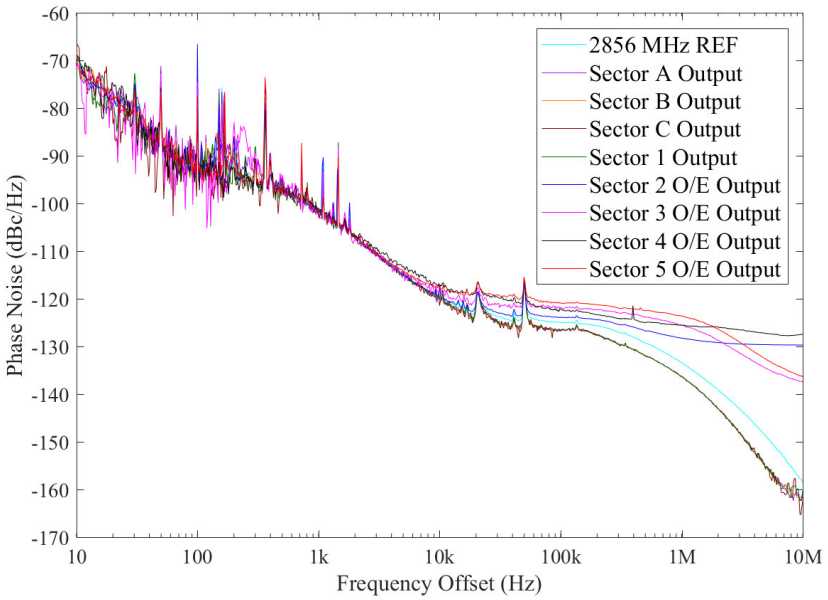

Figure 3.1: SSB phase-noise power spectrum of the transmitted signal at each sector (A-C and 1-5).

As shown in Fig. 1.3, the 2856 MHz reference signal (REF) is generated

by the reference generator based on LMO (571.2 MHz). For sector A-C and sector 1, the reference signal is distributed by the coaxial cable because they are close to MO. For sector 2 to sector 5, this electrical reference signal is converted to the optical signal by the E/O and distributed by PSOF. The transmitted optical signal is converted to the electrical signal by the O/E at each sector. The distance between two adjacent sectors is approximately 80 m. Thus, the length of the PSOF from MO to sector 2 to 5 is 140 m, 220 m, 300 m, and 380 m, respectively. The phase noise is measured using a signal source analyzer (E5052B, Agilent Technologies). Figure 3.1 shows the single side band (SSB) phase-noise power spectrum of the transmitted signal at each sector (A-C and 1-5). The result of integral bandwidth from 10 Hz to 10 MHz is shown in Table 3.1. All values of the timing jitter are less than 150 fs (rms).

Table 3.1: Integral timing jitter of the transmitted signal.

Signal	**Jitter [fs]**	**Phase Noise [deg.]**
2856 MHz REF	106.08	0.109
Sector A Output	103.03	0.106
Sector B Output	98.66	0.101
Sector C Output	90.99	0.094
Sector 1 Output	93.13	0.096
Sector 2 O/E Output	134.67	0.138
Sector 3 O/E Output	127.06	0.131
Sector 4 O/E Output	148.98	0.153
Sector 5 O/E Output	135.48	0.139

3.2 RF Phase Detection

3.2.1 Down Conversion

To measure the long-term phase drift in the reference signal, a phase detector with high accuracy and long-term stability is required. Several techniques of RF phase detection are applied in the accelerator field, which has been detailed in [38]. With the development of ADCs technology, although a bandwidth of a few GHz is available, a 2856 MHz RF is still too high for ADCs. Thus, the RF frequency is down-converted to the intermediate frequency (IF) using a local oscillator (LO). The IF signal is sampled by the oversampling technique to detect the RF phase.

Assuming that the RF signal $y_{RF}(t)$ and LO signal $y_{LO}(t)$ are two cosine

signals with amplitudes A_{RF},A_{LO} and frequencies f_{RF},f_{LO}. The IF signal $y_{IF}(t)$ can be represented as

$$\begin{aligned} y_{IF}(t) &= y_{RF}(t) \cdot y_{LO}(t) \\ &= A_{RF}\cos(2\pi f_{RF}t + \phi_{RF}) \cdot A_{LO}\cos(2\pi f_{LO}t + \phi_{LO}) \\ &= \frac{1}{2}A_{RF} \cdot A_{LO} \cdot (\cos[(2\pi f_{RF} + 2\pi f_{LO})t + (\phi_{RF} + \phi_{LO})] \\ &+ (\cos[(2\pi f_{RF} - 2\pi f_{LO})t + (\phi_{RF} - \phi_{LO})]) \end{aligned}$$

With down conversion, the input RF signal is transmitted to the upper $(f_{RF} + f_{LO})$ and lower $(f_{RF} - f_{LO})$ side band signals. The frequency of the IF signal is much lower than that of the RF and LO signals. The lower side band signal is extracted with a suitable LPF or BPF. The IF signal is given as

$$y_{IF}(t) = A_{IF}\cos(2\pi f_{IF}t + \phi_{IF}) \tag{3.1}$$
$$\tag{3.2}$$

where the frequency, amplitude, and phase of the IF signal are defined as

$$\begin{aligned} f_{IF} &= f_{RF} - f_{LO} \\ A_{IF} &= \frac{1}{2}A_{RF} \cdot A_{LO} \\ \phi_{IF} &= \phi_{RF} - \phi_{LO} \end{aligned}$$

The phase change in the RF signal is the same as that in the IF signal with a constant LO signal (constant A_{LO} and ϕ_{IF}). Furthermore, the phase noise or timing jitter at the RF signal are exactly translated to the IF signal.

3.2.2 Principle of IQ Detection

IQ Definition

The RF signal is down-converted to a lower IF signal, which can be digitized using an ADC. The continuous IF signal can be converted to a series of discrete sample points in time domain, which can be processed in the digital system. The IF signal is digitally processed in Cartesian coordinates (I/Q) instead of the polar coordinates (amplitude/phase).

Any cosine radio-frequency signal $y(t)$ can be represented using the amplitude/phase or I/Q components. This signal can be decomposed into its

sine and cosine components as follows [38]:

$$\begin{aligned} y(t) &= A\cos(\omega t + \phi_0) \\ &= \underbrace{A\cos\phi_0}_{I}\cos(\omega t) - \underbrace{A\sin\phi_0}_{Q}\sin(\omega t) \\ &= I \cdot \cos\omega t - Q \cdot \sin\omega t \end{aligned} \tag{3.3}$$

where A is the amplitude, ω is the RF angular frequency, and ϕ_0 is an initial phase of the RF signal. The amplitudes of the cosine and sine components are defined as I and Q components, respectively. The polar representation and its Cartesian representation can be transformed into each other. Consequently, the phase of the RF signal can be calculated by

$$I = A\cos\phi_0 \tag{3.4}$$

$$Q = A\sin\phi_0 \tag{3.5}$$

$$\phi_0 = \arctan(Q/I) \tag{3.6}$$

$$A = \sqrt{I^2 + Q^2} \tag{3.7}$$

Sampling Methods

The IF signal can be digitized using an ADC with a suitable sampling rate (SR). According to the Nyquist sampling theorem, a signal must be sampled at a rate greater than the Nyquist sampling rate (twice the maximum frequency component of the measured signal) to reconstruct the signal [39]. If the Nyquist criterion is not met, aliasing will occur. The RF signal information can not be extracted from the IF signal. However, based on the Nyquist-Shannon theorem, the sampling rate only needs to be twice the signal bandwidth, instead of the maximum frequency component. In this case, the signal can be measured using a sampling rate lower than the Nyquist sampling rate. There are three possibilities for sampling the IF signal using an ADC: IQ sampling, oversampling, and undersampling.

To calculate the phase of the RF signal, the sampling rate of the ADC must be synchronized with the measured RF frequency. The sampling rate f_s and the measured IF frequency f_{IF} must satisfy [38, 41]

$$f_s = \frac{f_{IF}}{K + \dfrac{N}{M}}, K = 0, 1, 2, 3... \tag{3.8}$$

where M is an integer greater than 3. N and K are integers. M and N are prime to each other.

When $K = 0$ and $M > 2N$, the sampling rate is higher than the Nyquist rate ($f_s > 2f_{IF}$), which is called the oversampling technique. Specially, with the condition $K = 0$ and $M = 4N$, the sampling rate is four times greater than the IF signal ($f_s = 4f_{IF}$) and the phase advance is fixed to 90°. This technique is called IQ sampling. Detailed explanations for each sampling method are given in [38].

In comparison to IQ sampling, the advantage of the oversampling technique is that (1) more sampled data are collected in one period; thus, the measurement error can be reduced by averaging over M samples as shown in Eq. 3.10 and 3.11. (2) The requirements of the ADC bandwidth and aperture jitter are not so stringent owing to the low frequency of the input signal, which implies low cost. However, the down-conversion stage is required in this method to ensure that the long-term stability of the phase detector is sensitive to the temperature and humidity fluctuations. This method is applied in the phase monitoring system of the RF reference signal at injector LINAC because the 2856 MHz RF is too high for most ADCs (see Section 3.4).

When $K > 0$, the sampling rate is lower than the Nyquist rate ($f_s < f_{IF}$), which is called the undersampling or direct sampling technique [40]. By using this technique, the signal is directly sampled by the ADC without the down-conversion stage. Thus, it makes the phase detector much simpler and the monitoring system is less affected by the slow temperature and humidity variations. The advantages also include lower requirement of the ADC sampling rate, lower data processing rates to digital signal processor (DSP) or the FPGA board, lower power consumption, and lower costs. However, the signal-to-noise ratio (SNR) of the ADC is very sensitive to the clock jitter in high-frequency applications and the RF frequency is limited by the sampling rate of ADC [42]. This method is applied to the phase monitor system between the LMO and RMO and its detailed explanation is given in Section 7.2.

IQ Detection

Figure 3.2 shows the block diagram of IQ detection where an RF signal is first down-converted to the IF signal and then digitized by an ADC with a suitable sampling rate. The sampling rate and the IF satisfy Eq. (3.8) and the phase advance $\Delta\varphi$ between the two adjacent samples can be represented by

$$\Delta\varphi = (K + \frac{N}{M}) \cdot 2\pi = \frac{f_{IF}}{f_s} \cdot 2\pi \tag{3.9}$$

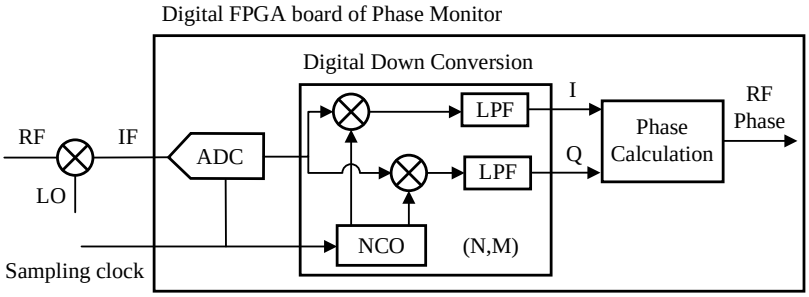

Figure 3.2: Block diagram of phase detection with analog down-conversion and digital IQ detection.

The I and Q baseband components of the measured IF signal can be calculated by the following equations [41].

$$I = \frac{2}{M} \sum_{n=0}^{M-1} x[n] \cos\left(\frac{2\pi \cdot N}{M} \cdot n\right) \tag{3.10}$$

$$Q = -\frac{2}{M} \sum_{n=0}^{M-1} x[n] \sin\left(\frac{2\pi \cdot N}{M} \cdot n\right) \tag{3.11}$$

where $x[n]$ is the n^{th} ADC sampled data.

The IQ values are evaluated in the digital down conversion (DDC). The procedure of this algorithm is explained as follows. First, the IF signal is digitized by the ADC, which is then down-converted to the base band by a digital mixer. The local oscillators are supplied by numerically controlled oscillators (NCOs), which generate a stream of sine and cosine samples according to the relationship between the input IF and the sampling rate. The digital mixer is realized as an ideal multiplier; thus, the digitized IF signal samples are multiplied by the NCOs. The outputs of the digital mixer are summed and the IQ value is evaluated using Eq.(3.10) and Eq.(3.11). The LPF shown as the final block in DDC is an anti-aliasing filter that aims to suppress the sum of the frequency components. Finally, the phase of the IF signal is calculated by using Eq.(3.6).

The sampled data of the IF signal is shown in Fig. 3.3 when $f_{IF} = 14.28\,\mathrm{MHz}, f_s = 114.24\,\mathrm{MHz}, M = 8 and N = 1$.

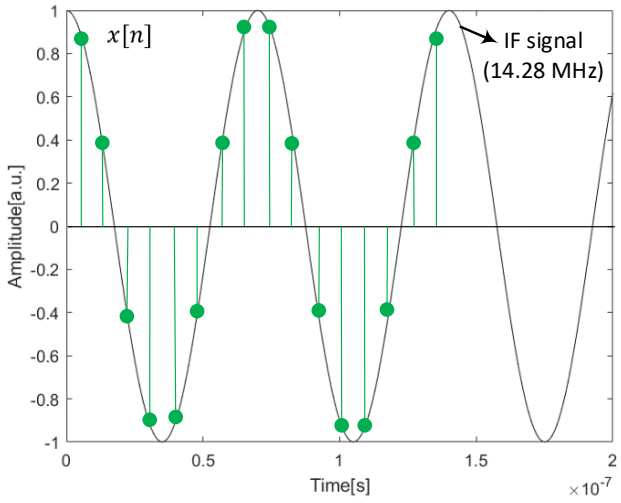

Figure 3.3: 14.28 MHz IF signal sampled using the oversampling technique. $x[n]$ is the sampled data. Data from eight samples data are collected in one IF period.

3.3 LO and Clock Generation

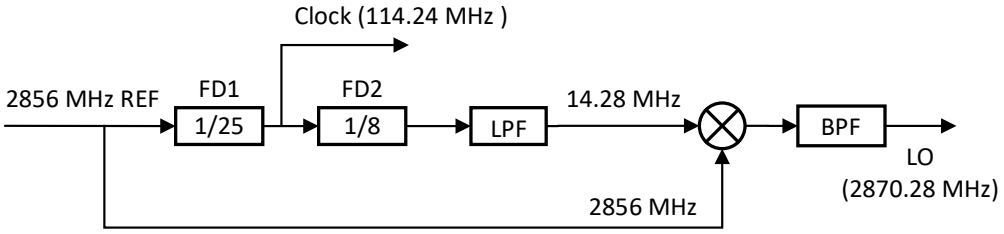

Figure 3.4: LO and clock generation.

Considering the ADC sampling rate limitation (130 MSPS, see Section 3.4) and the availability of IQ algorithm implementation ($M = 8, N = 1$) in the digital board, the sampling rate (f_s) is eight times greater than that of the IF signal (f_{IF}). The block diagram of the LO and clock (SR for ADC) is represented in Fig. 3.4. First, the 2856 MHz REF signal (f_{RF}) is divided by 25 to obtain the sampling rate (f_s). Then, the f_s is divided by eight and filtered by LPF to obtain the IF signal (f_{IF}). It is mixed with f_{RF} to obtain another frequency $f_{RF} \pm f_{IF}$. Finally, this output frequency is filtered by a BPF to obtain the LO frequency (f_{LO}) $f_{RF} + f_{IF}$ or $f_{RF} - f_{IF}$. In our case,

relationships between the RF, LO, IF, and SR are represented as

$$
\begin{aligned}
f_{RF} &= 2856\,\text{MHz} \\
f_s &= f_{RF}/25 = 114.24\,\text{MHz} \\
f_{IF} &= f_s/8 = 14.28\,\text{MHz} \\
f_{LO} &= f_{RF} + f_{IF} = 2870.28\,\text{MHz}
\end{aligned}
$$

Two same frequency dividers (FD, AD9516, Analog Devices) are used for the LO generation. The bandwidth of LPF is 15 MHz. The center frequency of BPF is 2870.28 MHz and its bandwidth is ± 5 MHz. The integral timing jitter is measured using a signal source analyzer (E5052B, Agilent Technologies). Figure 3.5 shows the SSB phase-noise power spectrum of the RF and LO signals. The result of the integral bandwidth from 10 Hz to 1 MHz is shown in Table 3.2. The induced jitter is from 10 Hz to 100 Hz.

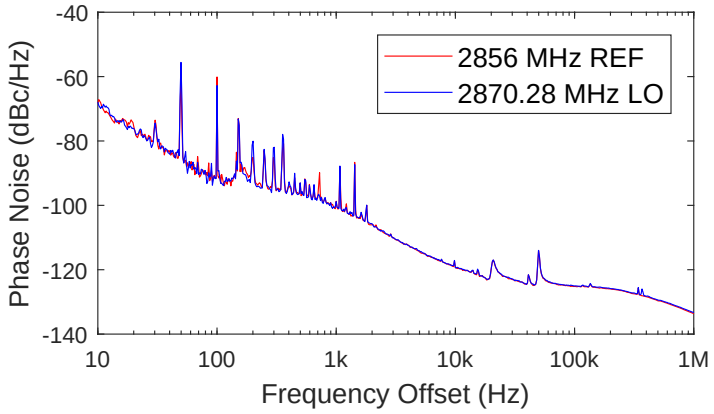

Figure 3.5: SSB phase-noise power spectrum of RF and LO signals.

Table 3.2: Integral timing jitter of RF and LO signals.

Signal	**Frequency [MHz]**	**Jitter [fs]**	**Phase Noise [deg.]**
REF	2856	168.17	0.173
LO	2870.28	191.44	0.198

3.4 Phase Monitor System Implementation

The current status of the RF reference distribution system is described in Chapter 1. To monitor the RF reference phase drift in each sector, two

problems arise. (1) The transmitted signal is physically several hundred meters away from the REF signal at the MO side, which makes it difficult to measure the phase drift between them. (2) It is impossible to touch the RF reference line during the operation of SuperKEKB LINAC. An example of signal distribution between REF and Sector 5 is shown in Fig. 3.6. The transmitted signal had to be sent back with another pair of O/E and E/O modules and the same length and same type of PSOF. A 2856 MHz returned signal is obtained at the MO side. The returned signal is down-converted to the IF signal and then the IQ components are calculated using Eqs.(3.10) and (3.11). The phase drift of returned signal is expected to be twice of the transmitted signal.

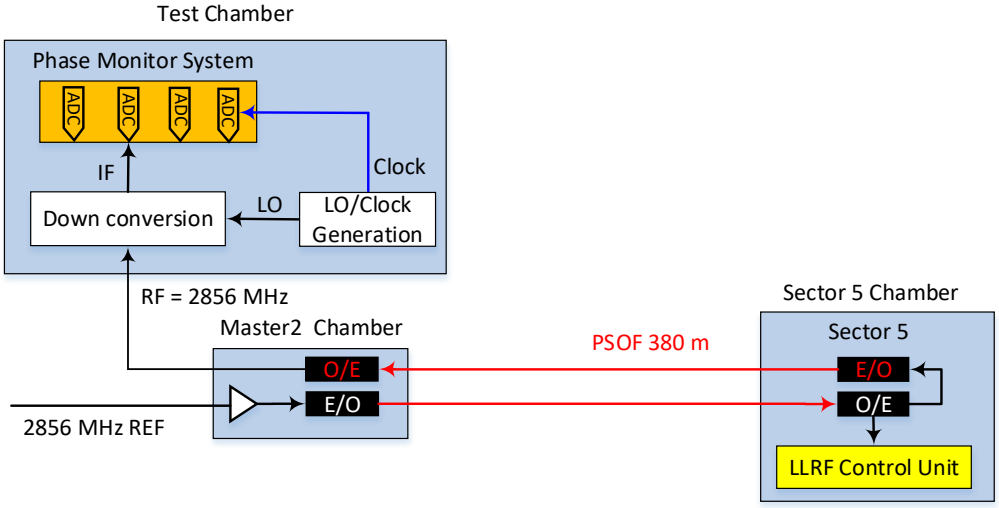

Figure 3.6: Phase drift monitoring between REF to Sector 5.

A phase monitor was implemented in the digital board based on the Micro Telecommunications Computing Architecture (μ TCA) standard. The μTCA chassis is shown in Fig. 3.8. An advanced mezzanine card (AMC) was used as shown in Fig. 3.7. This board is equipped with Xilinx Virtex-5 FXT FPGA, four 16-bit ADCs (130 MSPS high-speed, 700 MHz input bandwidth, LTC2208), four 16-bit digital-to-analog converters (DAC, 500 MSPS high-speed, AD9783), and digital input/output (DIO) channels.

To monitor the phase drift in each sector, the short optical link (E/O+1m PSOF+O/E), system phase drift, and two digital boards are necessary owing to not enough ADC channels. The full diagram of the phase monitor system is shown in Fig. 3.9. The 2856 MHz REF is split into two as the reference signal for both digital boards. All 2856 MHz signals are down-converted to

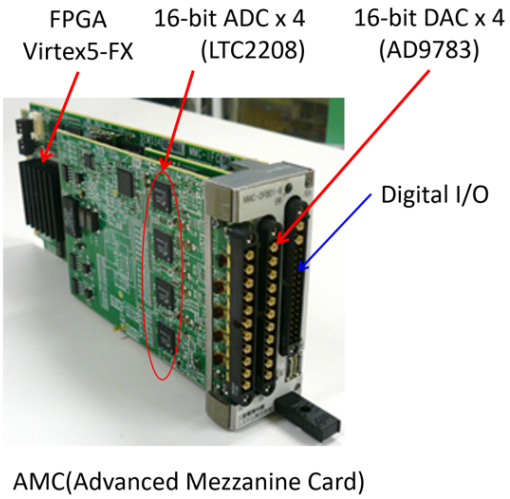

Figure 3.7: Digital board used to implement the oversampling technique.

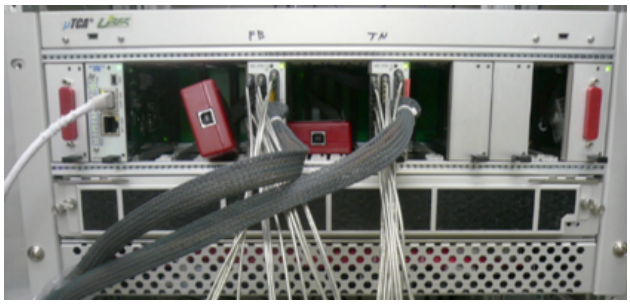

Figure 3.8: μTCA chassis.

IF signals. The returned signals from sector 2 and 3 are measured by board1 and the returned signals from sector 4 and 5 are measured by board2. The phase drift of the short optical link is monitored by board1. The injector LINAC is operated in the pulse mode and the reference phase of the injector is changed depending on the injection mode of HER/LER at 50 Hz. The short-term and long-term data recordings should be synchronized with a 50 Hz beam trigger, and should exclude the phase changing timing. Thus, 1 ms short-term averaged raw data are used to measure the long-term phase drift. To improve the accuracy of phase detection, a digital LPF with a bandwidth of 100 kHz is applied [43].

The short-term phase stability with digital LPF (100 kHz bandwidth) is presented in Fig. 3.10 and the results are summarized in Table 3.3. All short-term phase stabilities are less than 0.1° (rms), which fulfills the requirement

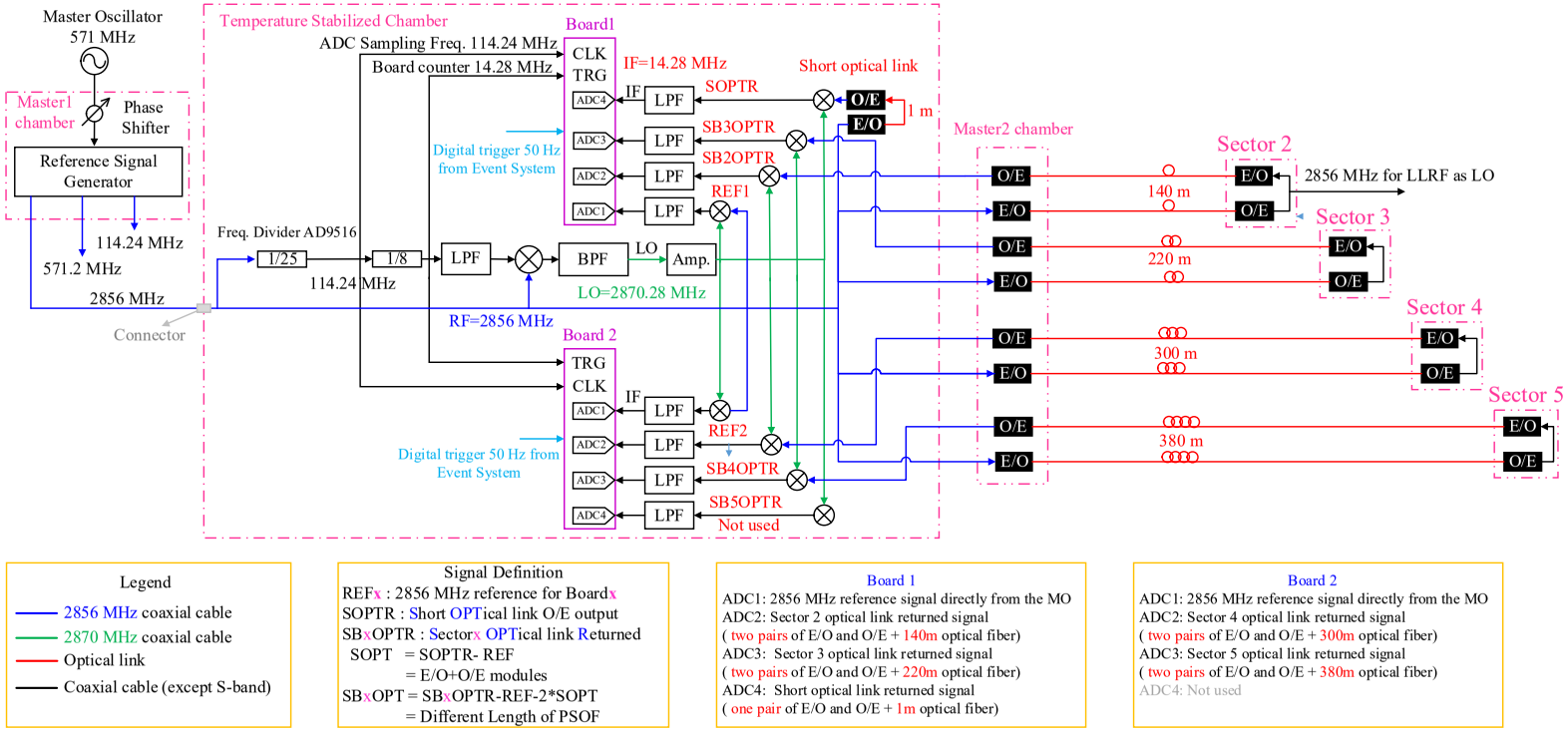

Figure 3.9: Full diagram of the phase drift monitor at Sector 2 to 5.

of 0.2° (rms).

Table 3.3: Short-term phase stabilities of REF, short optical link (SOPTR), and returned (SBxOPTR) signal at Sector 2 to 5.

Signal	**Stability [deg.(rms)]**
REF	0.027
SOPTR	0.024
SB2OPTR	0.065
SB3OPTR	0.068
SB4OPTR	0.064
SB5OPTR	0.076

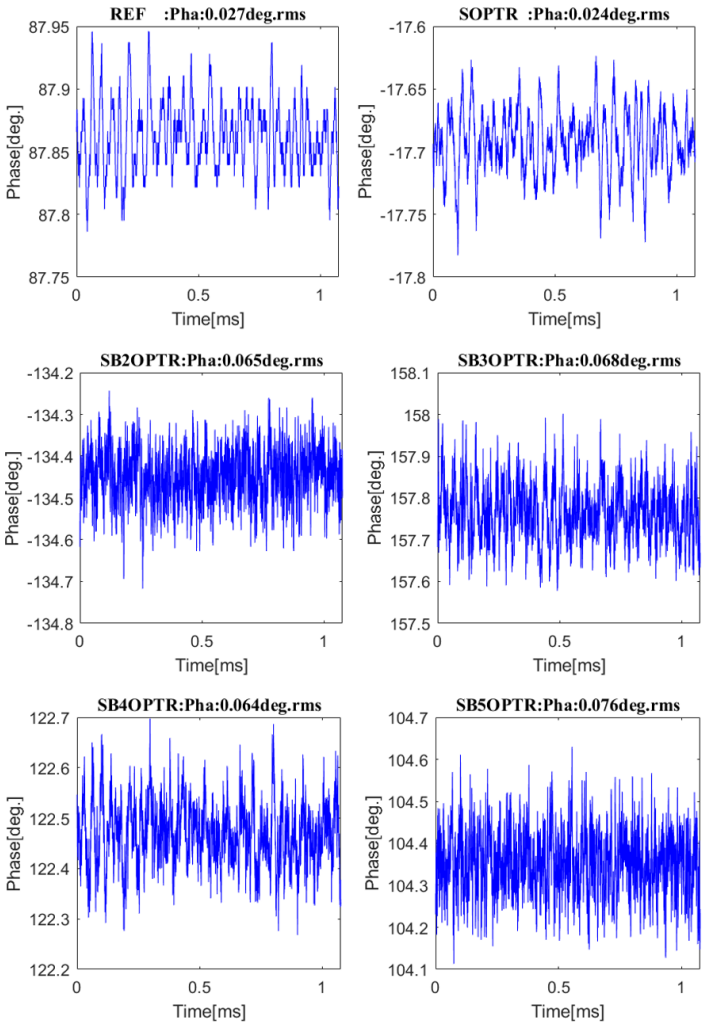

Figure 3.10: Short-term phase stabilities of of REF, short optical link, and returned signal at Sector 2 to 5.

3.5 Long-term Phase Drift Measurement

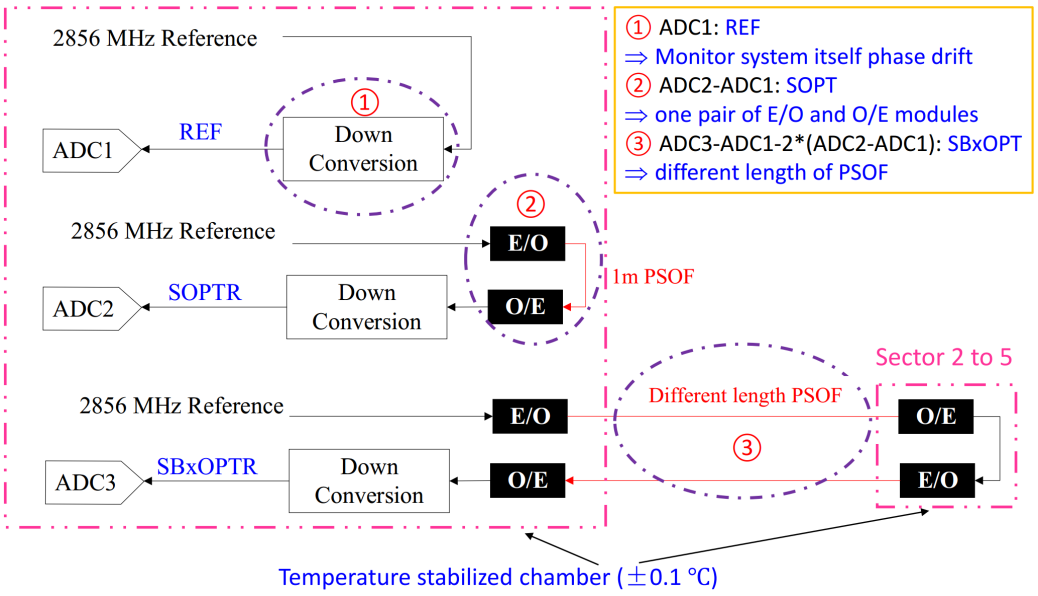

Figure 3.11: Explanation for the contributions of phase drift.

The long optical links from REF to each sector consist of one pair of E/O and O/E modules and different lengths of PSOF. To analyze the contributions of phase drift, the following setup is illustrated, as shown in Fig. 3.11. As mentioned above, the RF signal is first down-converted by the ADC, composed of frequency dividers, mixers, BPF, amplifiers, and coaxial cables of different lengths. These RF components and cables have a phase drift so that the 2856 MHz REF signal is measured by ADC1 to indicate the monitor system phase drift (REF: ADC1, $\Delta\phi_1$). To estimate the phase drift of the E/O and O/E modules, the short optical link, which consists of 1 m PSOF and one pair of E/O and O/E modules, is measured by ADC2 ($\Delta\phi_2$). Thus, the phase difference between ADC2 and ADC1 indicates the phase drift of one pair of the E/O and O/E modules (SOPT = ADC2 - ADC1), omitting the effect of 1 m PSOF. The long optical link, which is composed of different lengths of PSOF and two pairs of E/O and O/E modules, is monitored by ADC3 ($\Delta\phi_3$). Therefore, the PSOF phase drift can be estimated by

$$\Delta\phi_{REF} = \Delta\phi_1 \tag{3.12}$$
$$\Delta\phi_{SOPT} = \Delta\phi_2 - \Delta\phi_1 \tag{3.13}$$
$$\Delta\phi_{SBxOPT} = \Delta\phi_3 - \Delta\phi_1 - 2 \cdot \Delta\phi_{SOPT} \tag{3.14}$$
$$\Delta\phi_{SBxTRN} = \frac{1}{2}(\Delta\phi_3 - \Delta\phi_1) \tag{3.15}$$

In our monitor system, the correspondence is

$$\Delta\phi_1 = \Delta\phi_{REF}$$
$$\Delta\phi_2 = \Delta\phi_{SOPTR}$$
$$\Delta\phi_3 = \Delta\phi_{SBxOPTR}$$

3.5.1 Transmitted Phase Drift at Each Sector

The long-term phase drift of the 2856 MHz REF, short optical link, and returned signals from sector 2 to 5 are measured by the phase monitor system during LINAC RF operation. Seven-day phase drifts are directly observed by ADCs, as shown in Fig. 3.12 and the results are summarized in Table 3.4. The phase drift of the transmitted signal (TRS) is estimated in Table 3.5. In this section, all phase drifts are discussed in pk-pk. The phase drift of the transmitted signal at each sector is more than 5°, which cannot fulfill the requirement.

Table 3.4: Long-term phase drifts of REF, E/O+O/E, and returned signal at sector 2 to 5.

Signal	**Phase Drift**
REF1	4.45
REF2	3.97
SOPTR	3.08
SB2OPTR	-7.96
SB3OPTR	-6.32
SB4OPTR	-9.35
SB5OPTR	-9.18

Table 3.5: Long-term phase drifts of the transmitted signal at sector 2 to 5.

Signal	**SB2TRS**	**SB3TRS**	**SB4TRS**	**SB5TRS**
Phase Drift	-5.76	-5.22	-6.22	-6.16

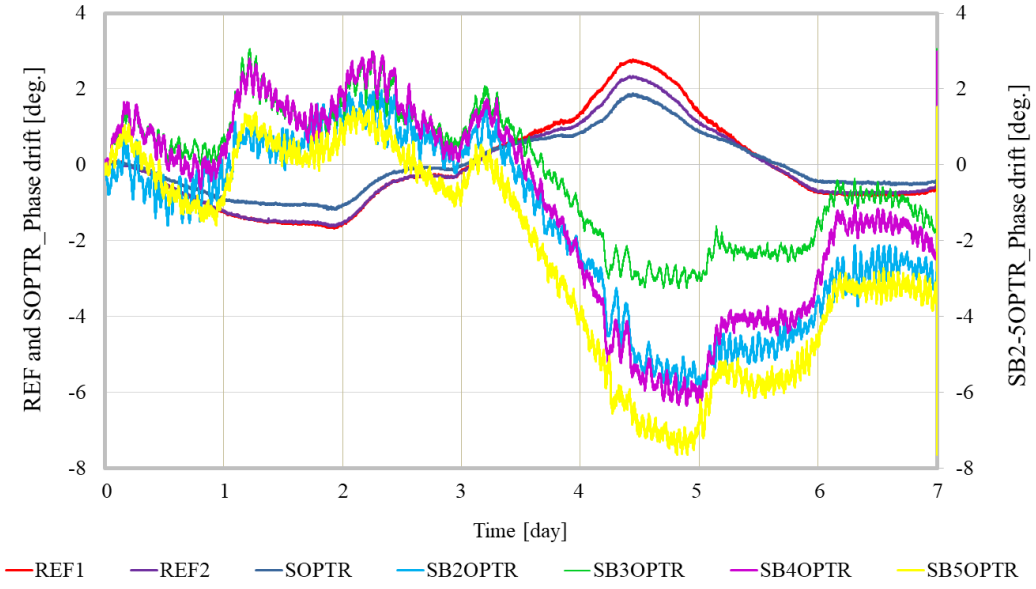

Figure 3.12: Long-term phase drift for each channel including system drift.

The phase drift of the reference signal is 4.45° and 3.97°, observed by digital board1 and board2, respectively. The system phase drift is very large and different; therefore, the sources and the solution are discussed in Chaper 5.

3.5.2 Contribution of Phase Drift

The contributions of the transmitted reference phase drift consist of long PSOF and E/O and O/E modules. Their phase drifts are shown in Fig. 3.13 and summarized in Table 3.13. The phase drift of the E/O and O/E modules is −1.47°, which is in the opposite direction of the system phase drift. The phase drift of PSOF varies from −7° to −10° in the same direction of the E/O and O/E modules. This drift is not proportional to the length of PSOF because of the following two reasons.

(1) Monitoring system phase drift

As shown in Fig. 3.12, the system phase drift is as large as 4.5° and it is different for each board. The phase drift of the PSOF is a calculated value, which is affected by the measurement error.

(2) Different phase drifts of the E/O and O/E modules at each sector

In our estimation, we assumed that the phase drift of the E/O and O/E modules at each sector is the same as that of the short optical link. However, phase drift can be different in each sector owing to the different humidity fluc-

tuations in the environment, despite temperature stabilized. (see Chapter 4).

(3) Effects of different temperature and humidity fluctuations on PSOF in the gallery

The phase drift of PSOF is mainly caused by the temperature and humidity fluctuations in the gallery. The phase drift is proportional to temperature and inversely proportional to humidity. In reality, the temperature and humidity fluctuations at each sector are very different. Thus, it is difficult to precisely estimate the phase drift.

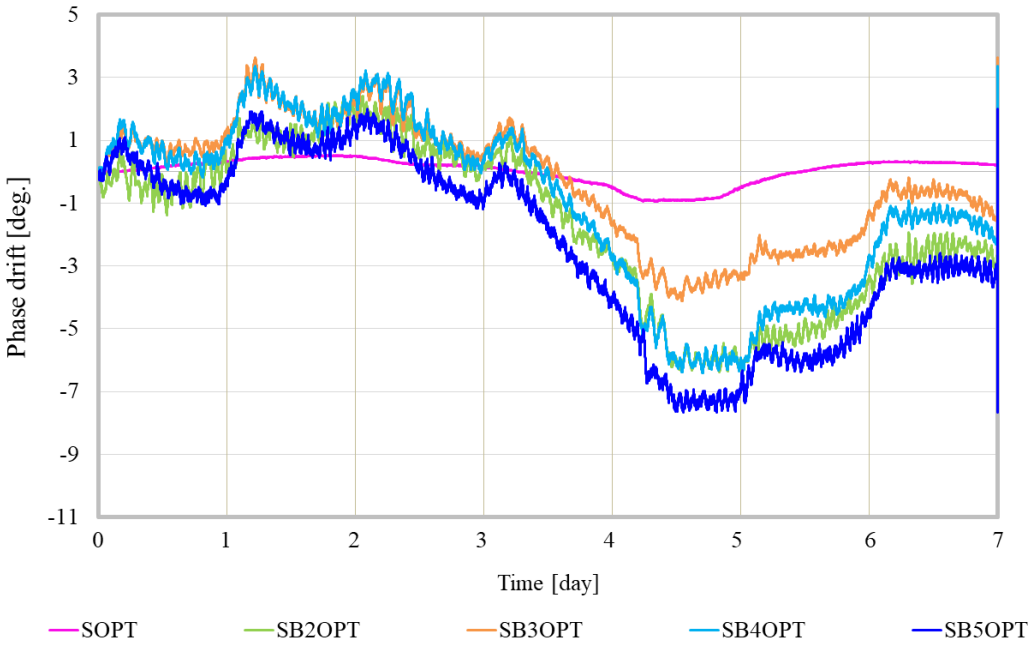

Figure 3.13: Phase drifts of the E/O and O/E modules, different lengths of PSOF.

Table 3.6: Long-term phase drift of the E/O + O/E + different lengths of PSOF at sector 2 to 5.

Signal	Phase Drift	PSOF Length
SOPT	-1.47	1 m
SB2OPT	-8.78	280 m
SB3OPT	-7.75	440 m
SB4OPT	-9.77	600 m
SB5OPT	-9.67	760 m

Chapter 4

Causes of Phase Drift in Optical Link

The reference phase drift in the optical link depends on the characteristics of the E/O and O/E modules and the optical fiber.

4.1 Optical Components

4.1.1 E/O and O/E Modules

The E/O (EOC-144) and O/E (OEC-1041) modules are customized by TAMAGAWA Electronics Inc. [44] owing to their lower phase noise [45]. The specification are listed in Table 4.1. The electronics and optical components inside the modules are affected by the temperature and humidity fluctuations.

Table 4.1: Specification of EOC-144 and OEC-1041 modules.

Item	**EOC-144**	**OEC-1041**
Optical power	+7.8 dBm	+7.0 dBm
RF input/output range	10 3000 MHz	
RF input/output level	-20 dBm (max. 0 dBm)	
Typical Wavelength	1310 nm/1550 nm	
Temperature range	-10 °C to +40 °C	

4.1.2 Phase-stabilized Optical Fiber

Light undergoes the group delay when passing through an optical fiber. The group delay can be represented as [46]

$$\tau = \frac{L}{c}(n - \lambda\frac{dn}{d\lambda}) \tag{4.1}$$

where τ is the group delay, L is the length of optical fiber, c is the light speed in vacuum, n is the refractive index at core center, and λ is the wavelength.

In the jacketed optical fiber, the temperature, humidity, and the longitudinally-applied mechanical tension acting on the fiber (such as the jacket tension) bring changes in both fiber length and refractive index, each of which affects the group delay [46, 47, 48, 49, 50]. The phase drift (at degree) caused by the group delay at a certain frequency (f_{crf}) can be represented as

$$\phi = 2\pi f_{crf} \cdot \tau \cdot 360^{\circ} \tag{4.2}$$

From Eq. (4.1), the group delay is also depending on wavelength, thereby resulting in the chromatic dispersion in the single-mode optical fiber. Wavelength dispersion will be explained in Section 4.1.2. A special optical fiber called phase-stabilized optical fiber was widely used for RF reference distribution in SuperKEKB injector LINAC and rings. In comparison to the standard silica optical fiber with positive thermal expansion coefficient, the silica glass of the PSOF is coated with a liquid crystal ploymer (LCP) with negative thermal expansion coefficient [51]. Thus, the thermal coefficient of the PSOF is reduced to be less than 5 ps/km/°C. Accordingly, the humidity coefficient of the PSOF is also changed owing to the LCP coating. Nowadays, only Furukawa Electric Co., Ltd. [53] can provide the PSOF.

Wavelength Dispersion

According to Eq.(4.1), group delay not only depends on the length of optical fiber, refractive index, but also wavelength. The propagation velocity through a dielectric medium depends on the optical angular frequency or wavelength [54]. The most often used parameter for measuring the chromatic dispersion is the dispersion coefficient D, which is defined as

$$D = \frac{d\tau_g}{d\lambda}[\frac{ps}{nm \cdot km}] \tag{4.3}$$

where $d\tau_g$ is the group delay per unit length and λ is the optical wavelength.

In optical fiber, the chromatic dispersion consists of material dispersion and waveguide dispersion. Material dispersion depends on the refractive index of the core and cladding on the optical wavelength. Waveguide dispersion

depends on fiber-design parameters such as core radius and core-cladding index difference. This waveguide dispersion is also defined as the dependence of the effective refractive index on light wavelength. Thus, the chromatic dispersion coefficient, including the contributions of material dispersion and waveguide dispersion, are typically modeled using the Sellmeier formula [55]

$$D(\lambda) = \frac{S_0}{4}(\lambda - \frac{{\lambda_0}^4}{\lambda^3}) \tag{4.4}$$

where S_0 is the chromatic dispersion slope at the zero dispersion wavelength λ_0. Thus, the chromatic dispersion coefficient is dependent on the wavelength.

4.2 Temperature and Humidity Dependency at Injector LINAC

In Section 3.5, several degrees of phase drifts were observed in the optical link at the LINAC gallery owing to the temperature and humidity fluctuations in the LINAC gallery, where the temperature is stabilized within ±1 °C by air conditioners but there is no humidity control. The 2856 MHz REF is close to sector 1; therefore, the PSOFs are distributed from sector 1 to sector 2-5 in the gallery. The RF phase of PSOF is affected by the gallery temperature and humidity. To reduce the temperature effect on the phase monitor system, the RF components, E/O and O/E modules, and digital boards are situated inside the temperature stabilized chamber (TC) with more precise control of ±0.1 °C. Therefore, the E/O and O/E modules are mainly influenced by the humidity due to the small temperature fluctuation. All temperatures and humidities are measured at the same time with the phase drift in the transmitted reference signal. All fluctuations are discussed in pk-pk.

4.2.1 Humidity Dependency

The humidity sensors are only installed inside the chamber at each sector instead the gallery. However, the humidity change trend inside the chamber can indicate that in the gallery. There is only a slight difference between them. Figure 4.1 represents the phase drift in each part and the changes in humidity around them. It was found out that phase drift depends on humidity and is negatively correlated to it. Humidity varies from 13 to 37%RH (relative humidity) over seven days. The changes in humidity at each sector is summarized in Table 4.2. The maximum (max.) humidity

change is 24%RH. Furthermore, the humidity effect on the components or PSOF is as slow as several hours, implying that phase drift lags behind the changes in humidity by several hours. Furthermore, the phase drifts of the E/O and O/E modules are very smooth but there are some glitches in the PSOF phase drift due to the temperature of the gallery.

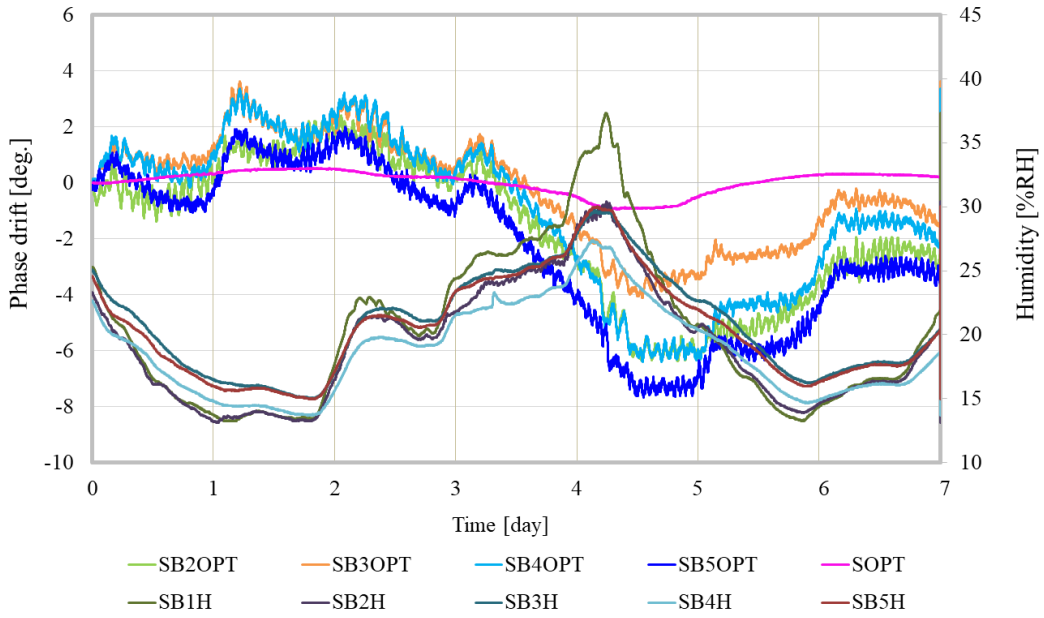

Figure 4.1: Humidity inside the chamber at each sector for seven days. SBnH: humidity inside the chamber at sector n.

Table 4.2: Humidity change at each sector.

Sector	**SB2H**	**SB3H**	**SB4H**	**SB5H**
Humidity [%RH]	24.1	17.4	14.7	13.7

4.2.2 Temperature Dependency

The temperature sensors are installed in the gallery and inside the chamber at each sector. The temperature fluctuations inside the chamber at sector 1 to 5 are $\pm 0.1\,^{\circ}\mathrm{C}$. Figure 4.2 shows the gallery temperature fluctuations from sector 1 to 5. Although the gallery temperature is controlled within $\pm 1\,^{\circ}\mathrm{C}$, the fluctuation varies in each sector. The PSOF is distributed from sector 1 to sector 2-5 to ensure that it is affected by the gallery temperature in different sectors. The PSOF distributed to sector 2 is affected by the

gallery temperature in sector 1 and 2. However, the PSOF distributed to sector 5 is affected by the gallery temperature in sector 1,2,3,4,and 5. The effect is accumulated by all the temperature fluctuations where the PSOF goes through. It is difficult to determine the temperature dependency from Fig. 4.2 because the humidity effect is included. Thus, we focus on the glitches and discuss the temperature effect individually in each sector.

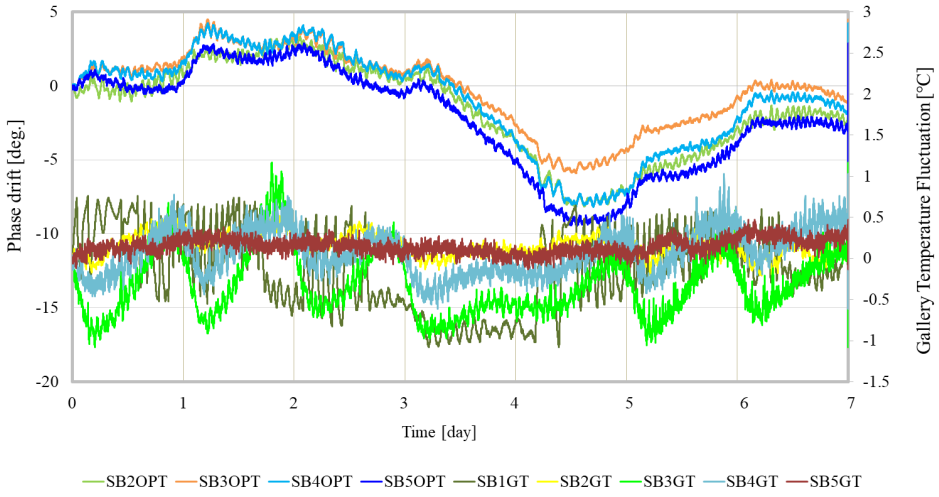

Figure 4.2: Phase drift in PSOF vs. temperature fluctuation at LINAC gallery. SBnGT: temperature in LINAC gallery in sector n.

Figure 4.3, 4.4, 4.5 and 4.6 show the phase drift in PSOF and sum of the gallery temperature fluctuations in sector 1-2, 1-3, 1-4, and 1-5, respectively. The data are taken from the first two of the seven days in Fig. 4.2. It was found that the phase drift is negatively correlated to the sum of gallery temperatures.

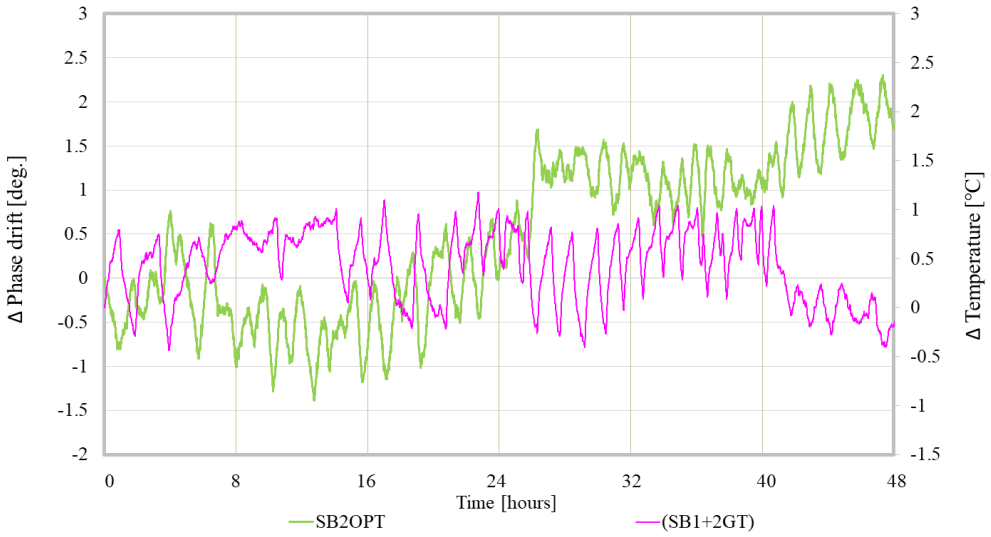

Figure 4.3: Phase drift in PSOF vs. sum of gallery temperature fluctuations in sector 1 to 2.

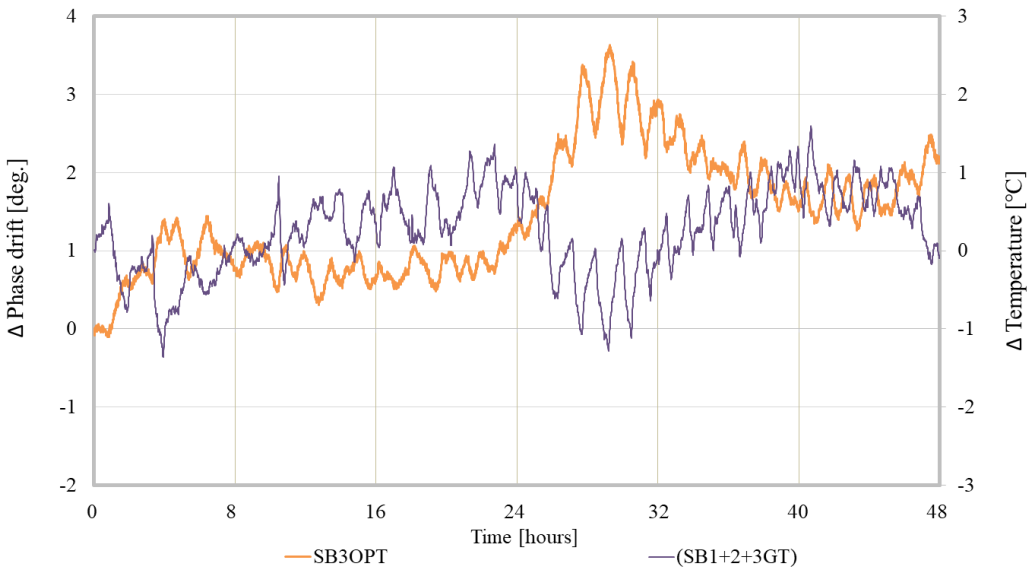

Figure 4.4: Phase drift in PSOF vs. sum of gallery temperature fluctuations in sector 1 to 3.

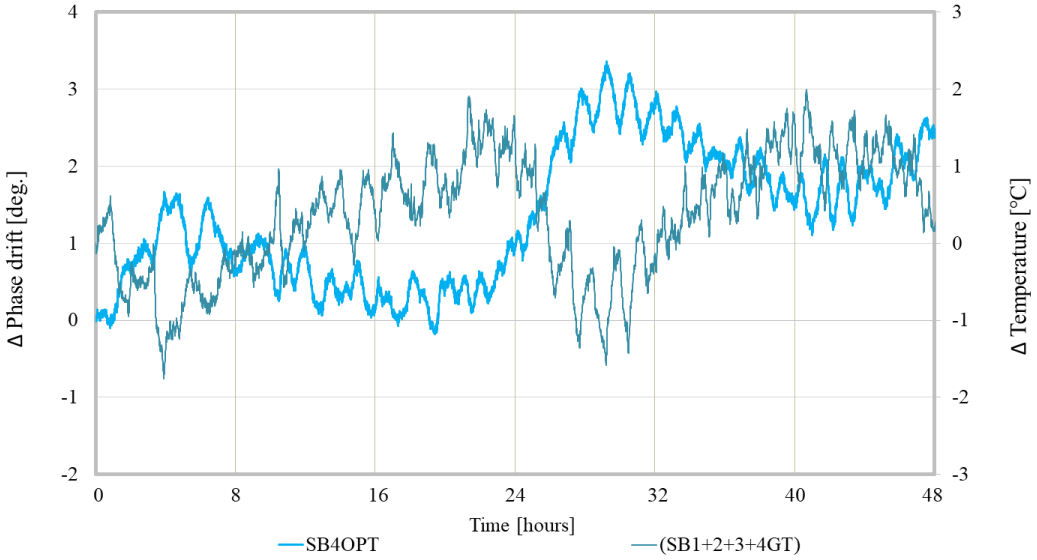

Figure 4.5: Phase drift in PSOF vs. sum of gallery temperature fluctuations in sector 1 to 4.

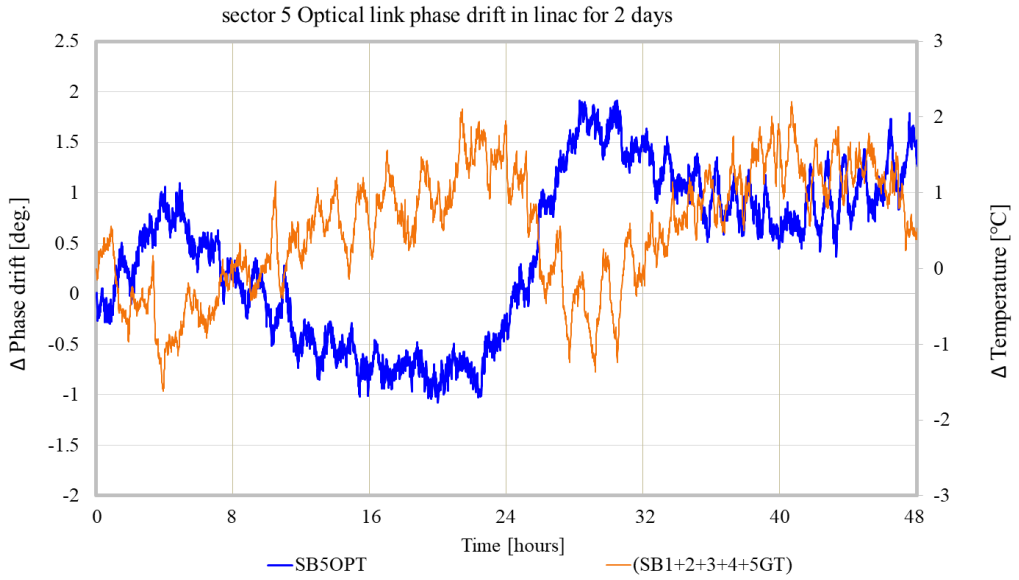

Figure 4.6: Phase drift in PSOF vs. sum of gallery temperature fluctuations in sector 1 to 5.

4.3 Temperature and Humidity Characteristics

The phase drifts in the PSOF and E/O, O/E modules are caused by the temperature and humidity fluctuations in the environment.

4.3.1 Measurement Setup for PSOF

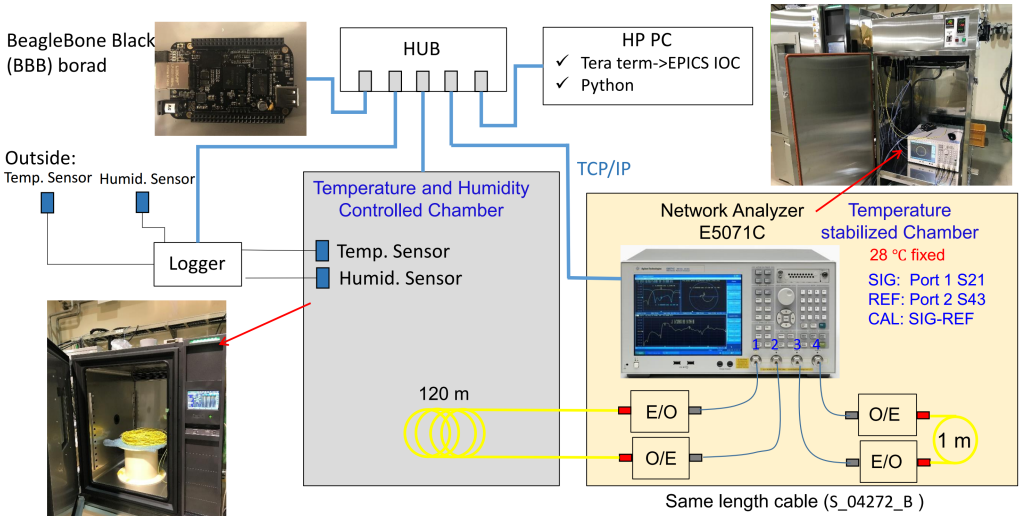

Figure 4.7: Configuration of the test system for PSOF.

According to Eq.(4.1), an exact calculation is impossible because the material parameters are not fully provided by the cable manufacturers and their values in the literature are widely different. To estimate the transmission time delay of PSOF, the temperature and humidity coefficients are measured using a 4-port network analyzer (NA, E5071C, Agilent Technologies). The setup of the test system for PSOF is shown in Fig. 4.7. The 2856 MHz RF signal from port 1 of NA is converted to optical signal by E/O. The optical signal is transmitted by 120 m PSOF, which is placed in the temperature and humidity controlled chamber (THC). The optical signal is converted to electrical signal by O/E and received by port 2. Thus, the phase change in the S21 parameter is measured when the temperature and humidity are changed near the PSOF inside the THC. To reject the system phase drift, a coaxial cable of the same length and the same pair of E/O, O/E modules (1 m) are used as reference. Additionally, the E/O and O/E modules, coaxial cables, and NA are situated inside the temperature stabilized chamber with temperature 28±0.1 °C. The

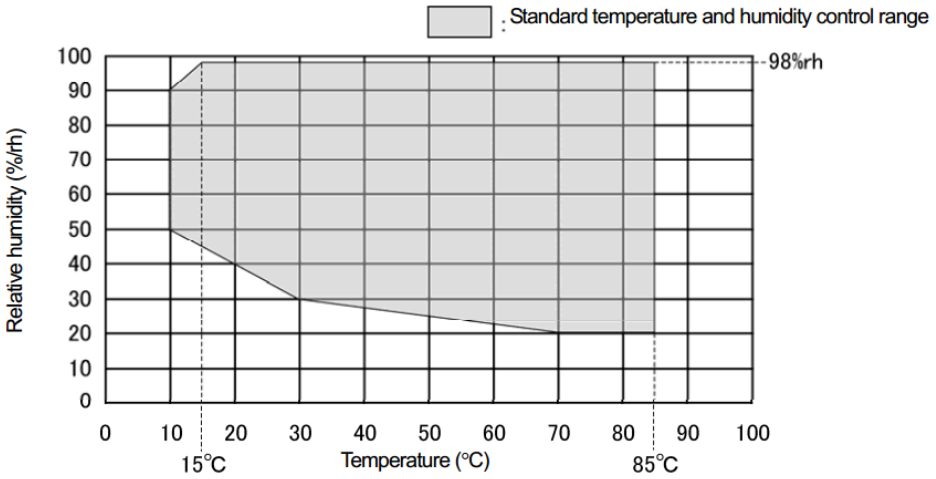

Figure 4.8: Temperature and humidity control range for THC.

120 m PSOF is not convoluted on the spool but free to stretch in space such that phase change is only caused by the temperature and humidity fluctuations without other external forces.

In LINAC gallery, the temperature is controlled at 28±1 °C and the relative humidity varies from 10%RH to 50%RH. To avoid the influence of temperature and humidity, the test temperature and humidity range are carefully chosen for the device under test (DUT). The temperature and humidity control range of THC are illustrated in Fig. 4.8. The standard control range is in the grey area. When the temperature is fixed to 28 °C as the temperature in LINAC gallery, the relative humidity only can be controlled only above 30%RH. Relative humidityIt cannot be set from 10%RH to 30%RH. Considering the temperature and humidity in LINAC gallery, the control range of THC, and the operation range of PSOF, the temperature is changed from 20 to 35 °C with fixed humidity at 50%RH to measure the temperature coefficient and the relative humidity is changed from 30 to 30%RH with fixed temperature at 28 °C to measure the humidity coefficient.

Typically, optical fiber systems operate in the second (approximately 1310 nm) or third (approximately 1550 nm) telecommunication windows, where the fiber attenuation is as low as ≤ 0.5 dB/km and ≤ 0.2 dB/km, respectively. To confirm the temperature and humidity characteristics of the optical fiber in the second and third windows, the temperature and humidity coefficients are measured at both optical wavelengths of 1310 nm and 1550 nm.

Measurement Result of Temperature Coefficient

The temperature is changed by 2 °C every 2 h from 20 to 35 °C. The phase of PSOF (SIG) is measured by the RF phase of S21 and the system phase drift (REF) is measured by the RF phase of S43. The calibrated phase drift (CAL) is obtained by subtracting REF from SIG (CAL = SIG - REF). Temperature and humidity sensors are installed inside the TC and THC to ensure the real-time temperature and relative humidity are monitored. Figure 4.9(a) shows the measurement result of the REF and SIG phase drift in PSOF with an optical wavelength of 1310 nm. The REF phase drift is as small as 0.055° and the SIG phase drift is changed owing to the PSOF temperature change. Figure 4.10(b) represents the CAL phase drift of PSOF and temperature change inside THC. The CAL phase has strong negative correlation with the temperature inside THC. The linear fitting equation is shown in Fig. 4.9(c). The temperature coefficient is -0.2612°/120 m/℃ which corresponds with the transmission time delay of -2.1168 ps/km/℃ at 2856 MHz.

The same setup is adopted to measure the temperature and humidity coefficients of PSOF with a wavelength of 1550 nm. The result is shown in Fig. 4.10. The temperature coefficient is -0.2365°/120 m/℃, which corresponds with the transmission time delay of -1.9169 ps/km/℃ at 2856 MHz. The temperature coefficient difference is 0.0247°/120 m/℃, corresponding to 0.2 ps/km/℃ at 2856 MHz, as shown in Fig. 4.11.

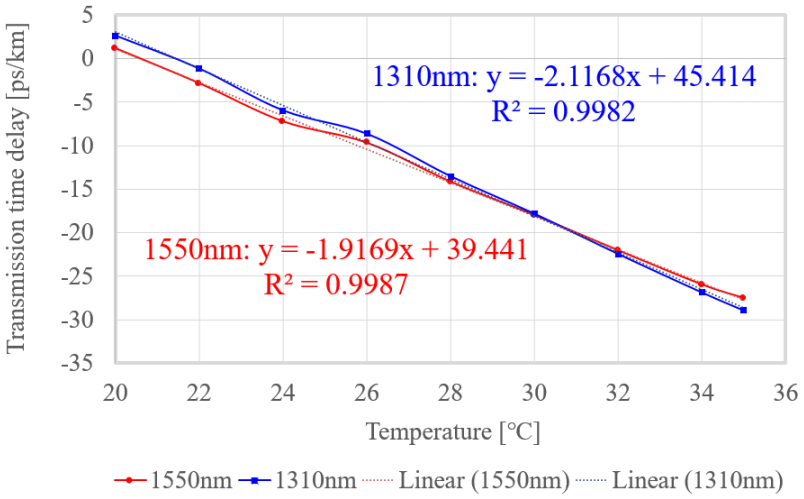

Figure 4.11: Thermal transmission time delay of PSOF with 1310 nm and 1550 nm.

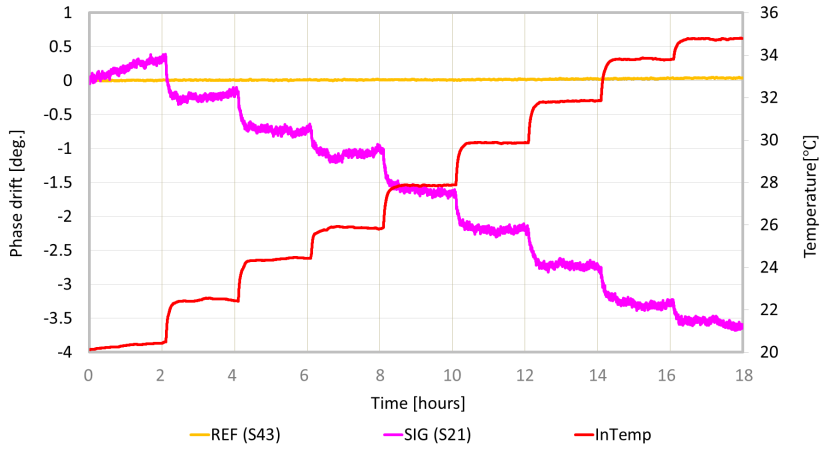

(a) REF, SIG phase of PSOF vs. temperature inside THC.

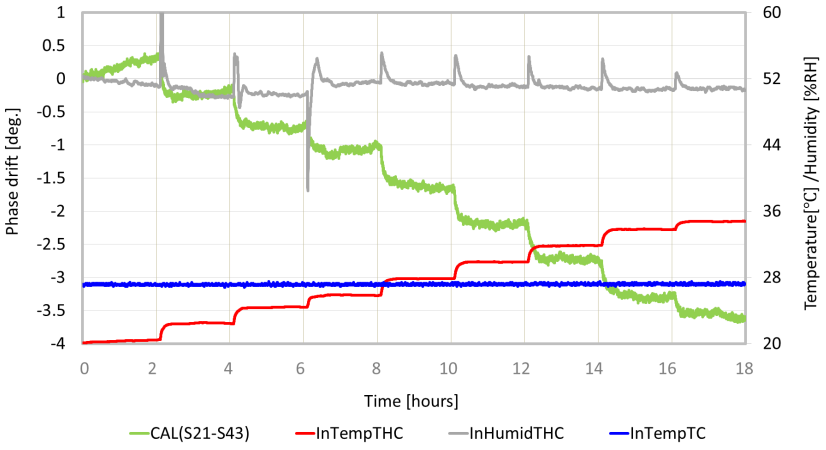

(b) CAL phase of PSOF vs. temperature inside THC.

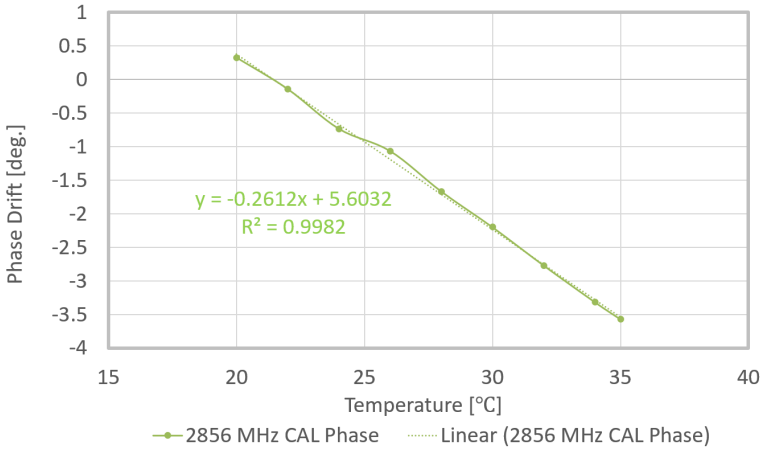

(c) Linear fitting between 2856 MHz CAL phase and temperature.

Figure 4.9: Temperature coefficient measurement of PSOF with a wavelength of 1310 nm.

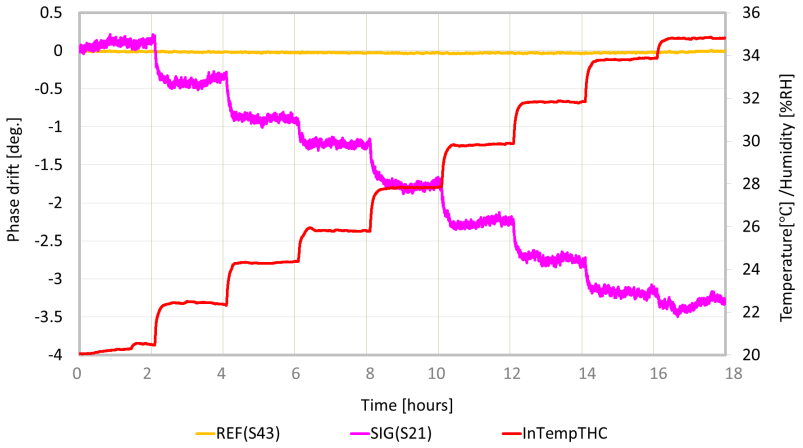

(a) REF, SIG phase of PSOF vs. temperature inside THC.

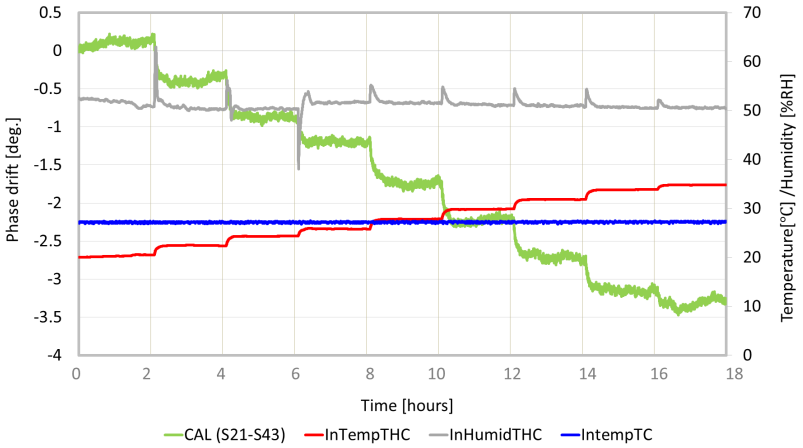

(b) CAL phase of PSOF vs. temperature inside THC.

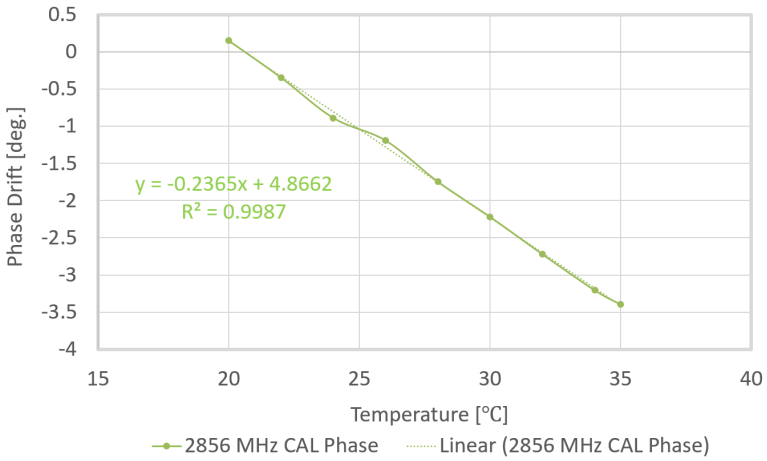

(c) Linear fitting between 2856 MHz CAL phase and temperature.

Figure 4.10: Temperature coefficient measurement of PSOF with a wavelength of 1550 nm.

Measurement Result of Humidity Coefficient

Considering the standard control range of THC, the humidity is changed from 30 %RH to 70 %RH with a fixed temperature of 28 °C to measure the humidity coefficient. The moisture needs more time to affect the optical fiber. Thus, the relative humidity is changed 10 %RH per 10 h from 30 %RH to 70 %RH. The measurement result is shown in Fig. 4.12. The CAL phase of PSOF has positive correlation with relative humidity. Unfortunately, the temperature is not controlled well from 30 %RH to 50 %RH, as shown in Fig. 4.12(b). The temperature fluctuation is up to 1.5 °C which induces external phase drift. This temperature induced phase error (TPE) is estimated to be -0.39° based on the measured temperature coefficient -0.2612°/120 m/°C. This error is removed from the CAL phase. The corrected CAL phase is used to estimate the humidity coefficient of PSOF. The humidity coefficient is 0.0799°/120 m/%RH, which corresponds the transmission time delay of 0.6475 ps/km/%RH at 2856 MHz.

With the same setup and data analysis method, the result of measuring the humidity coefficient with a wavelength of 1550 nm is shown in Fig. 4.13. The TPE is also rejected from the CAL phase. The humidity coefficient is 0.7°/120 m/%RH, which corresponds with the transmission time delay of 0.5674 ps/km/%RH at 2856 MHz. The humidity coefficient difference is 0.0099° /120 m/%RH, corresponding to 0.08 ps/km/%RH at 2856 MHz, as shown in Fig. 4.14. The difference between the coefficient of temperature and humidity is due to the optical wavelength difference of 240 nm (1310 nm, 1550 nm), which is explained in detail in Section 4.1.2.

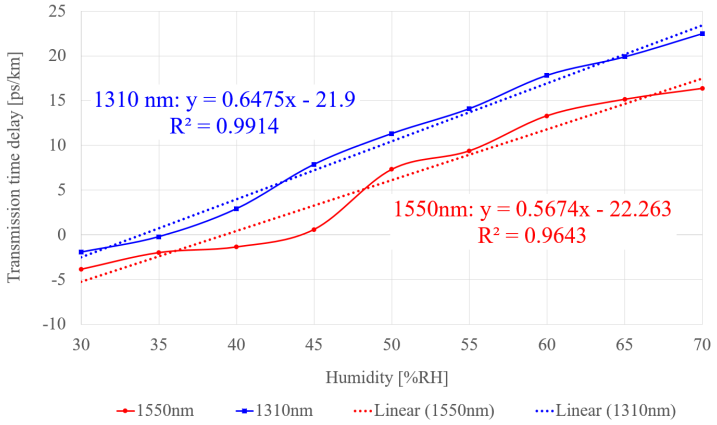

Figure 4.14: Transmission time delay (humidity) with wavelengths of 1310 nm and 1550 nm.

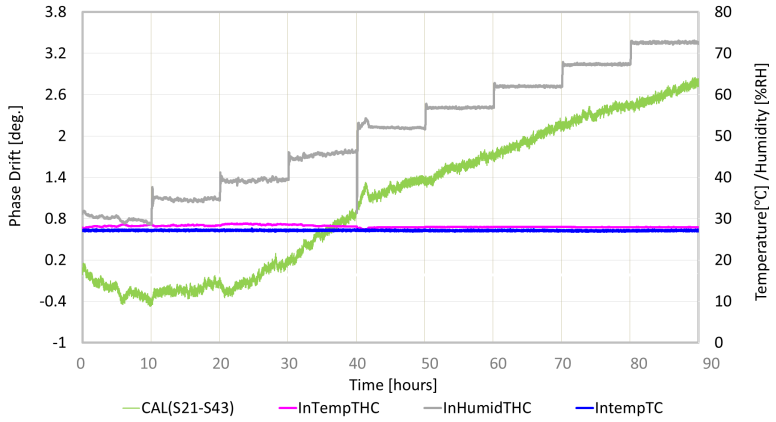

(a) CAL (SIG-REF) phase vs. temperature/humidity inside THC.

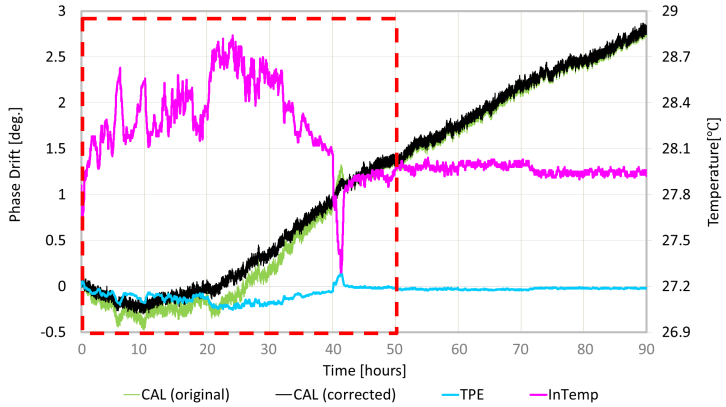

(b) Inside temperature induced phase drift.

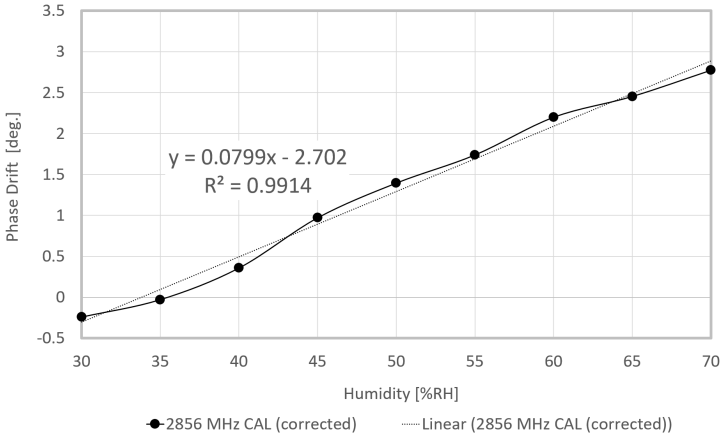

(c) Linear fitting between CAL phase (corrected) and humidity.

Figure 4.12: Humidity coefficient measurement of PSOF with a wavelength of 1310 nm.

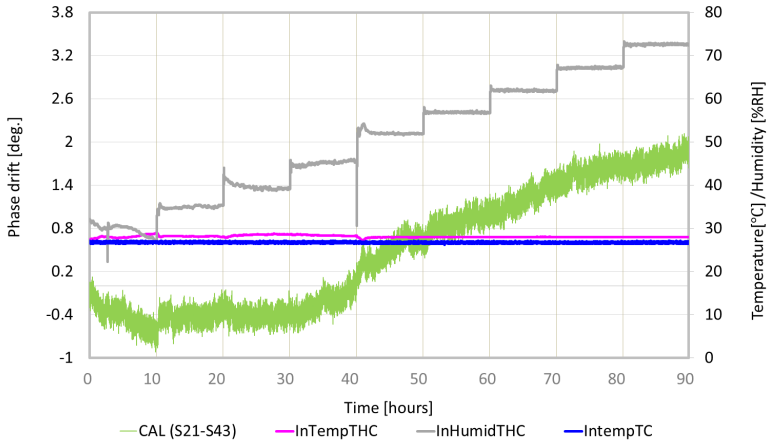

(a) CAL (SIG-REF) phase vs. temperature/humidity inside THC.

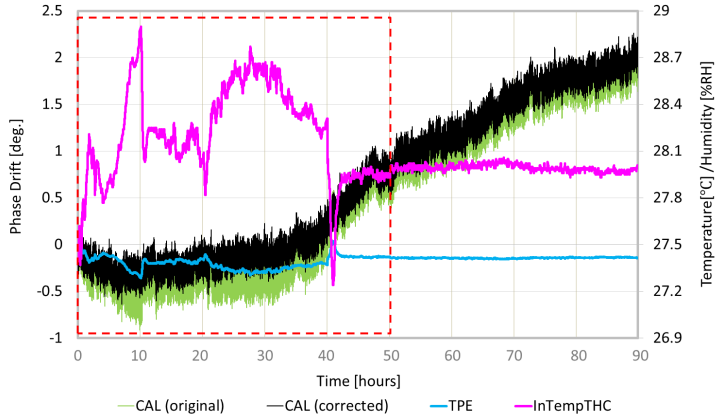

(b) Inside temperature induced phase drift.

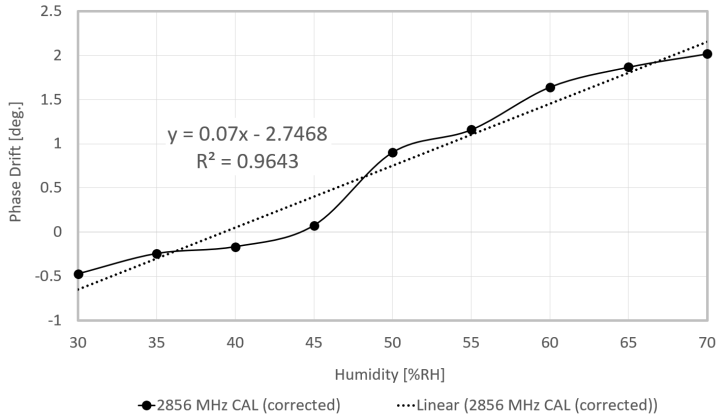

(c) Linear fitting between CAL phase (corrected) and humidity.

Figure 4.13: Humidity coefficient measurement of PSOF with a wavelength of 1550 nm.

4.3.2 Measurement Setup for E/O and O/E modules

The E/O and O/E modules are mostly used as one pair. The setup of temperature and humidity coefficient measurement for one pair of E/O and O/E modules is shown in Fig. 4.15. A short optical link including one pair of E/O and O/E module with 1 m optical fiber is situated inside the THC to change the temperature and humidity near the E/O and O/E module. The phase change is measured by ports 3 and 4 of NA (S43). To reject the system phase drift, the same length of coaxial cable is adopted and its phase drift is monitored by ports 1 and 2 (S21) for reference. Only the 1310 nm wavelength is measured to analyze the contribution of E/O and O/E modules to the long optical link at SuperKEKB injector LINAC.

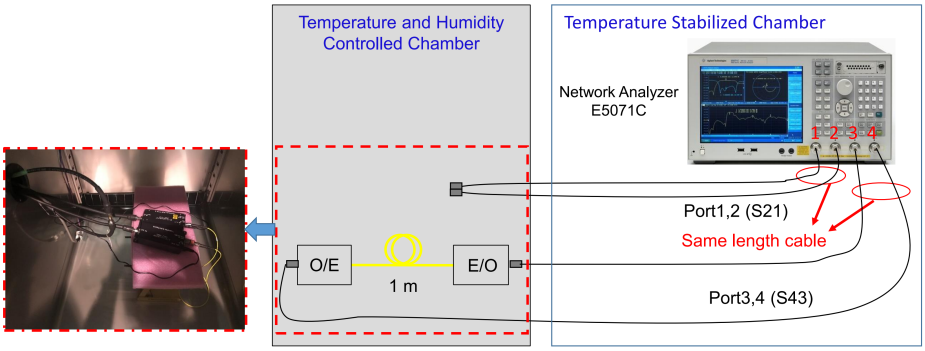

Figure 4.15: Configuration of the test system for one pair of E/O and O/E modules.

Measurement Result of Temperature Coefficient

The optic components of E/O and O/E modules are covered by a sealed box, indicating that temperature requires time to show any effects. The temperature inside THC is changed by 5 °C per 5 h from 25 to 40 down to 25 °C with a stable relative humidity of 50%RH. The phase of SOPT (SSIG) and the reference coaxial cable (SREF) are measured by S43 and S21 of NA, respectively. The calibrated phase drift of SOPT (SCAL) is obtained by subtracting SREF from SSIG (SCAL = SSIG - SREF). Figure 4.16(a) shows the measurement result of the SREF and SSIG phase drifts of SOPT with an optical wavelength of 1310 nm. A part of the reference cable is inside the THC so that the SREF phase drifts by 0.3° due to the temperature change inside THC. The SIG phase drifts 9.73°. As shown in Fig. 4.16(b), the SCAL phase has strong negative correlation with the temperature inside THC. The linear fitting equation is shown in Fig. 4.16(c). The temperature coefficient

is -0.6327°/℃ corresponding to -0.6154 ps/℃ at 2856 MHz.

Measurement Result of Humidity Coefficient

For humidity coefficient measurement, it is necessary to keep the temperature very stable when the relative humidity is changed. As shown above, the temperature coefficient of the E/O and O/E modules is very large such that the temperature stability will significantly influence the observed phase drift. To maintain a stable temperature, the relative humidity is changed between 40 %RH and 70 %RH with a fixed temperature of 30 °C; however, it is different from the normal operation status. The relative humidity is changed by 10 %RH per 10 h from 40 %RH to 70 %RH down to 40 %RH. The measurement result is shown in Fig. 4.17.

As shown in Fig. 4.17(a), the SCAL (SSIG-SREF) phase has negative correlation with the relative humidity inside THC. However, there are two big phase jumps in the dotted circle line when the relative humidity is changed from 40 %RH up to 50 %RH and 50 %RH down to 40 %RH. To analyze the source of the phase jump, the temperature inside the THC is illustrated in Fig. 4.17(b) and it is evident that there are temperature fluctuations of $-0.8\,^{\circ}\mathrm{C}$ at the phase jump points. The temperature induced phase error of SOPT (STPE) is estimated to be $+0.51^{\circ}$ according to the temperature coefficient -0.6327°/℃. This phase jump is well compensated, as represented via black lines. The corrected SCAL phase (CSCAL) is used to estimate the humidity coefficient of the E/O and O/E modules. As shown in Fig. 4.17(c), the humidity coefficient is -0.0352°/%RH, corresponding to -0.0342 ps/%RH at 2856 MHz.

4.4 Summary of Temperature and Humidity Coefficients

The temperature and humidity coefficients of PSOF at wavelengths of 1310 nm and 1550 nm and one pair of E/O and O/E modules at 1310 nm are measured. The temperature and humidity coefficients and the test environment are summarized in Tables 4.3 and 4.4, respectively. The humidity coefficient is much smaller than the temperature coefficient. However, the temperature is stabilized within $\pm 1\,^{\circ}\mathrm{C}$ and the humidity is not controlled in the LINAC gallery. Although the humidity coefficient is very low, large relative humidity fluctuation was monitored from 10-50%RH during one year (May 2017-2018). Therefore, the phase drift due to the humidity fluctuation becomes serious.

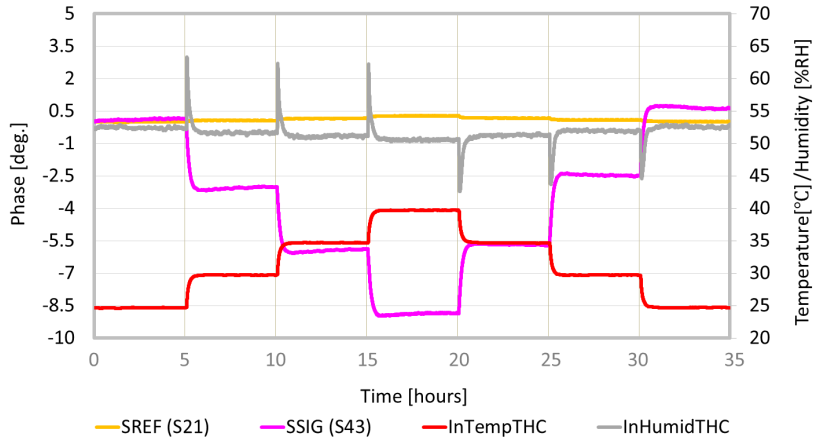

(a) SREF, SSIG phase of SOPT vs. temperature inside THC.

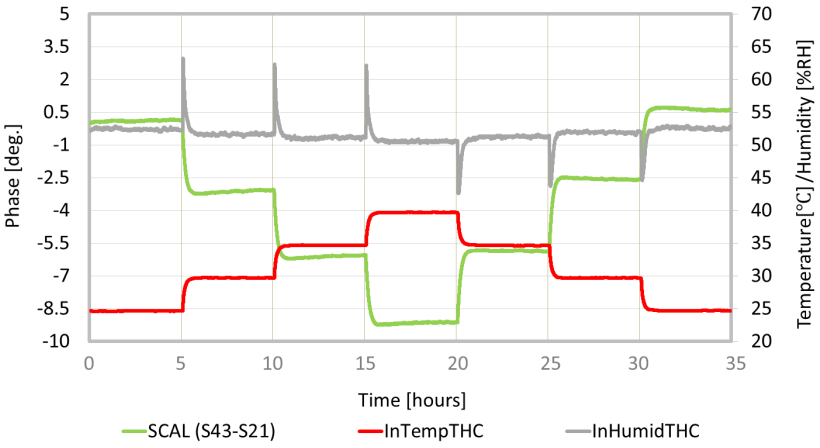

(b) SCAL phase of SOPT vs. temperature inside THC.

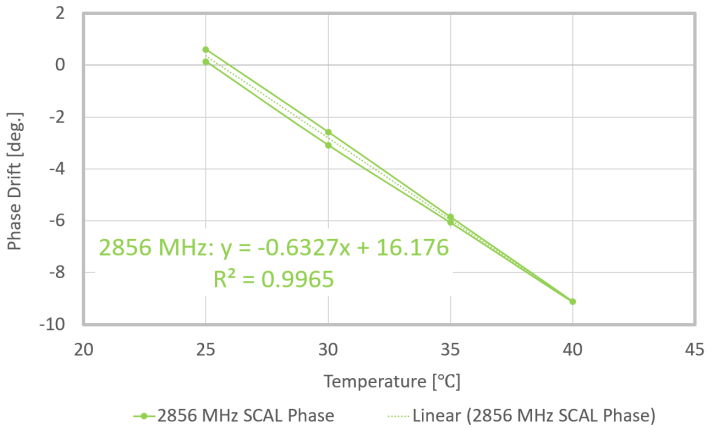

(c) Linear fitting between SCAL phase and temperature.

Figure 4.16: Temperature coefficient measurement of E/O and O/E modules with a wavelength of 1310 nm.

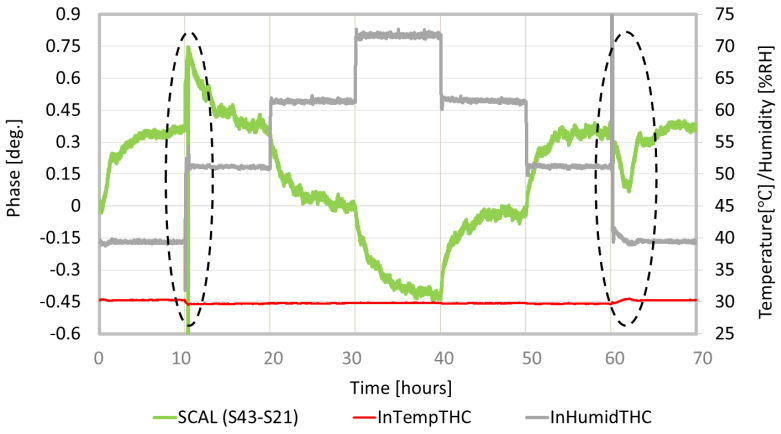

(a) SCAL (SSIG-SREF) phase vs. temperature/humidity inside THC.

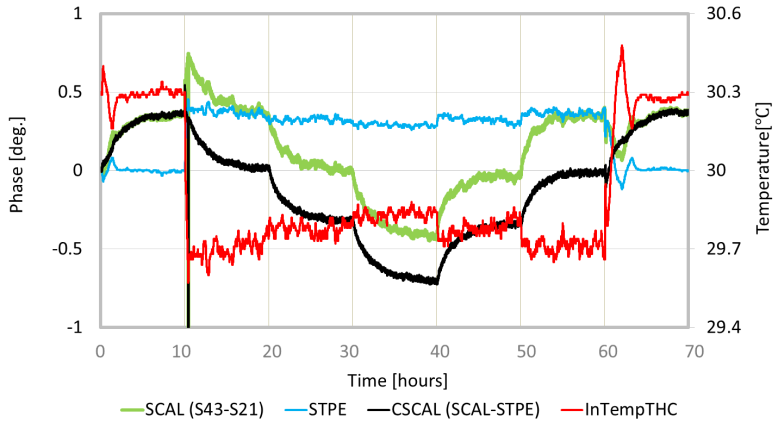

(b) Inside temperature induced phase drift.

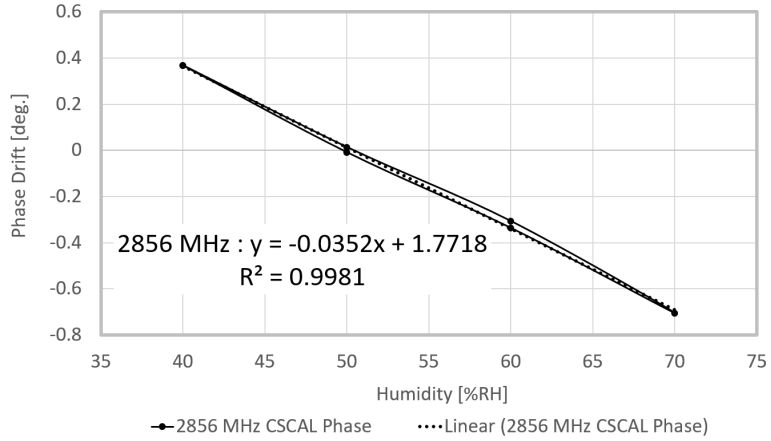

(c) Linear fitting between CSCAL phase and humidity.

Figure 4.17: Humidity coefficient measurement of E/O and O/E modules with a wavelength of 1310 nm.

As mentioned in Section 4.2, the humidity and temperature fluctuations were monitored to be 24%RH and ±1 °C, respectively, in the LINAC gallery. The outside humidity was roughly the same as the inside humidity. According to the temperature and humidity coefficients with a wavelength of 1310 nm, the phase drift of 600 m PSOF is roughly estimated to be 9.6° by humidity fluctuation and ±1.3° by temperature fluctuation. Therefore, the total phase drift is estimated from 8.3° to 10.9°. The measured phase drift of 600 m PSOF in Section 3.5.2 is 9.77°, which is located in the estimation range. The E/O and O/E modules are located inside the temperature stabilized chamber, where the temperature is controlled within ±0.1 °C. The phase drift of the E/O and O/E modules is estimated to be 0.845° by humidity fluctuation and ±0.063° by temperature fluctuation. Therefore, the phase drift is 0.9°. The measured phase drift of the E/O and O/E modules is 1.47°. The estimated phase drift almost matches with the measured result but not precisely. One possible reason is that the measured value is calculated by data analysis including the measurement error. Another possible reason is that the humidity and temperature fluctuations are not accurate. Finally, the humidity and temperature range of the temperature and humidity coefficients are not exactly the same as the real environment in the LINAC gallery. We can use the temperature and humidity coefficients to roughly estimate the phase drift. It is very useful for the phase stabilization system.

For PSOF, it is found out that the temperature and humidity coefficients are different at different operation wavelengths (1310 nm, 1550 nm). The wavelength difference affects the transmitted phase stability in the RF reference phase stabilization system.

Table 4.3: Temperature Coefficient of PSOF, E/O and O/E modules. WL: Wavelength, TEMP: Temperature, HUMI: Humidity.

	WL	**TEMP**	**HUMI**	**Coefficient**	**Time Delay**
PSOF	1310 nm	20-35 °C	50%RH	-0.2612°/120m/°C	-2.1168 ps/km/°C
PSOF	1550 nm	20-35 °C	50%RH	-0.2365°/120m/°C	-1.9169 ps/km/°C
E/O+O/E	1310 nm	25-40 °C	50%RH	-0.6327°/°C	-0.6154 ps/°C

Table 4.4: Humidity Coefficient of PSOF, E/O and O/E modules.

	WL	**TEMP**	**HUMI**	**Coefficient**	**Time Delay**
PSOF	1310 nm	28 °C	30-70%RH	0.08°/120m/%RH	0.6475 ps/km/%RH
PSOF	1550 nm	28 °C	30-70%RH	0.07°/120m/%RH	0.5674 ps/km/%RH
E/O+O/E	1310 nm	30 °C	40-70%RH	-0.0352°/%RH	-0.0342 ps/%RH

Chapter 5

Drift Compensation for Phase Monitor System

Phase detectors with high stability and accuracy are required by many systems in particle accelerators, such as the LLRF system and the RF reference phase distribution system. The RF phase must be measured with high accuracy on the scale of tens of femtoseconds or even sub-10 fs for several hours or days. The long-term measurement stability of a phase monitoring system is mainly affected by environmental changes such as the variations in temperature and humidity.

The RF signal with very high frequency (such as 2856 MHz) is usually down-converted to an IF signal, digitized, and processed in an FPGA board. In the synchronization system, the phase monitoring system is used to measure the phase drift between a reference signal from MO and the RF signal distributed to a remote location. Many RF components are used in the front-end circuit such as mixer, BPF, power splitter, and coaxial cables. Temperature and humidity drifts of these RF components are not perfectly correlated, and they induce long-term measurement error.

In this chapter, the phase drift of the phase monitoring system is presented. The sources of phase drift are analyzed. Several solutions for phase drift compensation are proposed, such as two-tone calibration (TTC) implemented by the Lawrence Berkeley National Laboratory (LBNL) and drift compensation module (DCM) developed by DESY. A method called reference tracking (RTC) is used at the SuperKEKB injector LINAC. The long-term performance is evaluated. Finally, the performance of RTC and DCM is compared.

5.1 Monitoring System Phase Drift

Several techniques are applied to detect the RF phase [38]. At Injector LINAC, the 2856 MHz RF phase is detected using the oversampling technique, as described in Chaper 3. The down-conversion stage is necessary. Two different FPGA boards are applied to measure the phase drift of four optical links at LINAC. As shown in Fig. 3.9, the 2856 MHz RF reference signal is split into four: two are used for LO generation for both FPGA boards and the other two are used as references to the two FPGA boards, individually. These two reference signals are measured by an ADC of two FPGA boards, which enables the evaluation of the monitoring system phase drift. The long-term phase drift of each monitoring system is shown in Fig. 5.1. The time slot is the same as in Section 3.5. The phase drifts in REF1 and REF2 indicate the phase drift of the monitoring system based on FPGA board 1 and FPGA board 2, respectively. The system drifts of board 1 and board 2 are 4.45° and 3.97°, respectively. Although the same LO is used, a phase difference of 0.48° was observed between the two monitors. The monitor system is situated inside the temperature stabilized chamber with a stability of ±0.1 °C at sector 1 but there is no humidity regulation. Thus, the humidity fluctuation at sector 1 is observed as 26%RH presented in Fig. 5.1. It was found that the system phase drift depended on humidity and the phase drift lagged behind the humidity change for ∼ 7 h. Coaxial cable (Candox 5B-008X-23-23-10000) and a normal cavity-type BPF were used.

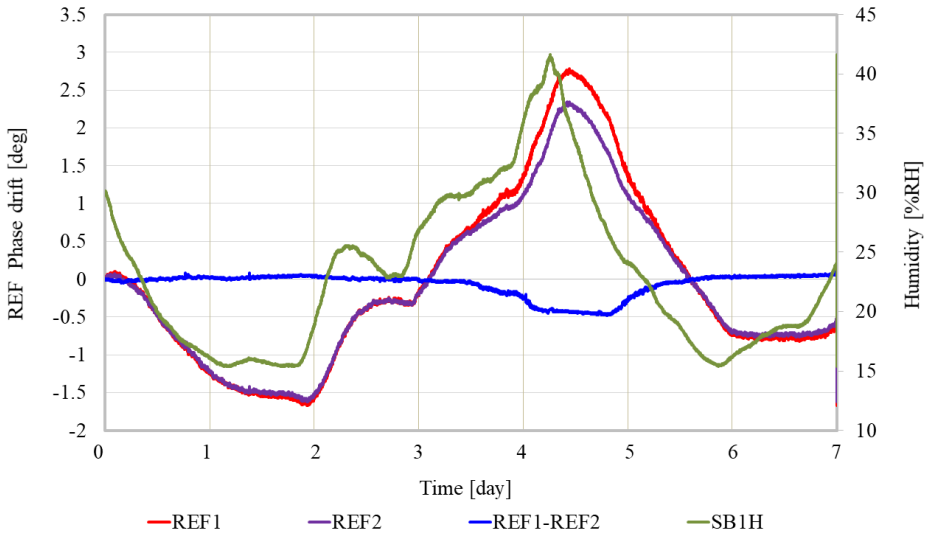

Figure 5.1: Long-term phase drift of the monitoring system at injector LINAC.

5.2 Sources of Phase Drift

The sources of such large system phase drift are the front-end circuit (e.g., mixer, BPF, LPF, attenuator, and coaxial cable) and the FPGA board (e.g., chips, electric components, and printed circuit board (PCB) routing). They are very sensitive to the fluctuation in temperature and humidity. It was found that the system phase drift is suppressed by the changes in the type of coaxial cable and BPF.

5.2.1 Coaxial Cable

The delay stability of the coaxial cable is very sensitive to temperature and humidity. In LO generation, several coaxial cables are used to connect the RF components and the phase drift from the coaxial cable can make significant contributions to the system phase drift. Initially, a type of coaxial cable commercialized by Candox system Inc. (Candox 5B-008X-23-23-10000) [56] was used, as shown in Fig. 5.2(a). The result in Fig. 5.1 is based on this type of coaxial cable and the system phase drift is very large. The detailed data on delay stability caused by temperature and humidity are generally not available to the manufacturers. To choose a coaxial cable with low temperature and humidity coefficient, five types of cables, commonly used in our laboratory, were ordered and tested. Their performances are shown in Appendix A.

(a) Coaxial cable commercialized by Candox system Inc., initially used in the monitoring system.

(b) Coxial cable commercialized by HUBER+SUHNER, newly selected to reduce the monitoring system phase drift.

Figure 5.2: Coaxial cable used in the monitoring system.

A similar test system, as shown in Section 4.3, is constructed. The coaxial cable is located inside the temperature and humidity controlled chamber.

By changing the temperature with stable humidity, the temperature coefficient is calculated at 2856 MHz. Similarly, by changing the humidity with stable temperature, the humidity coefficient is estimated. The detailed data and measurement result is summarized in A. The temperature and humidity coefficients of the Candox cable are 145 ps/km/°C and −23 ps/km/%RH, respectively. Its delay stability is the most sensitive to both temperature and humidity, in comparison to other four types. The temperature of the monitoring system is stabilited but the humidity remains uncontrolled. To reduce the phase drift from the coaxial cable, a coaxial cable ($S0472B$) commercialized by HUBER+SUHNER [57] is chosen owing to its lowest humidity coefficient −0.25 ps/km/%RH and its second lowest temperature coefficient −30 ps/km/°C. The temperature and humidity coefficients are improved by five and 92 times, respectively.

The newly selected HUBER+SUHNER cable is used to connect the RF components instead of the Candox cable. Figure 5.3 describes the phase drift of the monitoring system using the HUBER+SUHNER cable with temperature and humidity fluctuations. The temperature is well stabilized but the humidity fluctuation is 18%RH. The phase drift of the monitoring system is improved from 4.45° ($\Delta H = 26\%RH$) to 0.45° ($\Delta H = 18\%RH$).

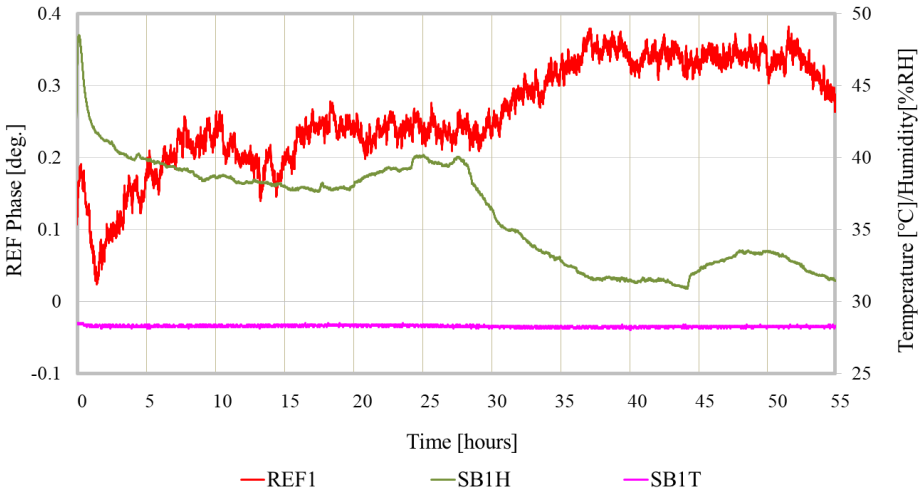

Figure 5.3: Phase drift of the monitoring system using HUBER+SUHNER cable.

5.2.2 Band Pass Filter

The other main source of the system phase drift is the BPF used in LO generation. Figure 5.4 shows the photo of cavity-type BPF with narrow band-

width. The center frequency is 2870 MHz and the bandwidth is ±5 MHz. In the beginning, a normal type is initially used in the monitoring system, as shown in Fig. 5.4 (a). The temperature and humidity coefficients are −1.82°/°C and −0.11°/%RH at 2870 MHz, respectively. It is very sensitive to humidity. This phenomenon was first found in the LLRF system of the compact energy recovery LINAC (cERL) at KEK [45]. The system phase drift is suppressed after enclosing the BPF with desiccant (silica gel) in a box. Thus, a waterproof BPF is customized to reduce the monitoring system phase drift. The temperature and humidity coefficients are measured to be −1.73°/°C and −0.0037°/%RH at 2870 MHz, respectively. The sensitivity to the temperature is almost the same but it is insensitive to humidity fluctuation.

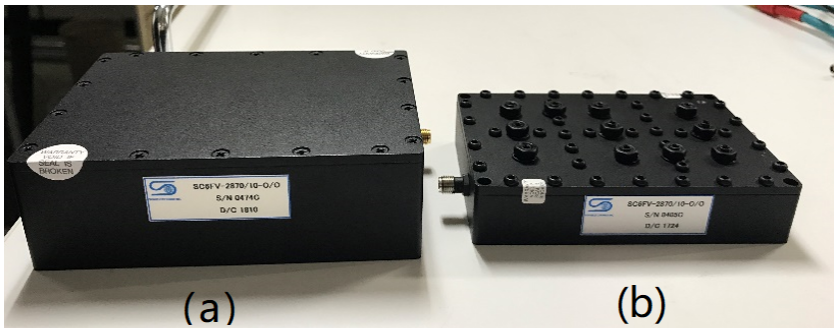

Figure 5.4: BPFs used in the monitoring system. (a) Customized waterproof type BPF to reduce the monitoring system phase drift, (b) normal cavity-type BPF, initially used in the monitoring system.

5.3 System Phase Drift Compensation

In addition to the coaxial cable and BPFs, there are many other RF components such as mixer, power splitter, attenuator, and amplifier that are also used in the monitoring system. It is difficult to measure and compare the temperature and humidity coefficients one by one and change all components. Howerve, some components that are highly sensitive to environment changes can be sealed but a small phase drift still remains. A few methods to compensate the monitoring system phase drift have been proposed for CW and pulse machine. The schematic design and long-term performance are presented and compared.

5.3.1 Two-Tone Calibration for CW Machine

In the synchronization system, the phase monitoring system measures the phase drift between a reference signal and the RF signal distributed to a remote location to evaluate the performance of the phase stabilization system. The RF signal is down-converted to an IF signal and the RF phase is measured. As shown in Fig. 5.5, a CW double side-band suppressed carrier signal (DSB-SC) is added to the RF signal as a common mode between both channels, which is called a calibration signal (CAL). The phase drift in the front-end circuit is measured by this CAL signal and the system phase drift can be compensated. This method is proposed by LBNL and known as two-tone calibration [58]. This technique can be applied in the synchronization system, LLRF system, and potentially other accelerator subsystems.

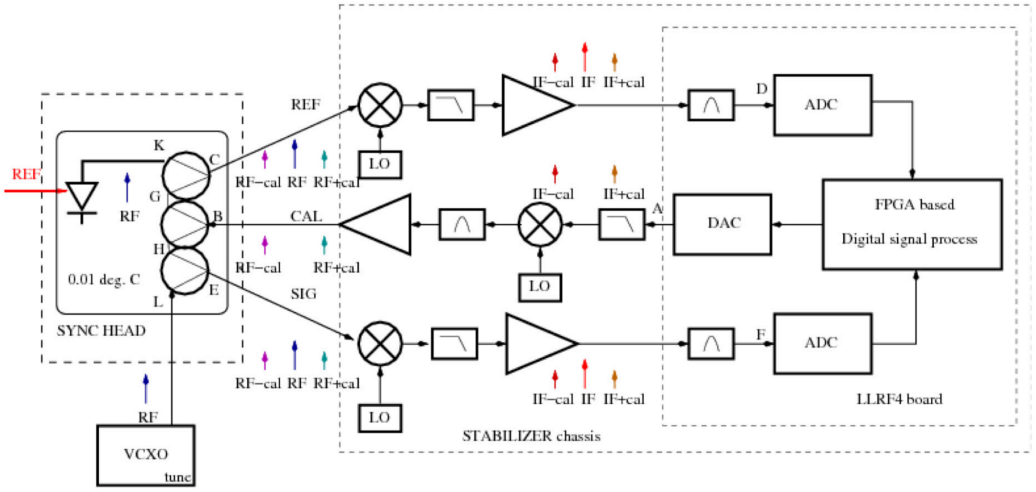

Figure 5.5: Schematic diagram of the two-tone calibration method [58].

At the receiver side, the signal from a voltage-controlled crystal oscillator (VCXO) (SIG) should follow the stable reference (REF) from the fiber link. To measure the phase drift between SIG and REF, the front end circuit with TTC contains two down-converted channels (REF, SIG) and one up-converted channel (CAL). The DSB-SC signal with the frequency of 1 MHz (cal) is synthesized by a DAC and up-converted to a CAL signal with the frequency of RF±cal by a mixer. The CAL signal is split into two: one is combined with the RFF signal and propagated from C to D, the other is combined with the SIG signal and propagated from E to F. In the sync head, the phase delay in the signal path inside the splitter and combiners are not common to both signals and cannot be canceled; thus, the sync head is well

temperature stabilized within a stability of 0.01 °C. The algorithm and the signal processing are explained in detail in [58]. The phase accuracy of the monitoring system achieved 15 millidegrees (rms) at 2856 MHz corresponding to 13 fs.

This method is further studied and applied at DESY. It is applied in the phase detection at 1.3 GHz using the undersampling technique [59] and can be extended to a measurement bandwidth of up to 3.0 GHz or 3.9 GHz using the oversampling technique [60]. Figure 5.6 shows the simplified scheme of the phase drift detector at 1.3 GHz using the undersampling technique with a two-tone calibration circuit. The phase detector is located in a temperature controlled chamber. As shown in Fig. 5.7(a), the temperature is changed from 18 °C to 33 °C and down to 18 °C with 1 °C per 30 min. The relative humidity fluctuation is $\sim$ 10%RH. During the measurement, the calibration circuit consisting of a power splitter and two combiners was temperature stabilized within $\pm$0.1 °C and humidity stabilized within $\pm$0.1%RH.

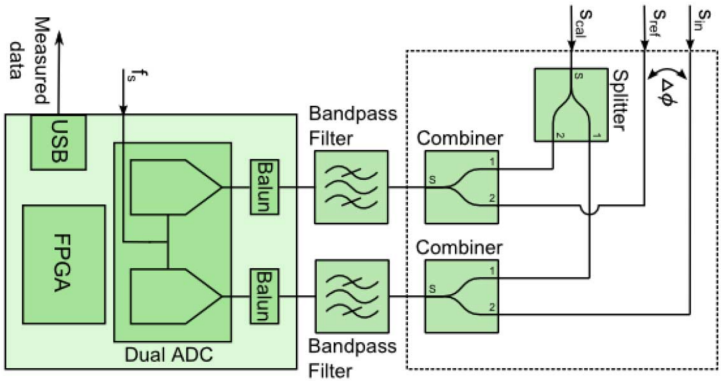

Figure 5.6: Simplified scheme of the phase drift detector at 1.3 GHz using undersampling technique with a two-tone calibration circuit [59].

The long-term stability with and without the TTC circuit is shown in Fig. 5.7(b). Without the TTC circuit, the system phase drift depended on the temperature change and a phase drift of 0.023° (pk-pk) was observed corresponding to 50 fs at 1.3 GHz. With TTC circuit, the phase drift is suppressed within 0.01° (pk-pk) corresponding to 22 fs. It is concluded that the system phase drift can be smaller without the down-conversion stage (system phase drift is in hundreds of femtoseconds level with down-conversion at injector LINAC but in tens of femtoseconds level without down-conversion), and the TTC circuit is effective in compensating the system phase drift for CW machines. However, the TTC method is very complicated in the algo-

rithm and implementation (programming).

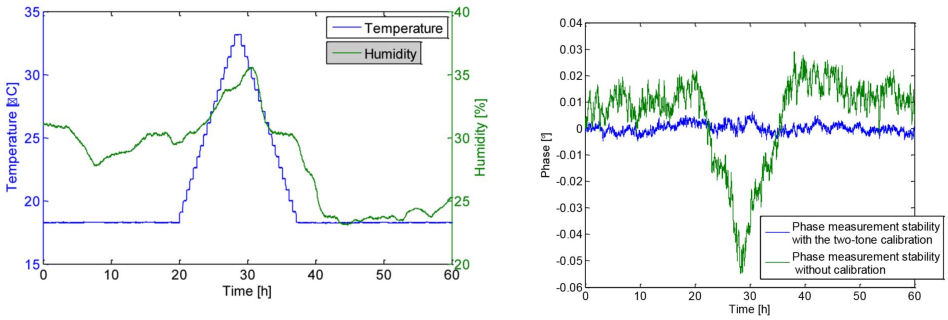

(a) Temperature and humidity change inside the chamber.

(b) Long-term stability with/without the two-tone calibration circuit.

Figure 5.7: Long-term stability with/without the two-tone calibration circuit and the environment change where the phase detector is located [59].

5.3.2 Drift Compensation Module for Pulse Machine

In the pulse machine, the reference signal is not always required. A drift compensation module with an RF switch is developed to compensate the monitoring system phase drift at DESY for pulse machine [61]. The schematic diagram of DCM used for the LLRF system is shown in Fig. 5.9. An RF switch is applied before the LLRF system.

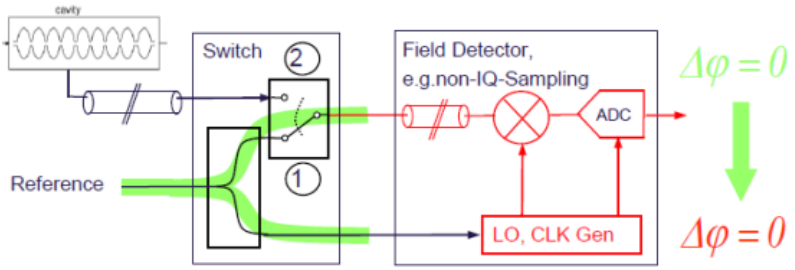

Figure 5.8: Schematic diagram of drift compensation module [61].

The procedure of phase drift compensation consists of two stages:

(1) Before the filed detection, the RF switch is connected to position ① (reference signal) to measure the system phase drift. This phase drift is calculated and compensated inside the FPGA board.

(2) After phase drift compensation, the RF switch is connected to position ② to detect the cavity field.

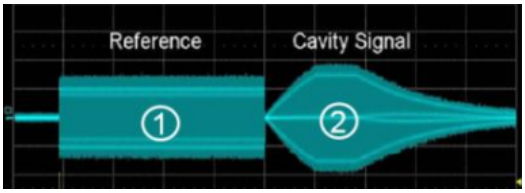

Figure 5.9: Principle of DCM operated for pulse machine [61].

By using this method, the system phase drift and cavity filed are detected by the same front-end board and signal processing board, respectively. This can avoid the phase difference between different ADC channels. However, the phase drift of the RF switch cannot be measured and canceled. The RF switch is carefully sealed with temperature stabilization within 0.005 °C and humidity stabilization within 1%RH. The LLRF system is inside the temperature stabilized rack.

To evaluate the performance of DCM, a test system is constructed, as shown in Fig. 5.10 [62]. A 1.3 GHz RF signal is split into two by a power spliter, which is passive stabilized: one is used as the reference and the other is used as the signal that needs to be measured (e.g., cavity signal). All test systems are located inside the rack. Ideally, the phase drift between the two signals is approximately zero with DCM.

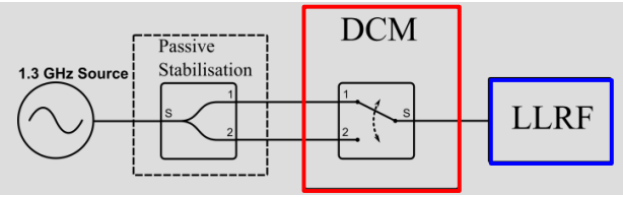

Figure 5.10: Test system for DCM [61].

Figure 5.11 presented the measurement result. By changing the temperature ($\Delta T = 5\,°C$) inside the rack, the phase drift was suppressed from 5° (pk-pk) to 0.02° (pk-pk) at 1.3 GHz. However, this phase stability included the phase drift of the power splitter because it is only passive stabilized. By changing the humidity ($\Delta H = 40\%RH$) inside the rack, the phase drift of the LLRF system was suppressed from 3.3° (pk-pk) to 0.02° (pk-pk) at 1.3 GHz. Thus, it can be concluded that phase stability using DCM can achieve below 0.02° (pk-pk) at 1.3 GHz corresponding to 43 fs. This method is very

simple and easy to implement. However, it should be noted that excellent packaging/sealing is required for the RF switch. Detailed information can be found in [60, 62]. This module is already used in the Free Electron Laser in Hamburg (FLASH) at DESY.

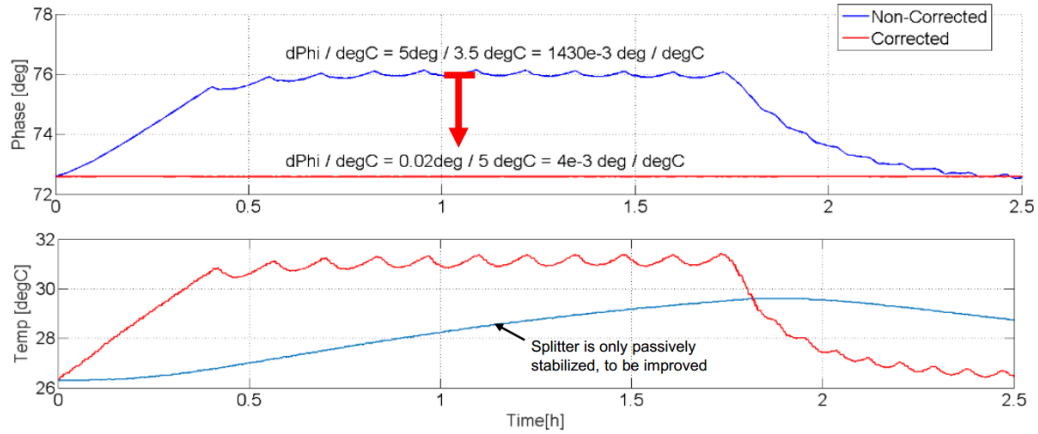

(a) Phase stability with/without DCM by changing temperature.

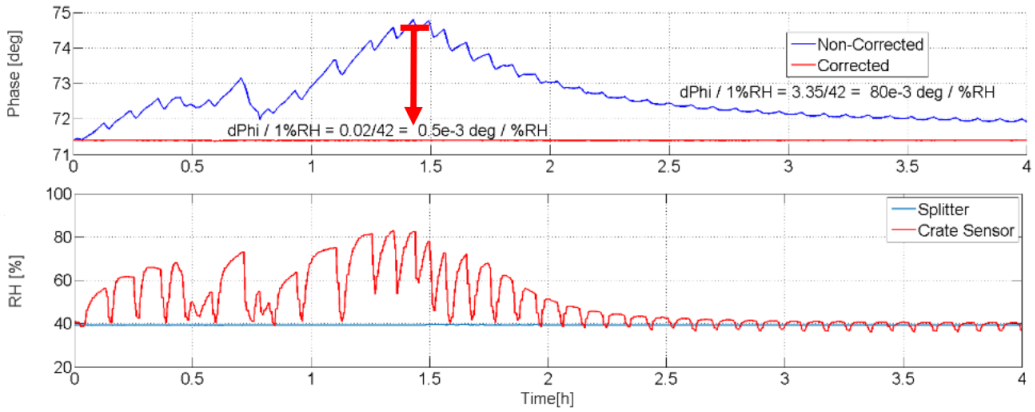

(b) Phase stability with/without DCM by changing humidity.

Figure 5.11: Phase stability with/without DCM by changing temperature and humidity [61].

5.3.3 Reference Tracking

As shown in Fig. 5.12, the reference signal is used for LO and clock (CLK) generation. The reference signal is measured by an ADC and the signal to be monitored is measured by another ADC. The LO and CLK generation is common to both signals. As mentioned above, the phase drift of the reference signal indicates phase drift of the monitoring system. To reject

the system phase drift, the reference phase is directly subtracted from the monitored phase. This method is called reference tracking. It is efficient only for symmetric structures and the RF cable used to connect the RF components should be carefully selected.

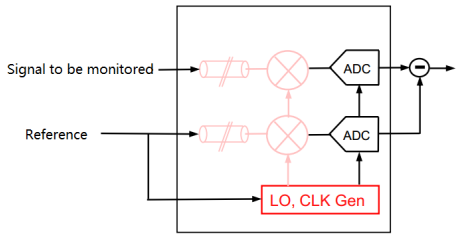

Figure 5.12: Schematic diagram of the reference tracking method for system drift compensation at SuperKEKB injector LINAC.

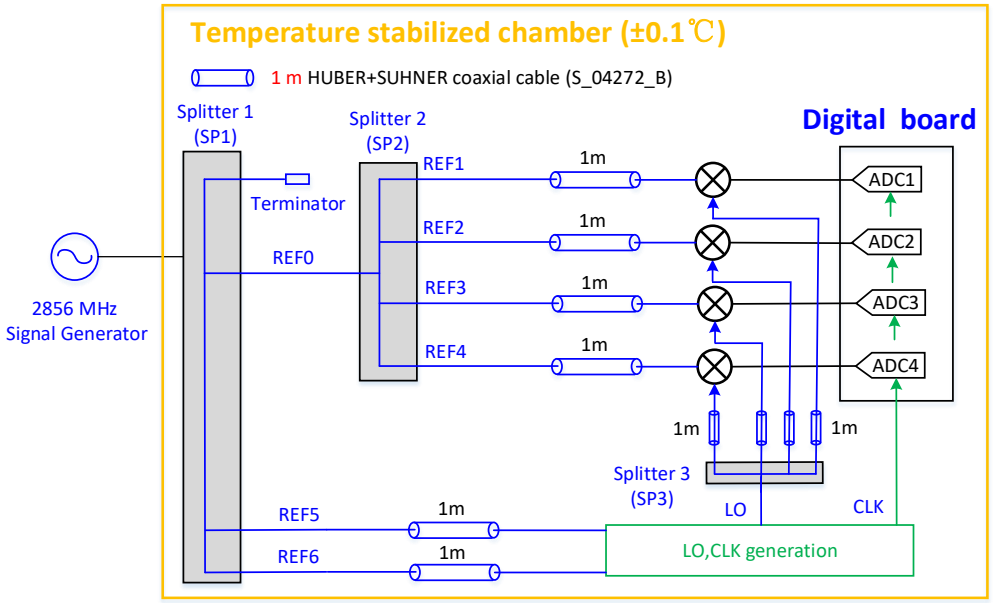

Figure 5.13: Four-channel reference tracking at the test stand.

The method is used in the phase monitoring system at SuperKEKB injector LINAC. To evaluate the long-term performance of RTC, four-channel reference tracking is constructed in the test stand. Figure 5.13 describes the configuration of the 4-channel reference tracking. The 2856 MHz reference

signal is split into three by a four-port power splitter (ZA4PD-S+) from Mini-Circuits [63]. Two signals (REF5, REF6) are used for LO and CLK generation. One (REF0) continues to split into four (REF1, REF2, REF3, REF4). These signals are down-converted to an IF signal by four split LO signals and then measured by four ADCs. The configuration is symmetric and HUBER+SUHNER coaxial cables with 1 m length are used. The system is located inside a chamber that was temperature stabilized with $\pm 0.1\,^{\circ}\mathrm{C}$ but the humidity is not controlled.

Figure 5.14 shows the long-term phase stability with/without the RTC method and environment changes in the monitoring system. The temperature is stabilized within $0.1\,^{\circ}\mathrm{C}$ (pk-pk) and the humidity fluctuation is 11%RH. The system phase drift can be evaluated as 1.3° at 2856 MHz from the phase drift in the reference signals (REF1 to REF4), as shown in Fig. 5.14. It is mainly affected by changes in humidity. Using the TRC method, the system phase drift is significantly suppressed by subtracting the REF1 phase from the phases of other signals.

$$RTCn = REFn - REF1 \tag{5.1}$$

The long-term (80 h) phase drift is suppressed from 1.3° to 0.03° at 2856 MHz corresponding to 28 fs, as presented in Fig. 5.15. Thus, the phase stability with reference tracking method is comparable with two-tone calibration and DCM using good coaxial cable and symmetric structure.

As presented in Fig. 5.15, a small phase drift still remained and the phase drift between ADC4 and ADC1 was smaller than that between ADC2 and ADC1, ADC3, and ADC1. Furthermore, it was found that the residual phase drift was influenced by changes in humidity. The possible source is the phase difference between the four ports of the power splitter and the PCB routing path of the digital FPGA board. Figure 5.16 shows a photo of the structure of the four-port splitter used in the test system. The routing paths between ports 1 and 4 and ports 2 and 3 are symmetric. However, the routing path between port 1 and port 2 is not symmetric. Thus, the path is not exactly the same for the four ports and the time delay caused by the environment is a little bit different for each to port.

In conclusion, the reference tracking method is very simple and easy to implement but it is only effective in a symmetric structure. The RF coaxial cable should be carefully selected and some important RF components (such as the power splitter) should be well sealed. The disadvantage is that it can suppress only the correlated noise, not the uncorrelated noise.

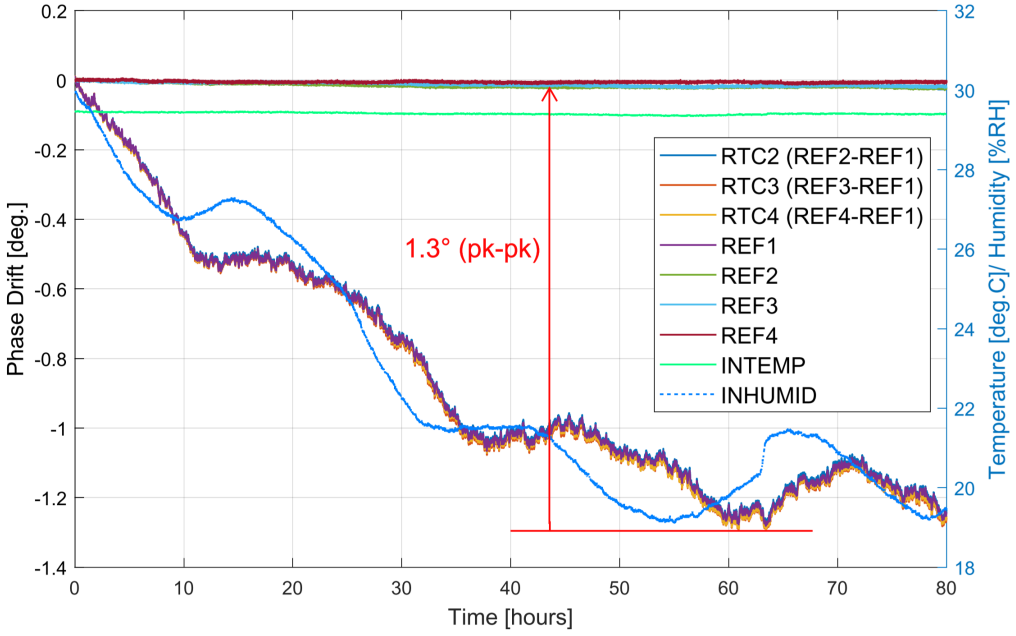

Figure 5.14: System phase drift with/without RTC method and environmental changes inside the chamber.

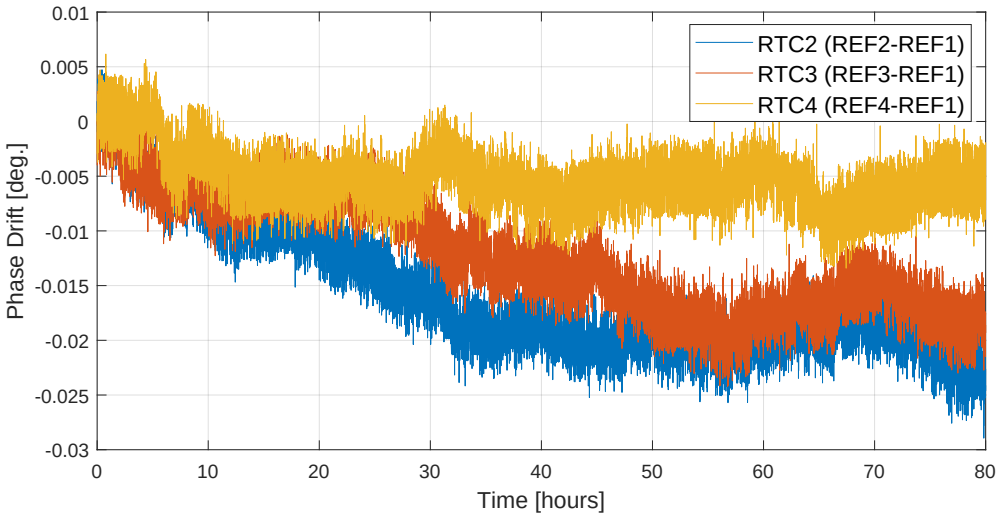

Figure 5.15: System phase drift compensation with RTC method (zoomed data of Fig. 5.14).

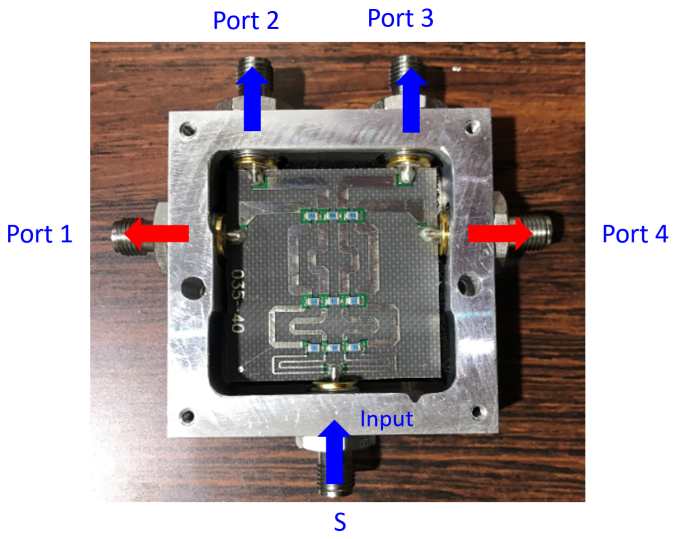

Figure 5.16: Four-port power splitter.

5.3.4 Comparison of System Phase Drift Compensation using DCM and RTC at DESY Test Stand

In the laboratory, both RTC and DCM are demonstrated to compensate the monitoring system phase drift. To compare the long-term performance, a test system using DCM and RTC is constructed at the DESY test stand. Figure 5.17 shows the setup of the test system. A 1300 MHz reference signal is generated by a signal generator. A coupled portion is used to generate the LO and CLK signals with a 2 m coaxial cable (Type 3). The main portion of the reference signal is split into two: one is fed to the DCM module as a reference (REF) and the other is used as the signal that needs to be monitored (SIG). The Type 1 0.5 m coaxial cable is used. The REF signal is split into seven channels and the RF switch is kept on the lower side for the reference tracking mode except channel 1. The SIG signal is fed to channel 1 in the DCM mode. All reference signals are fed to the down converter through the 1 m coaxial cable (Type 2) and the RF phase is detected by the LLRF system used at the European XFEL. The RTC and DCM are not effective exactly at the same time. This test system is operated in pulse mode. It works in the RTC mode in the first RF pulse and then changes to the DCM mode in the next RF pulse. The two modes are operated interchangeably. The duration of the RF pulse is 100 ms. The temperature and humidity induced system phase drift is much slower than the pulse duration. The same system phase drift should be compensated using RTC and DCM.

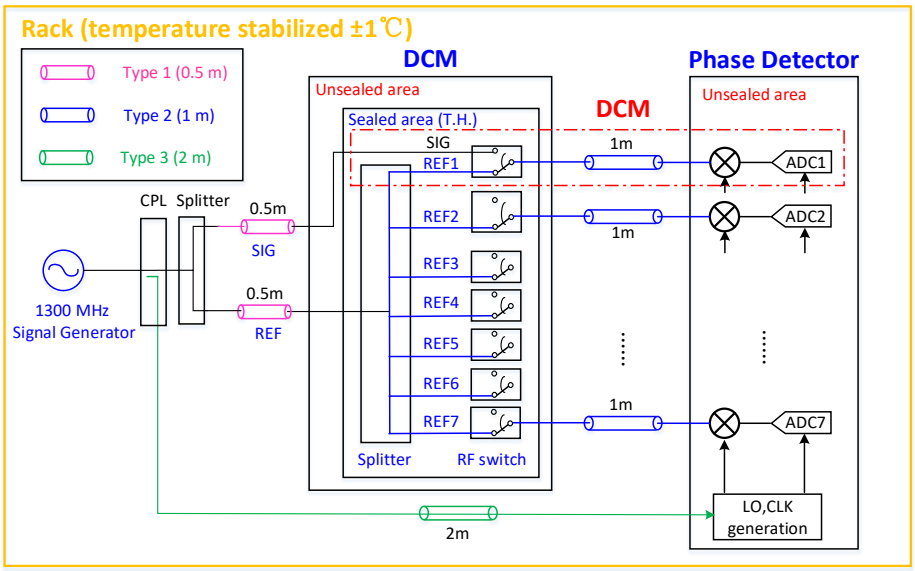

Figure 5.17: Setup of phase drift compensation using DCM and RTC at DESY test stand.

The measurement result of the RTC between the seven channels and the DCM is presented in Fig. 5.18. The system phase drift (REF1) is observed to be 1.94° at 1300 MHz with open rack. This drift can be suppressed to 50 millidegrees (pk-pk) level using the DCM or RTC method. As shown in Fig. 5.19, the system phase drift can be compensated within 47.8 millidegrees (pk-pk) with DCM and controlled between 27.9 millidegrees (pk-pk) to 46.7 millidegrees (pk-pk) with RTC. The performance is comparable. However, the residual phase drift with DCM can be affected by the external unsealed splitter. The stability is expected to be improved by sealing the splitter. The residual phase drift using the RTC method has a different direction than that with DCM. In the setup, the seven-channel splitter and RF switch are well sealed with stable temperature (0.005 °C) and humidity (1%RH). Thus, the possible source of the residual phase is the uncorrelated noise, RF cables, and some unbalanced PCB routing in the digital board.

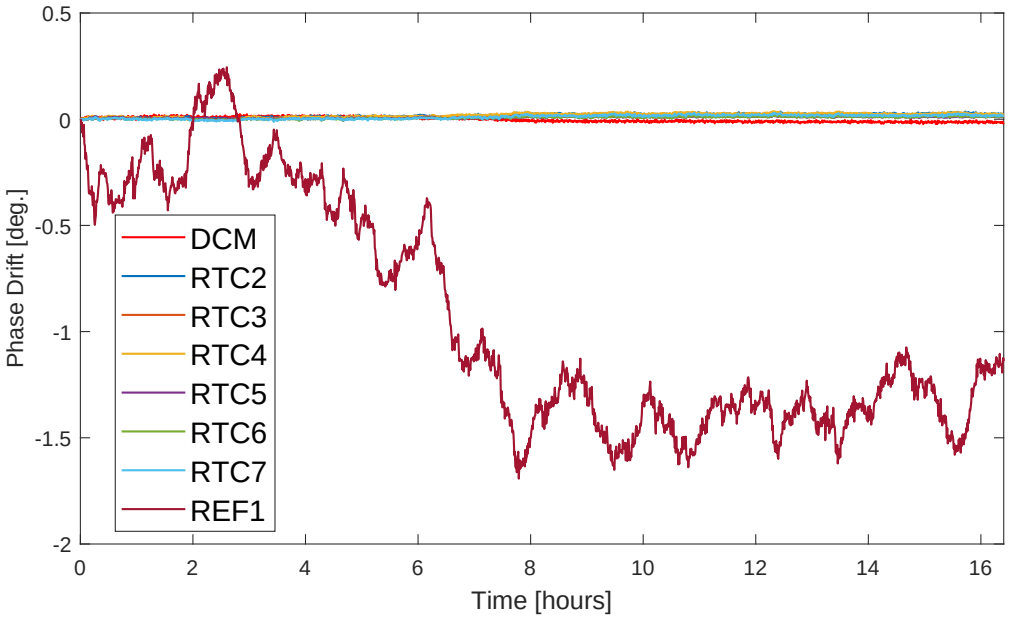

Figure 5.18: Long-term phase drift compensation of the monitoring system using DCM and RTC.

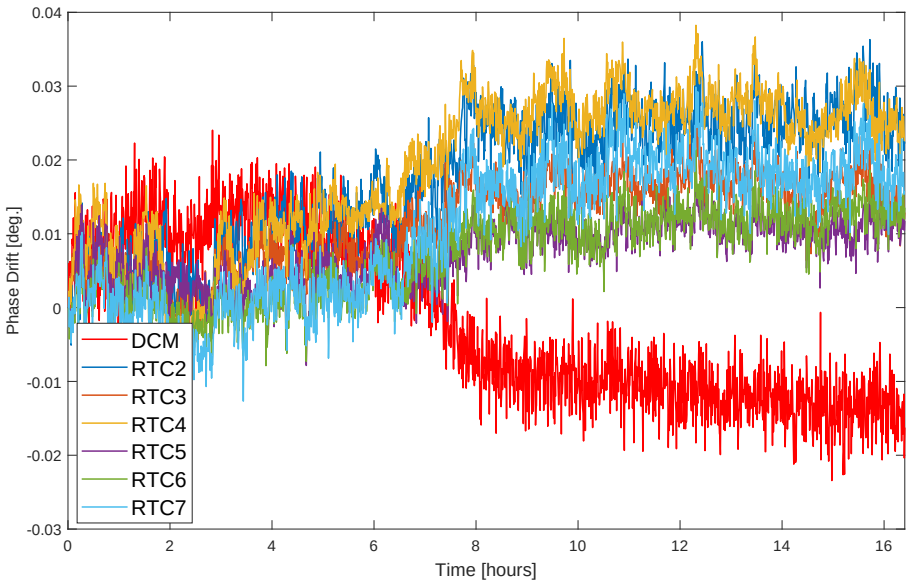

Figure 5.19: Comparison of long-term performance using DCM and RTC (zoomed data of Fig. 5.18).

Chapter 6

Demonstration of RF Reference Phase Stabilization System for Injector LINAC

Several techniques have been developed to stabilize the reference phase with femtosecond precision. A phase stabilization system should be specific to the current system at the injector LINAC, with low cost using commercial components that are simple to implement. A reference phase stabilization system using optic circulator and WDM technique are considered.

6.1 Phase Stabilization System with WDM Technique

The WDM technique multiplexes several optical signals into a single optical fiber with different light wavelengths (λ). It can be subdivided into coarse WDM (CWDM) and dense WDM (DWDM). The CWDM technique is characterized by the nominal central wavelength range from 1271 nm to 1611 nm and wider central wavelength spacing of not less than 20 nm, as defined in the ITU standard [64]. In contrast, the DWDM technique is characterized by narrower central wavelength spacing (1.6 nm, 0.8 nm, 0.4 nm, or 0.1 nm), as defined in the ITU standard [65].

In the early stage, the CWDM technique with two nominal wavelengths of 1310 nm and 1550 nm are used in the phase stabilization system. The wavelength of 1310 nm is applied for the transmission from the transmitter to the remote receiver (λ_1) and the wavelength of 1550 nm is used to send the slow phase drift back through the same PSOF from the receiver to the transmitter (λ_2). Here, λ_1 and λ_2 denote the wavelength for forward path

and the backward wavelength, respectively. As described in Section 4.1.2, the group delay depends on the wavelength. Therefore, the transmitted phase was found to depend on the wavelength difference ($\Delta\lambda$ =240 nm) using this feedback system [66]. Thus, the DWDM technique with wavelengths of 1550.12 nm and 1551.72 nm is considered ($\Delta\lambda$ =1.6 nm).

To compensate the phase drift in the long optical link, the mechanical VODL and PDFS are widely used for optical length control. VODL is driven by a stepping motor with low resolution but large optical delay, with a range of up to hundreds of millimeters. PDFS is driven by a piezoelectric ceramic (PZT) with high resolution but small optical delay, whose range is limited to several millimeters. Thus, it is recommended to apply VODL for coarse control and PDFS for fine control in the phase stabilization system. In our case, the measurement result with PDFS compensation are presented in this chapter.

6.1.1 Schematic Design

Figure 6.1 shows the schematic diagram of the DWDM technique with PDFS compensation. The 2856 MHz reference signal generated by the SG is split into four using a four-port power splitter: (1) the reference signal from port 1 (REF) is directly measured to indicate the monitoring system phase drift, (2) the reference signal from port 2 is used for LO and clock generation, (3) the reference signal from port 3 is sent to one E/O module (at 1551.72 nm) for reference distribution and feedback control, and (4) the reference signal from port 4 (REF4) is directly measured by another ADC to confirm the phase drift from the monitoring system.

For this system, the electrical signal is converted to the optical signal with one wavelength (λ1) by an E/O. Then, the optical signal is transmitted through 120 m PSOF, which is located inside the temperature and humidity controlled chamber to ensure that the temperature and humidity can be changed independently. To guarantee the free extension of the PSOF, the fiber should be unbound in all measurements.

Finally, the optical signal is converted to the 2856 MHz electric signal by an O/E. This setup is the same as that in the LINAC gallery. Thus, the TRS phase drifts owing to the effects on temperature and humidity on the PSOF. Physically, the REF and TRS signals are several hundred meters away (e.g., 380 m from the MO to sector 5). To monitor the long-term TRS phase drift, the electrical signal is sent back through the same PSOF using another pair of E/O and O/E modules with another wavelength (λ2). The E/O and O/E modules with special wavelength are customized by TAMAGAWA Electronics Inc. [44]. Two WDMs are applied to combine and split the two

optical signals in the forward and backward paths. The phase drift of the returned signal (RTN) is expected to be twice that of the TRS signal. This phase drift is compensated by the piezo-driven fiber stretcher by adjusting the optical path length. An integral (I) controller is applied for precise feedback control. The TRS phase is monitored to evaluate the system performance. To reduce the system phase drift, all rf/optic components are situated inside the temperature stabilized chamber with a stability of $\pm 0.1\,^{\circ}\mathrm{C}$.

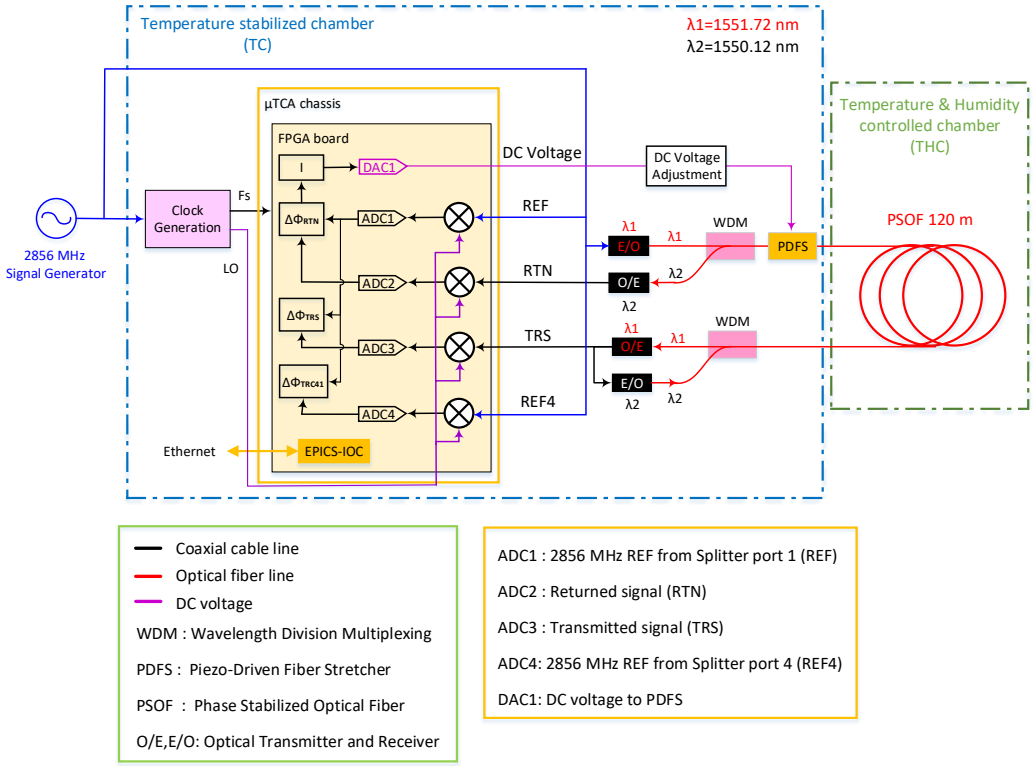

Figure 6.1: Schematic diagram of the DWDM technique with PDFS compensation.

The phase of the REF, RTN, TRS, and REF4 signals are monitored by ADC1, ADC2, ADC3, and ADC4, respectively. After rejecting the system phase drift, the phase drift of each signal can be represented as

$$\Delta\phi_{RTN} = \phi_{RTN} - \phi_{REF} \tag{6.1}$$
$$\Delta\phi_{TRS} = \phi_{TRS} - \phi_{REF} \tag{6.2}$$
$$\Delta\phi_{RTC41} = \phi_{REF4} - \phi_{REF} \tag{6.3}$$
$$\Delta\phi_{TRS} = 1/2 \cdot \Delta\phi_{RTN}$$

where ϕ_{REF} is the system phase drift, ϕ_{RTN} is the phase drift of the RTN signal, ϕ_{TRS} is the phase drift of the TRS signal, and ϕ_{RTC41} is the phase drift between ADC1 and ADC4, which indicates the phase stability of the monitoring system by applying the reference tracking method described in Section 5.3.3.

In our case, two close optical wavelengths of 1550.12 nm and 1551.72 nm with a smaller optical wavelength difference ($\Delta\lambda = 1.6\,\text{nm}$) are adopted for the forward and backward paths ($\lambda 1 = 1550.12\,\text{nm}, \lambda 2 = 1551.72\,\text{nm}$).

6.1.2 Piezo-driven Fiber Stretcher

The PDFS (FST-001-B) with large delay range, high speed, low insertion loss and analog/digital control was provided by General Photonics Inc. [69]. Its optical delay range is up to 3 mm. The piezoelectric ceramics are packaged in a metal enclosure including the piezo driver, as shown in Fig. 6.2. The device is controlled by four independent PZTs such that there is an option to drive each PZT individually for high resolution or collectively for large stroke. In addition, each PZT can be controlled either with an analog signal (e.g., DC voltage) or a 12- bit transistor-transistor logic (TTL) signal. Under analog control, the piezo driver acts as a 4-channel (CH) voltage amplifier with 30 V/V amplification. During digital control, the output voltage can be controlled using a computer equipped with a digital I/O card or a microprocessor.

Figure 6.2: Photo of PDFS (FST-001-B).

The main parameters are listed in Table 6.1. The phase change sensitivity is 810π/V at 1550 nm in the case of analog input with four channels. Thus, the time delay sensitivity can be calculated as

$$\Delta t_{dsen} = \frac{\Delta P_{dsen}}{2\pi \cdot f_{opt}} = \frac{\Delta P_{dsen}}{2\pi} \cdot \frac{\lambda}{\nu} = \frac{810\pi/V}{2\pi} \cdot \frac{1550\,\text{nm}}{3 \times 10^8} = 2.09\,\text{ps}/V \quad (6.4)$$

where Δt_{dsen} is the time delay sensitivity, ΔP_{dsen} is the phase change sensitivity, f_{opt} and λ are the frequency and wavelength of the optical signal, respectively, and ν is the speed of light ($\nu = 3 \times 10^8$ m/s). The phase sensitivity is 2.15°/V at 2856 MHz. In our case, the PDFS is driven by a 16-bit DAC via analog control and four PZTs are collected for the large stroke. The resolution of DAC output voltage can achieve $\frac{1}{2^{15}}$ V. Thus, the resolution of the PDFS time delay is 0.064 fs, which corresponds to 0.066 millidegrees at 2856 MHz.

Table 6.1: Specifications of the PDFS (FST-001-B).

Parameter	**Performance**
Optical delay range	> 3 mm
Phase change sensitivity	810π/V at 1550 nm (4 CHs)
Max. voltage on PZT	140 V
Internal voltage amplification	30 V/V
Analog input	4 CHs (max. 4.7 V for each CH)
Digital input	20-pin digital connector, 12-bit TTL
Operation Temperature	0 to 50 °C
Resonance frequency	2.2±0.3 kHz
Wavelength range	1260 to 1620 nm
Fiber type	SMF-28 standard
Insertion loss	<0.2 dB
Insertion loss variation	<0.1 dB
Return loss	>65 dB
Polarization dependent loss (PDL)	<0.05 dB

To confirm the phase range and sensitivity of the PDFS at 2856 MHz, the input voltage of PDFS is changed from 0 V to 4.7 V and the TRS phase change is measured by ADC3. Figure 6.3 shows the relationship between the RF phase change and the input voltage of PDFS. The phase change is up to 10.5° at 2856 MHz with the maximum input voltage of 4.7 V, which covered the phase drift of optical link in the gallery (max. 6°). The measured sensitivity is 2.36°/V, including the measurement error and the hysteresis effect of the PZT. This measurement result is consistent with the specification (2.15°/V).

6.1.3 Timing Jitter

To confirm the short-term performance of the optical link, the integral timing jitter is measured by the signal source analyzer (E5052B, Agilent Technologies). Figure 6.4 shows the SSB phase-noise power spectrum of the MO,

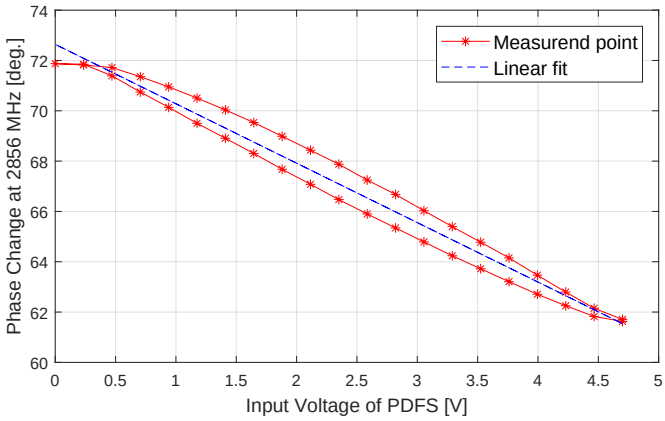

Figure 6.3: Phase change at 2856 MHz as a function of the input voltage of PDFS.

TRS, and RTN signals from 10 Hz to 10 MHz. The measurement result is summarized in Table 6.2. All jitters are found to be less than 100 fs (rms) and the phase noise is less than 0.1° (rms) from 10 Hz to 10 MHz.

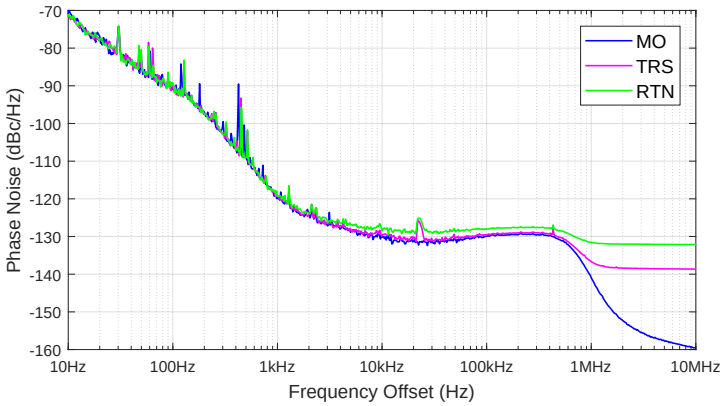

Figure 6.4: DWDM scheme: SSB phase-noise power spectrum of the MO, TRS, and RTN signals.

6.1.4 Short-term Stability

As shown in Fig. 6.5, short-term stability (10 ms) of each signal without digital LPF is measured. The phase range is the same for all signals. The result is summarized in Table 6.3. The phase stability of the reference signal is 0.02° (rms). Owing to the insertion of the E/O, O/E modules and the long

Table 6.2: DWDM scheme: Timing jitter of MO, TRS, and RTN signals at 2856 MHz.

Signal	Power [dBm]	Jitter [fs]	Phase Noise [deg.]
MO	-1.27	72.71	0.075
TRS	-6.60	77.38	0.080
RTN	-8.82	95.35	0.098

PSOF, the phase stability of the SOPT and TRS signal is gradually increased to 0.046° (rms) and 0.05° (rms), respectively. However, the phase stability of the RTN signal is as large as 0.108° (rms); thus, a digital IIR LPF with bandwidth of 10 Hz is applied to reduce the ADC noise. The phase stability of all the signals is improved to less than 0.004° (rms). Then, the short term data of 10 ms are averaged for the long-term measurement.

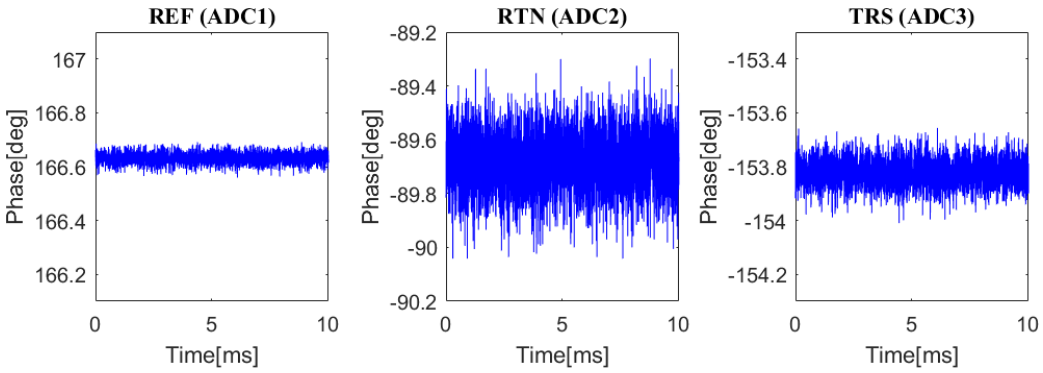

Figure 6.5: Short-term (10 ms) phase stability without digital LPF.

Table 6.3: Short-term (10 ms) phase stability without digital LPF.

Channel	ADC1	ADC2	ADC3
Signal	**REF**	**RTN**	**TRS**
Stability (rms)	0.020°	0.108°	0.05°

6.1.5 Long-term Performance Evaluation

Long-term Phase Stability with Temperature Change

To estimate the phase drift of the transmitted signal, the temperature inside THC is changed from 20 °C to 40 °C and down to 20 °C at a stable relative

humidity of 40%RH as before. A step of 5 °C per 2 h is used. Without the phase stabilization system, the phase drift of the transmitted signal due to the temperature change is shown in Fig. 6.6. By changing the temperature to 20 °C, the phase drifts of the TRS and RTN signals were 5.33° (pk-pk) and 10.73° (pk-pk), respectively. The feedback loop was not adopted and the DAC output was kept at 0 V.

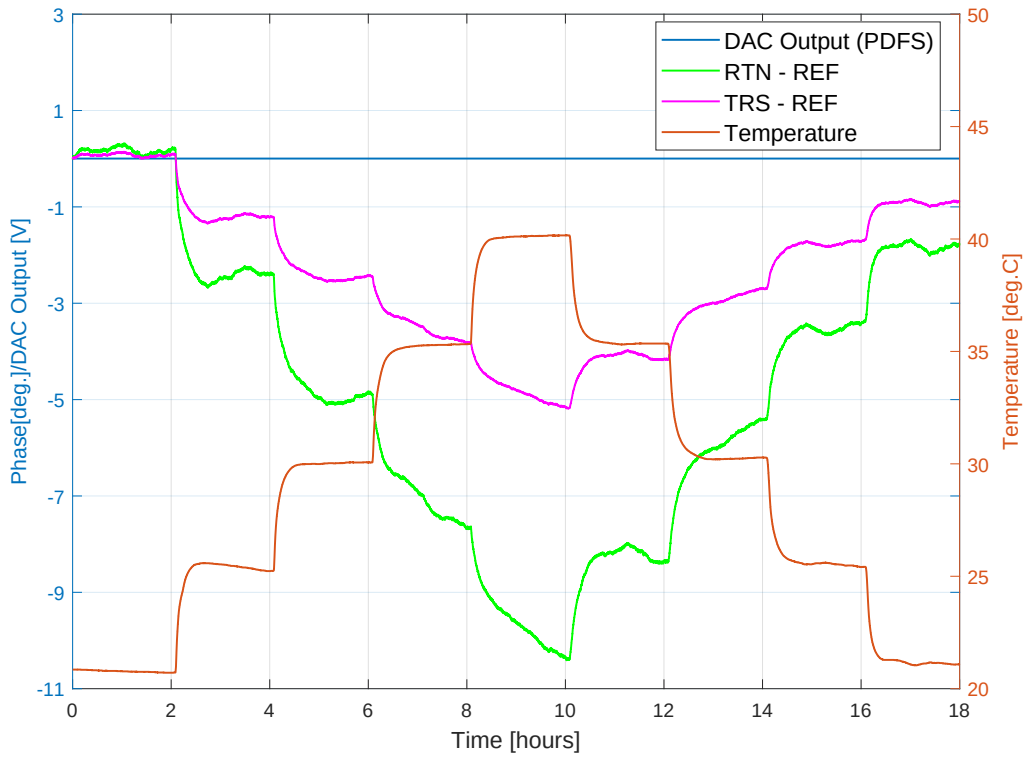

Figure 6.6: Temperature change: long-term phase drift of the RTN and TRS signals without compensation using 1550.12 nm and 1551.72 nm.

To evaluate the system performance, the phase stabilization system is applied. The MO and transmitted signals are directly measured by the ADCs, as shown in Fig. 6.7. The system phase drift is estimated to be 0.4375° and 0.4489° from ADC1 and ADC4, respectively. The phase difference between ADC1 and ADC4 is as small as 0.0114° corresponding to 11 fs at 2856 MHz. Thus, the system phase drift can be suppressed by subtracting the phase drift in the REF or REF4. The system phase drift is caused by the environmental change (humidity/temperature fluctuations) effect on the RF components (e.g., power splitter, LO generation), RF cables, and PCB routing

of the FPGA board; however, all components are located in the temperature stabilized chamber. The temperature (SYSINTEMP) and humidity (SYSINHUMID) inside the TC, where the feedback system is located, are monitored by the sensors. As shown in Fig. 6.8, the temperature stability is controlled within 0.17 °C (pk-pk) and the relative humidity is not controlled with the fluctuation of 2.52%RH (pk-pk). It is found that the REF phase drift depends on the temperature and humidity inside TC. The correlation coefficient between the REF phase and SYSINTEMP is 0.89 and that between the REF phase and SYSINHUMID is -0.66. Thus, the REF phase has high correlation with SYSINTEMP and strong correlation with SYSINHUMID. All phase drifts directly detected by ADC include the system phase drift. To reject the system phase drift effect on the performance evaluation, the REF phase drift is subtracted from the TRS and RTS phases in the following data analysis. Each phase is calculated at 2856 MHz.

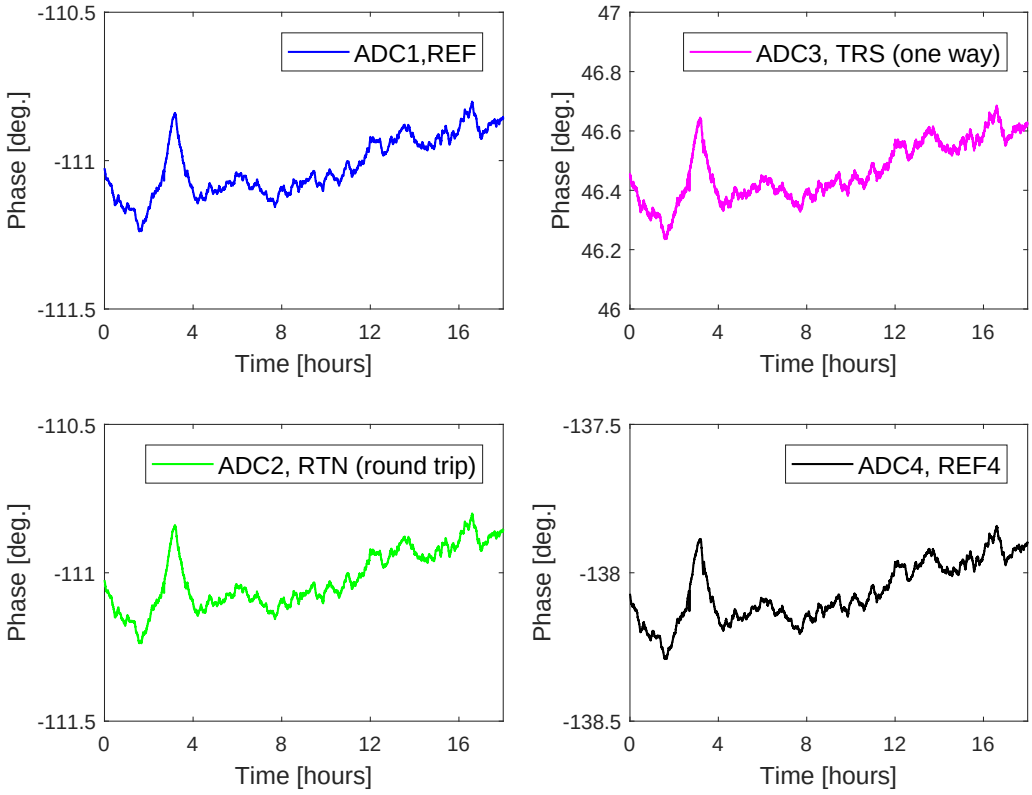

Figure 6.7: DWDM scheme with feedback under temperature change: phase drift measured by ADC directly.

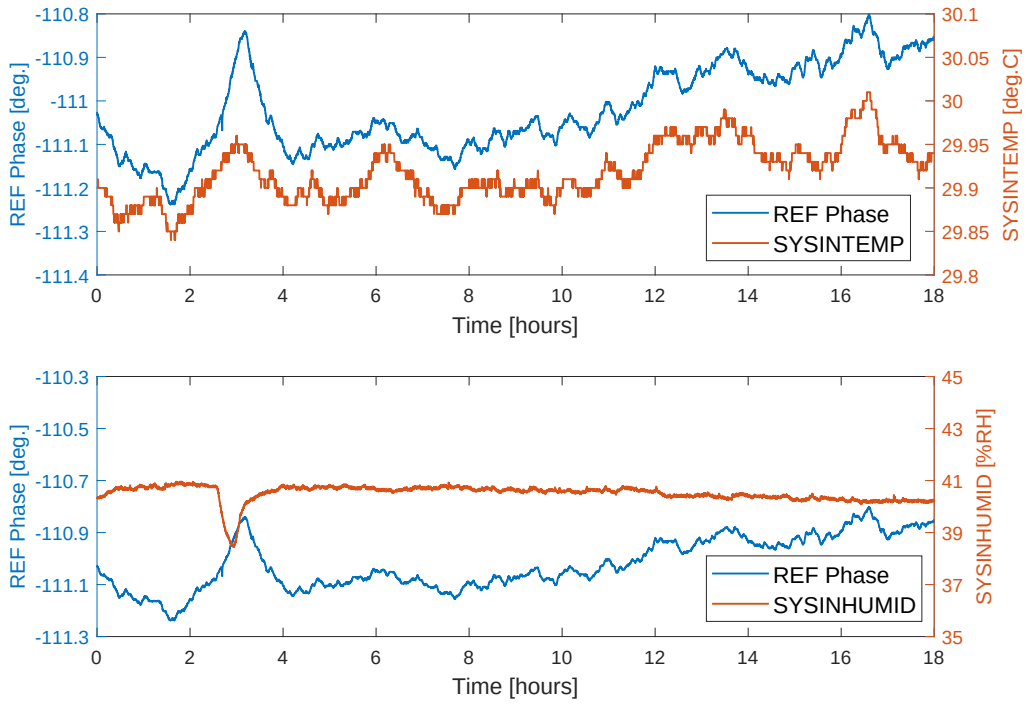

Figure 6.8: DWDM scheme with feedback under temperature change: REF phase and temperature/humidity fluctuation inside the TC (feedback system located).

Figure 6.9 describes the temperature change near PSOF and the long-term phase stability with the PDFS compensation. It is evident that the DAC output voltage is correlated to temperature change such that the TRS phase drift is compensated by adjusting the optical path length. As shown in Fig. 6.10(a), the RTN phase is suppressed from 10.73° (pk-pk) to 0.68 millidegrees (0.66 fs) (rms); however, the TRS phase is suppressed from 5.33° (pk-pk) to 59 millidegrees (57 fs) (pk-pk). This TRS phase stability includes a large spike in noise between 2 to 4 h as represented in Fig. 6.10(b). To find the source of this spike, the phase difference between ADC4 and ADC1 is calculated as shown in Fig. 6.11. It is evident that the noise spike in the phase difference between the two channels matched with that of the phase difference between TRS and REF. Thus, this spike in noise is caused by the measurement error instead of the feedback system. Therefore, we can conclude that the TRS phase is stabilized within 35 fs (pk-pk), which fulfilled the requirement.

As discussed in [66], the TRS phase stability is seriously effected by the wavelength difference (240 nm) between the forward and backward paths. In

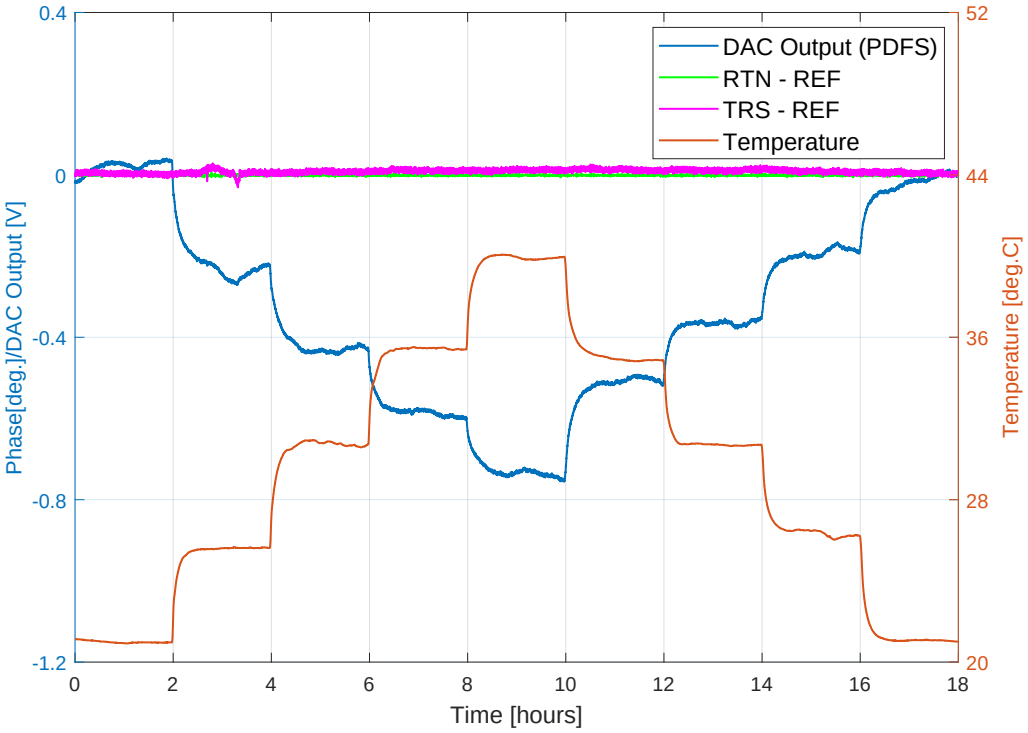

Figure 6.9: Temperature change near PSOF and long-term phase drift of the RTN and TRS signals with PDFS compensation using 1550.12 nm and 1551.72 nm.

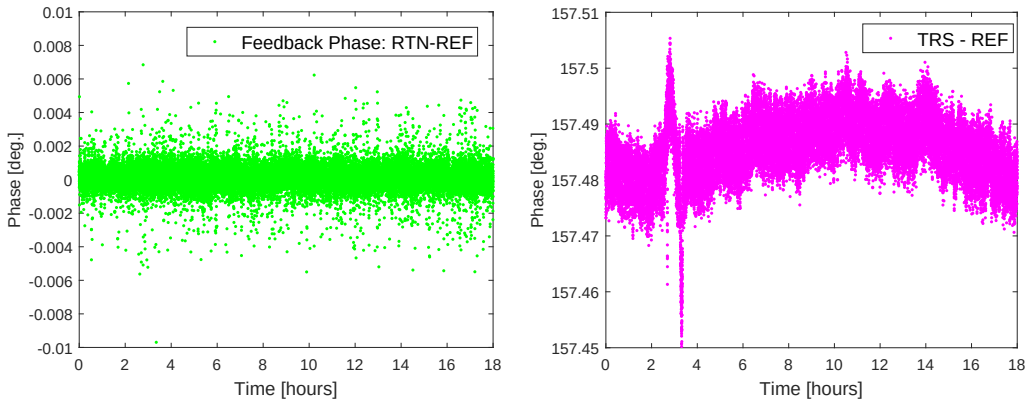

(a) RTN phase stability for 18 h.

(b) TRS phase stability for 18 h.

Figure 6.10: DWDM scheme with feedback under temperature change: RTN and TRS phase stability for 18 h with feedback.

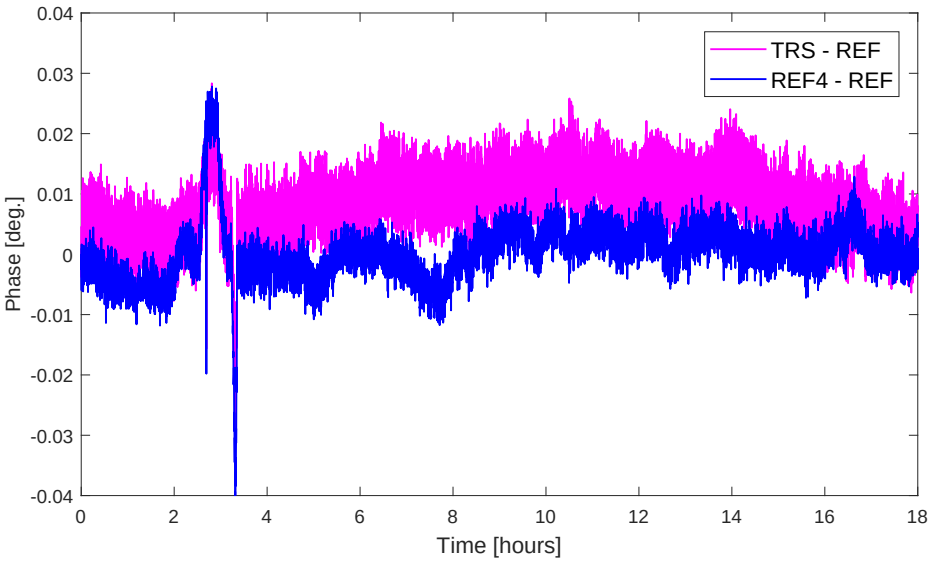

Figure 6.11: DWDM scheme with feedback under temperature change: phase difference between TRS and REF vs. phase difference between REF4 and REF, the spike in the noise is caused by the measurement error.

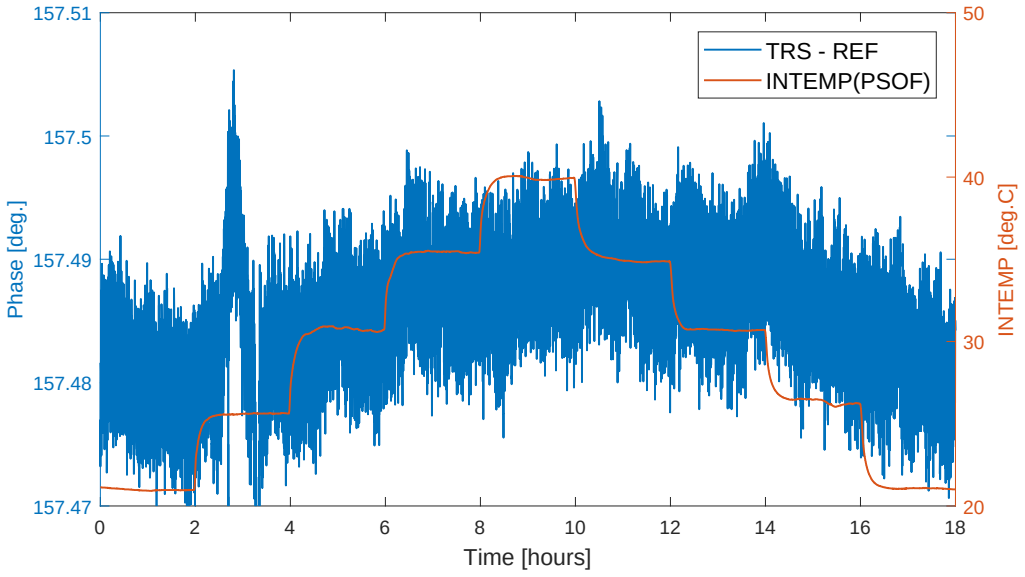

Figure 6.12: DWDM scheme with feedback under temperature change: correlation between TRS phase and temperature change near PSOF (INTEMP(PSOF)).

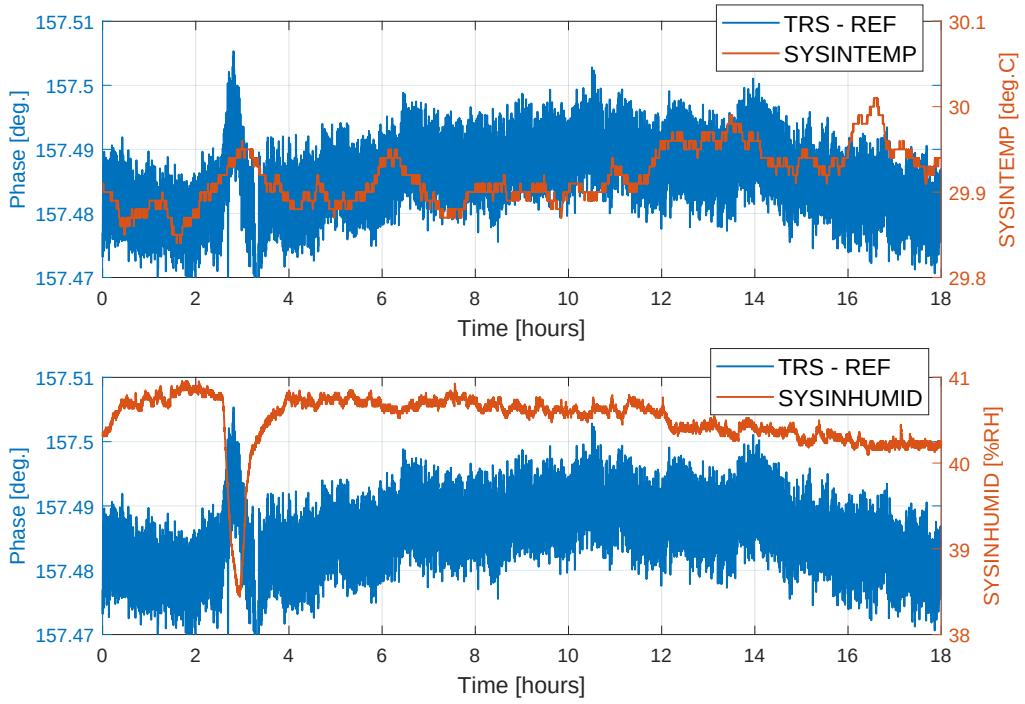

Figure 6.13: Temperature and humidity inside the TC where the RF components and optical devices are located.

the current setup, wavelengths of 1550.12 nm and 1551.72 nm are adopted and the difference between the forward and backward paths is found to be as small as 1.6 nm. As shown in Fig. 6.12, the TRS phase still depends on the temperature changes near PSOF inside the THC (INTEMP(PSOF)). The correlation coefficient is 0.5, which ensure a moderate correlation. Furthermore, the temperature in the LINAC gallery is controlled within ±1 °C, which is much smaller than the measurement setup in the laboratory (20 °C). In conclusion, the wavelength difference effect is successfully suppressed by adopting two wavelengths with a smaller difference to the forward and backward paths. Even though it is not completely eliminated, it is small enough to fulfill the requirement for the injector LINAC.

As mentioned above, all components are located inside the temperature stabilized chamber. However, there is no control for the humidity. A small phase drift still remains in the RF components (e.g., power splitter, amplifier, LO generation) and optical devices (e.g., O/E and E/O modules, WDMs, PDFS) owing to the humidity effect. It is also included in the TRS phase drift. The TRS phase drift and the temperature and humidity fluctuations

inside the TC are shown in Fig. 6.13. The temperature is stabilized within 0.17 °C and the correlation between the TRS phase and temperature is weak with a coefficient of 0.14. The humidity fluctuation is 2.51%RH and the correlation between the TRS phase and humidity is also weak with a coefficient of -0.11.

Long-term Phase Stability with Humidity Change

The phase drift of the PSOF is affected by the changes in temperature and humidity. The relative humidity inside the THC is changed from 30%RH to 60%RH at a stable temperature of 30 °C, as shown in Fig.6.15. Owing to the control range of the THC, the humidity range for this test (30%RH to 60%RH) only covers part of the humidity change (20%RH to 50%RH) at the LINAC gallery during one year. However, the humidity fluctuation (ΔH = 30%RH) is the same; therefore, a comparable phase drift can be induced. In comparison to the temperature effect, it takes longer to let the moisture go inside the PSOF; hence, the step is set to 10%RH per 10 h.

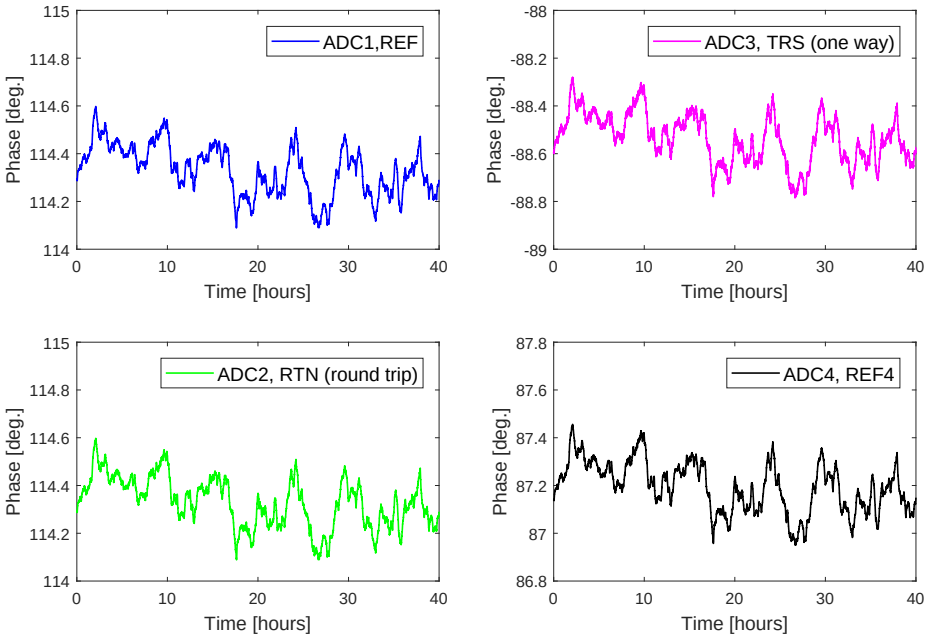

Figure 6.14: DWDM scheme with feedback under humidity change: phase drift measured by ADC directly.

As shown in Fig. 6.14, the reference, RTN and TRS signals are directly measured by four ADCs as before. The reference signals from the same

MO but different ports of the power splitter are measured by ADC1 (REF) and ADC4 (REF4). The system phase drifts in REF and REF4 are 0.5086° and 0.5049°, respectively. The phase difference between them is as small as 0.0037° at 2856 MHz corresponding to 3.6 fs. Thus, the system phase drift can be suppressed by subtracting the phase drift of REF or REF4. The TRS and RTN phases also followed the reference phase well. As mentioned before, the system phase drift is rejected from the phase drift of TRS and RTN in the data analysis.

Figure 6.15 shows the humidity change and temperature stability near PSOF and the long-term phase stability of the RTN and TRS signals with the PDFS compensation. The relative humidity and temperature are monitored by a sensor. The relative humidity is changed from 30%RH to 60%RH. However, because the temperature at humidity 30%RH and 40%RH is not well controlled, the fluctuation is 1.77 °C. Thus, the phase drift is caused by humidity as well as temperature. However, it will not effect the performance of the phase stabilization system. Each phase drift is compensated by the PDFS. As shown in Fig. 6.15, with feedback, the DAC outputs the DC voltage to PDFS to adjust the optical path length so that the RTN and TRS phase drift can be well compensated. However, there is no obvious proportional relationship between the humidity and DAC output. Because the moisture goes inside the PSOF gradually and the humidity takes more time to affect the time delay of PSOF. As shown in Fig. 6.16, the RTN phase is controlled within 0.64 millidegrees (0.62 fs) (rms) and the TRS phase is stabilized to 57.5 millidegrees (56 fs) (pk-pk), which fulfilled the requirement.

To study the wavelength difference effect caused by the temperature and humidity, the TRS phase and the humidity/temperature changes near PSOF are compared in Fig. 6.17. The correlation coefficient between the TRS phase and temperature is -0.57 and that between the TRS phase and humidity is +0.54. Thus, the TRS phase has moderate correlation with both temperature and humidity. This result is consistent with that obtained in Section 6.1.5.

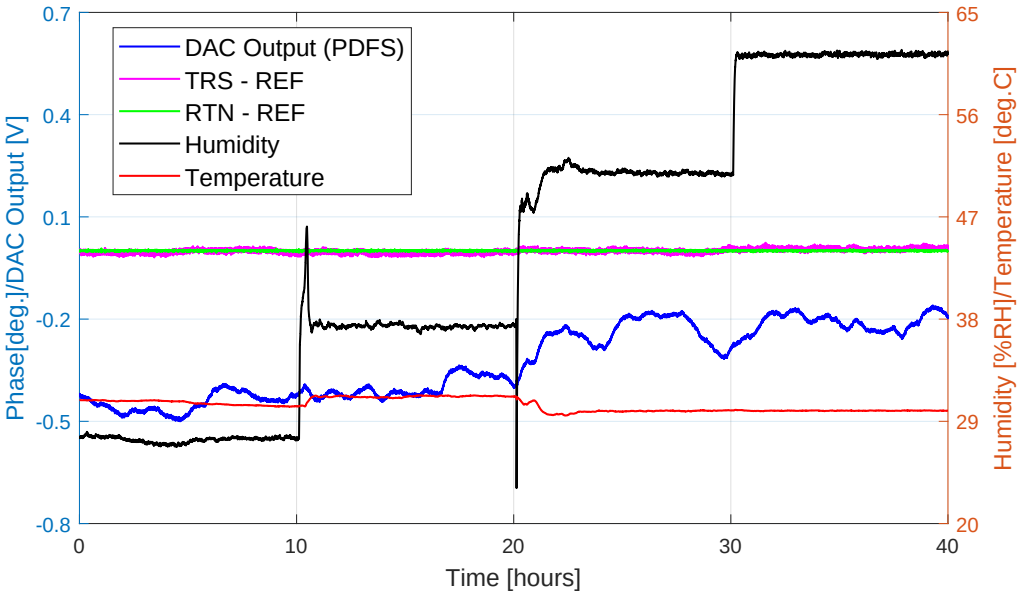

Figure 6.15: Humidity change: relative humidity change and temperature stability near PSOF and the long-term phase drift of the RTN and TRS signals with PDFS compensation using 1550.12 nm and 1551.72 nm.

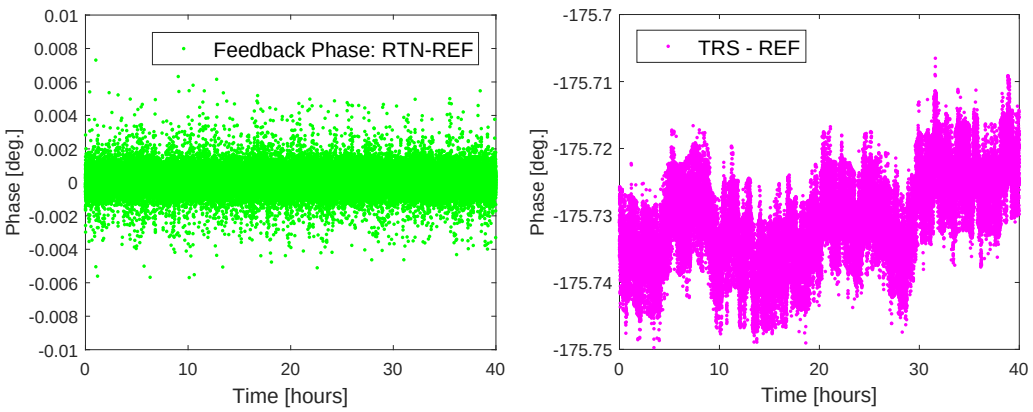

(a) RTN phase stability for 40 h.

(b) TRS phase stability for 40 h.

Figure 6.16: DWDM scheme under humidity change: RTN and TRS phase stability for 40 h with feedback.

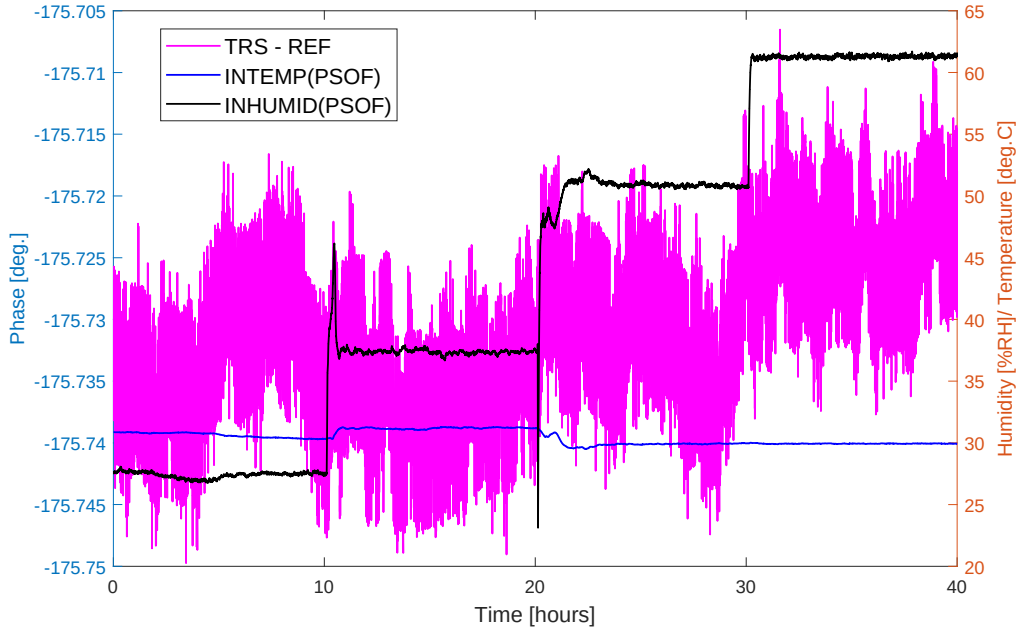

Figure 6.17: DWDM scheme with feedback under humidity change: correlation between the TRS phase and relative humidity.

Long-term Phase Stability with Free Temperature and Humidity Fluctuations

The phase stabilization system is located in the test hall where the temperature is controlled within ±1 °C by air conditioner, but the humidity is not controlled. The temperature and humidity control situation is the same as in LINAC gallery. To let the PSOF experience the temperature and humidity environment closest to the real situation in the LINAC gallery, the PSOF is exposed in the test hall, instead of inside the THC.

From Fig. 6.18, it is evident that the system phase drift is 0.68° (ADC1). The system phase drift can be rejected from the TRS phase by subtracting the REF or REF4 phase. Figure 6.19 shows the temperature and humidity changes in the test hall and the long-term TRS phase stability with PDFS compensation. The temperature and humidity fluctuations in the test hall are 2.55 °C and 7.71%RH, respectively. With feedback, the DAC output voltage to PDFS is 0.22 V, implying that 1.2° at 2856 MHz is compensated according to the amplifier of 2.5 times and the phase sensitivity of 2.15°/V. As shown in Fig. 6.20, the feedback phase is stabilized within 0.61 millidegree (rms) 2856 MHz corresponding to 0.59 fs. The long-term TRS phase is controlled

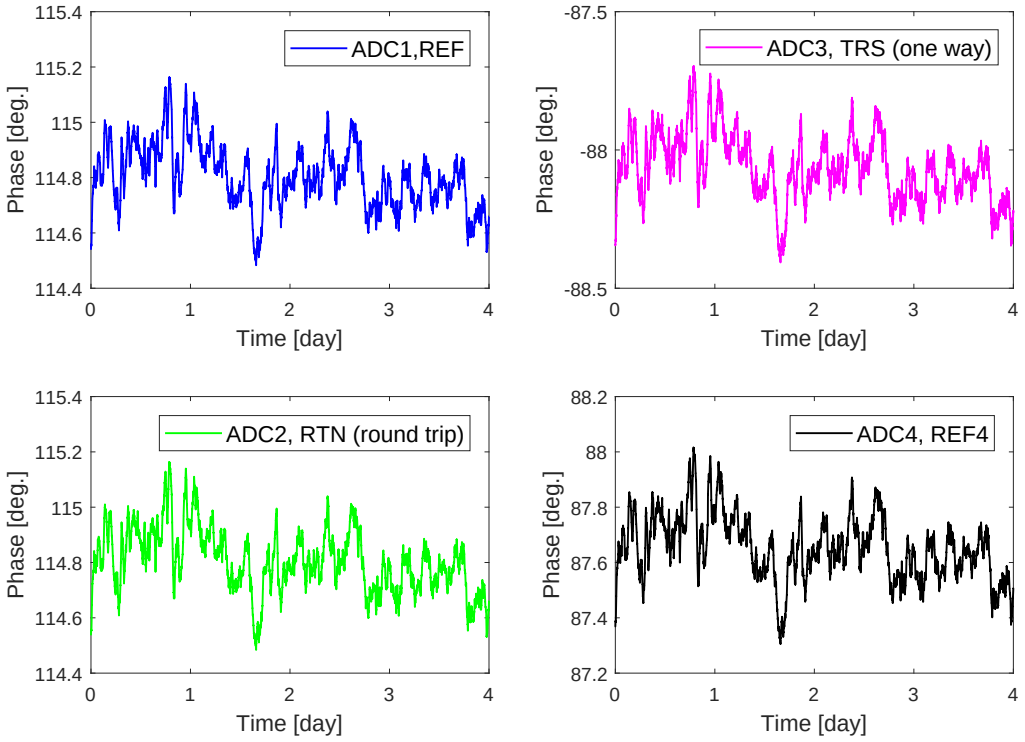

Figure 6.18: DWDM scheme with feedback under free temperature and humidity change: phase drift directly measured by ADCs.

within 0.0452° (pk-pk) corresponding to 44 fs, which fulfilled the requirement 0.1° (rms).

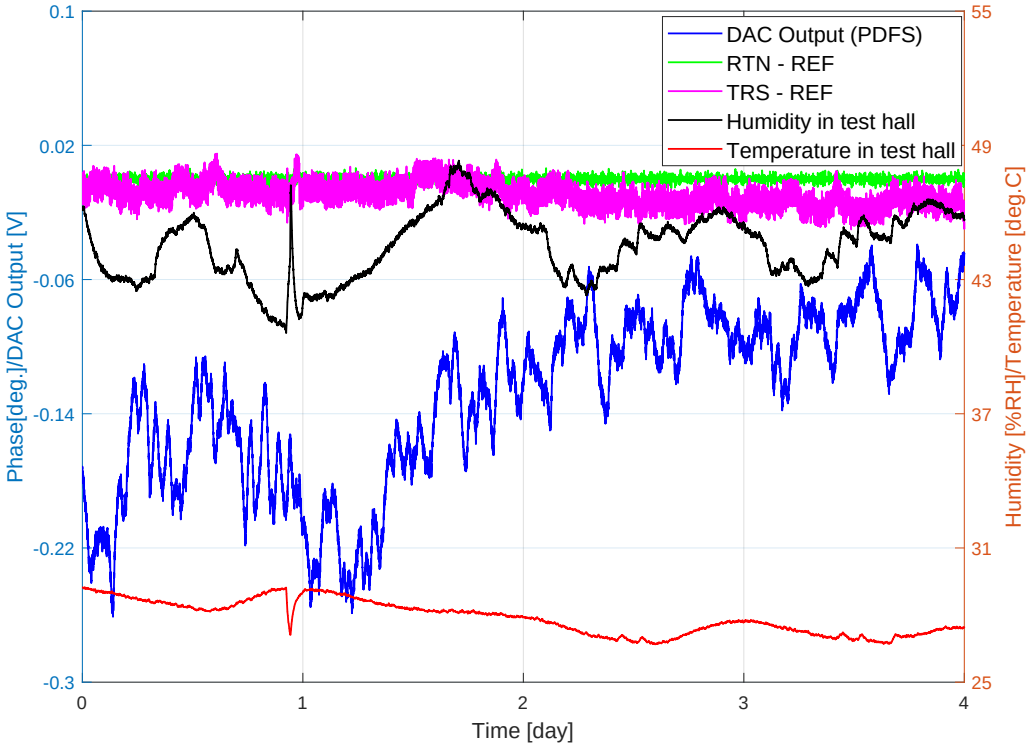

Figure 6.19: DWDM scheme: temperature and humidity changes in the test hall and long-term TRS phase stability with PDFS compensation for four days.

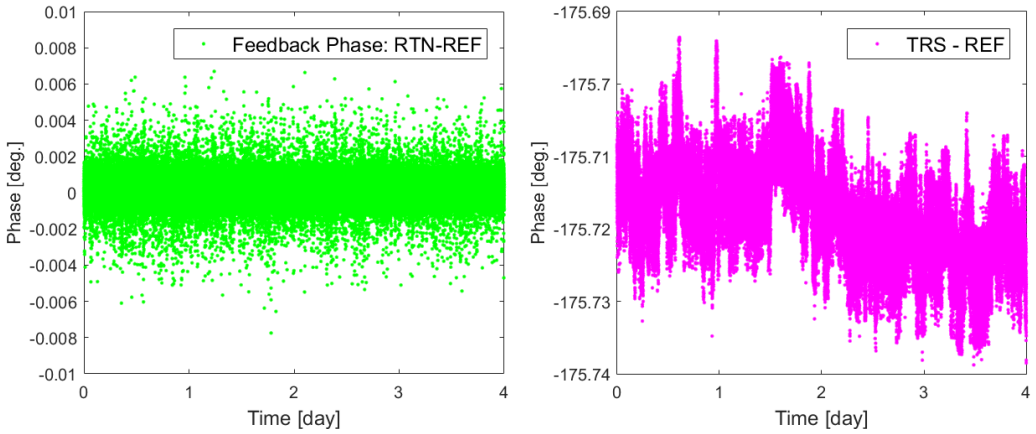

(a) RTN phase stability for four days.

(b) TRS phase stability for four days.

Figure 6.20: DWDM scheme: RTN and TRS phase stability for four days with feedback.

Summary for WDM Technique

So far, we evaluated the performance of the phase stabilization system by changing the temperature (TEMP) and humidity (HUMID) near PSOF. The performance is summarized in Table 6.4. The long-term jitter duration is between 15 and 20 fs (pk-pk). Each TRS phase is stabilized within 56 fs (pk-pk) corresponding to 0.6 millidegrees at 2856 MHz, which fulfilled the reference phase requirement. This scheme can be one of the candidates for reference phase stabilization at the SuperKEKB injector LINAC.

Table 6.4: Summary of the long-term performance with DWDM technique.

	TEMP Change	**HUMID Change**	**TEMP/HUMID Change**
Time [h]	18	40	96
TEMP [°C]	20-40	30	25-30
HUMID [%RH]	40	30-60	40-50
ΔT [°C]	20	–	2.55
ΔH [%RH]	–	30	7.71
RTN [fs] (rms)	0.66	0.62	0.59
TRS [fs] (pk-pk)	35	56	44

6.2 Phase Stabilization System with Optic Circulator

Optic circulators can be used to send optical signals through a single fiber in two directions. Two single mode optic circulators (SMOC) are applied to send the phase drift back for the phase stabilization system. The WDM technique is already used in the SuperKEKB ring; however, this is the first time that the phase stabilization system is being implemented using optic circulator.

6.2.1 Schematic Design

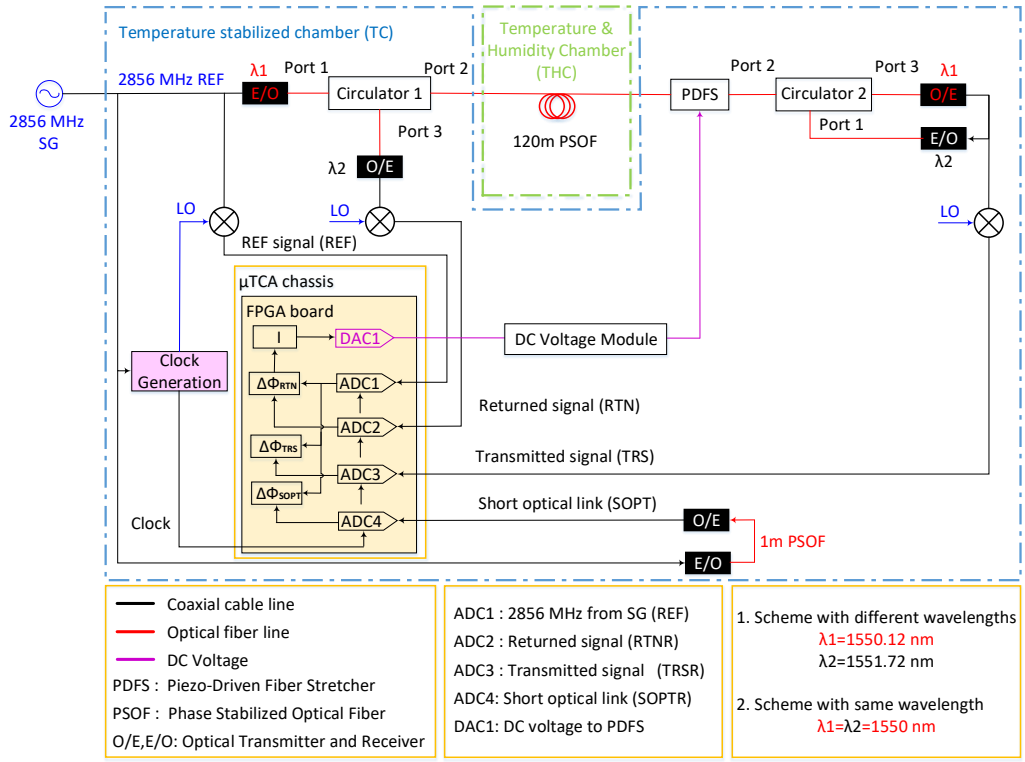

Figure 6.21: Schematic diagram of the phase stabilization system with SMOC.

A prototype of the reference phase stabilization system with SMOC is proposed. A SMOC is located at both ends of the fiber. Each SMOC adds a signal in one direction while removing the signal from the other. The schematic diagram is shown in Fig. 6.21. The 2856 MHz reference signal is

generated by a SG. The electric signal is converted to optical signal with the wavelength λ_1 using an E/O module. The optical signal is given as input to port 1 of one SMOC (SMOC1) and received as output from port 2. It is transmitted via 120 m PSOF, which is situated inside the temperature and humidity controlled chamber; thus, the environment changes near the PSOF can be simulated. Then it is given as input to port 2 of the other SMOC (SMOC2) and received as output from port 3. The optical signal is converted to the electric signal by an O/E module with the wavelength λ_1. To send the phase drift information back to the transmitted side, the received electrical signal is split into two: one is monitored to evaluate the system performance and the other is again converted to the optical signal with the wavelength λ_2 by another E/O. It is given as input to port 1 of SMOC2 and received as output from port 2. This optical signal is transmitted through the same PSOF and received by SMOC1 from port 2 to port 3. Finally, the optical signal is converted to electrical signal with the wavelength λ_2 by another O/E. The phase drift in the long optical link is detected by the phase detector. The same PDFS is used to adjust the optical length for phase drift compensation. The phase drift in the short optical link is also measured to evaluate the phase drift in one pair of E/O and O/E modules. The REF, RTN, TRS, and SOPT signals are directly measured by ADC1 to ADC4. Similar to Section 6.1, wavelengths of 1550.12 nm and 1551.72 nm are adopted for the forward and backward paths ($\lambda 1 = 1550.12\,\text{nm}, \lambda 2 = 1551.72\,\text{nm}$).

6.2.2 Single Mode Optic Circulator

The SMOC is a one-directional, three-port, non-reciprocating device. An optical circulator is analogous to an electronic circulator and both perform similar functions.

- One directional, three-port

  It allows the light to travel in only one direction. It means a signal entering port 1 will exit port 2 with minimal loss and a signal entering port 2 will exit port 3 with minimal loss. The light that enters port 2 experiences a large amount of loss at port 1 and the light entering port 3 experiences a large amount of loss at ports 2 and 1.

- Non-reciprocating

  This means that any changes in the properties of light caused by passing through the device are not reversed by traveling in the opposite direction.

Owing to its high isolation and low insertion loss, optical circulators are widely used in advanced communication systems and DWDM systems. A SMOC with a center wavelength of 1550 nm and a fiber-optic connector (FC)/ angled physical contact (APC) fiber connector is provided by Thorlabs Inc. [70] and the specification is listed in Table 6.5.

Table 6.5: Specification of the single mode optic circulator.

Specification	**Value**
Wavelength Range	1525-1610 nm
Insertion Loss	0.8 dB Typ./1.0 dB Max.
Isolation	>40 dB
Directivity (port 1 to port 3)	>50 dB
PDL	≤40 dB
Return Loss	≥ 50 dB
Max. Optical Power	500 mW
Operating Temperature	0 to 70 °C
Operating Relative Humidity	5% to 60%
Fiber	SMF-28
Connector (each port)	FC/APC

6.2.3 Timing Jitter

The integral timing jitter is measured by the signal source analyzer (E5052B, Agilent Technologies). Figure 6.22 shows the SSB phase-noise power spectrum of the MO, E/O, and O/E modules as well as the TRS and RTN signals from 10 Hz to 10 MHz. The measurement result is summarized in Table 6.6. All jitters are found to be less than 103 fs (rms) and the phase noise is less than 0.105° (rms) from 10 Hz to 10 MHz. The performance is comparable with the phase stabilization system using the WDM technique.

Table 6.6: SMOC scheme: Timing jitter and phase noise at 2856 MHz.

Signal	**Power [dBm]**	**Jitter [fs]**	**Phase Noise [deg.]**
MO	-1.27	72.71	0.075
E/O+O/E	3.16	75.80	0.078
TRS	-8.09	77.17	0.079
RTN	-10.7	102.05	0.105

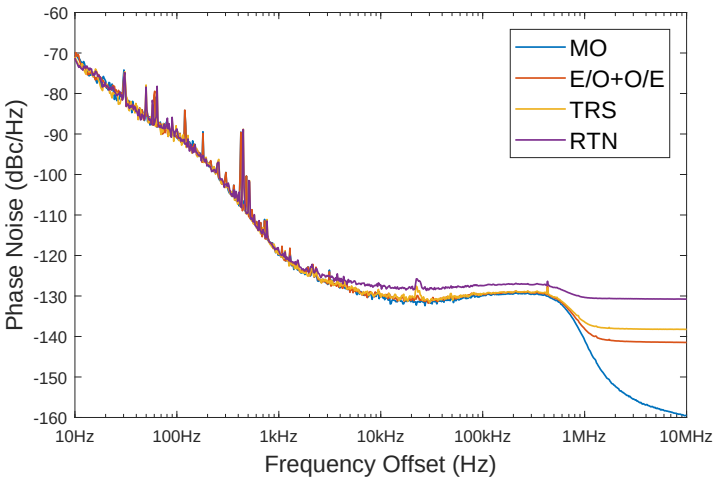

Figure 6.22: SMOC scheme: SSB phase-noise power spectrum of MO signal, E/O and O/E modules, TRS signal, and RTN signal.

6.2.4 Short-term Stability

As shown in Fig. 6.23(a), the short-term phase stability of 100 ms without digital LPF is measured by four ADCs. The result in time domain is summarized in Table 6.7. The phase stability of REF is 0.018° (rms). After one pair of E/O and O/E modules, the phase stability is increased to 0.027° (rms) (SOPT signal). After inserting two SMOCs and one PDFS, the phase stability is again increased to 0.046° (rms) in a single path (TRS signal) and 0.071° (rms) in a round-way path (RTN signal). From the frequency domain, as shown in Fig. 6.23(b), the phase stability is increased from REF, SOPT, TRS, and RTN signals. The result is consistent with that obtained in the time domain. Moreover, there is no spurious in fast Fourier transform (FFT) result. The short-term raw data is averaged and used for the long-term phase drift measurement. Usually, the phase drift in the optical link is very slow in the order of several minutes or hours. To improve the accuracy of the long-term phase drift, a digital IIR LPF with a narrow bandwidth of 10 Hz is applied to reduce the ADC noise.

Table 6.7: SMOC scheme: short-term phase stability without digital LPF.

Channel	**ADC1**	**ADC2**	**ADC3**	**ADC4**
Signal	**REF**	**RTN**	**TRS**	**SOPT**
Stability (rms)	0.018°	0.071°	0.046°	0.027°

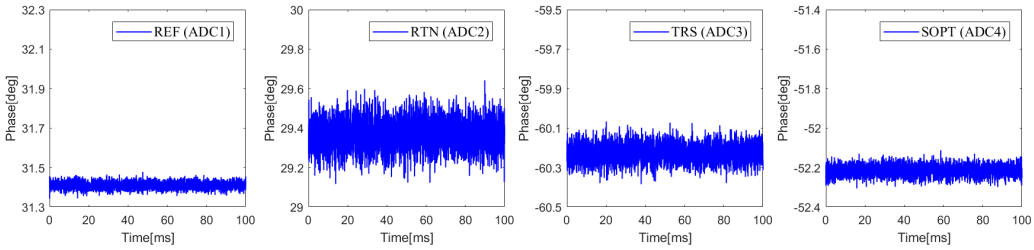

(a) Short-term raw data in time domian.

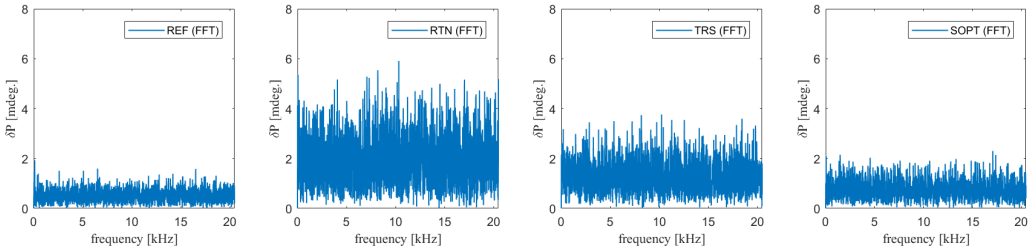

(b) Short-term raw data in frequency domain.

Figure 6.23: SMOC scheme: short-term phase stability without digital LPF.

6.2.5 Long-term Performance Evaluation

Long-term Stability with Temperature Change

As shown in Fig. 6.21, a PSOF of 120 m is located inside the THC. To evaluate the system performance with temperature change, the temperature inside the THC is changed from 20 °C to 40 °C and down to 20 °C at a stable relative humidity of 40%RH as before. The step used here is of 5 °C per 2 h. The phase drifts in the TRS and RTN signals without phase drift compensation are described in Fig. 6.24. Due to the 20 °C temperature change, the phase drift in the TRS and RTN signals was 4.93° (pk-pk) and 9.76° (pk-pk), respectively. Without feedback, the DAC output was kept at 0 V.

With the same temperature change procedure, the phase stabilization system is applied. As shown in Fig. 6.25, the REF, RTN, TRS, and SOPT signals are directly measured by the ADCs. The system phase drift is estimated to be as small as 0.21° at 2856 MHz from ADC1 for 18 h. To reject the system phase drift effect on the performance evaluation, the REF phase drift is subtracted from the TRS and RTS phases.

Figure 6.26 describes the phase drift compensation result under the temperature change. The temperature near PSOF is changed from 20 °C to 40 °C and down to 20 °C. The TRS and RTN phase drifts according to the temperature. With the PDFS compensation (DAC output voltage), the RTN phase drift is compensated from 9.76° (pk-pk) to 0.69 millidegrees (rms) at

2856 MHz, which corresponds to 0.67 fs. The TRS phase is suppressed from 4.93° (pk-pk) to 57 millidegrees (pk-pk) at 2856 MHz corresponding to 56 fs, which fulfilled the requirement. This phase stability (56 fs) includes the slow phase drift as well as the short-term jitter of about 10 fs (pk-pk). The zoomed data are illustrated in Fig. 6.27. Even though the phase stability of the TRS signal already fulfilled the requirement, the small phase drift still remains, as shown in Fig. 6.27(b).

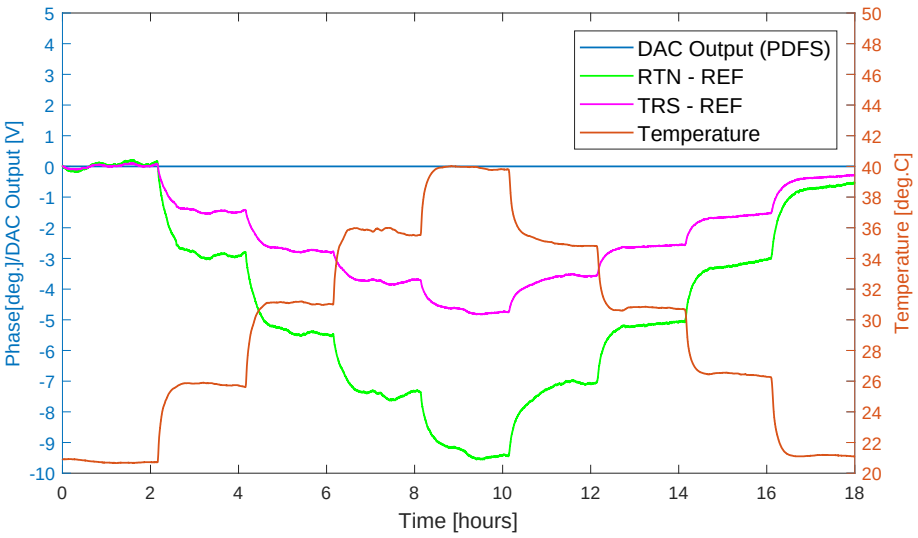

Figure 6.24: SMOC scheme: long-term phase drift of the RTN and TRS signals with 20 °C temperature change without compensation.

Figure 6.28 indicates that the residual TRS phase drift depends on the temperature near PSOF. The correlation coefficient between the residual TRS phase drift and the temperature near PSOF is 0.91, which implies that they have high correlation. Thus, this residual TRS phase drift is caused by the wavelength difference ($\Delta\lambda = 1.6$ nm) between the forward path ($\lambda_1 = 1550.12$ nm) and backward path ($\lambda_2 = 1551.72$ nm).

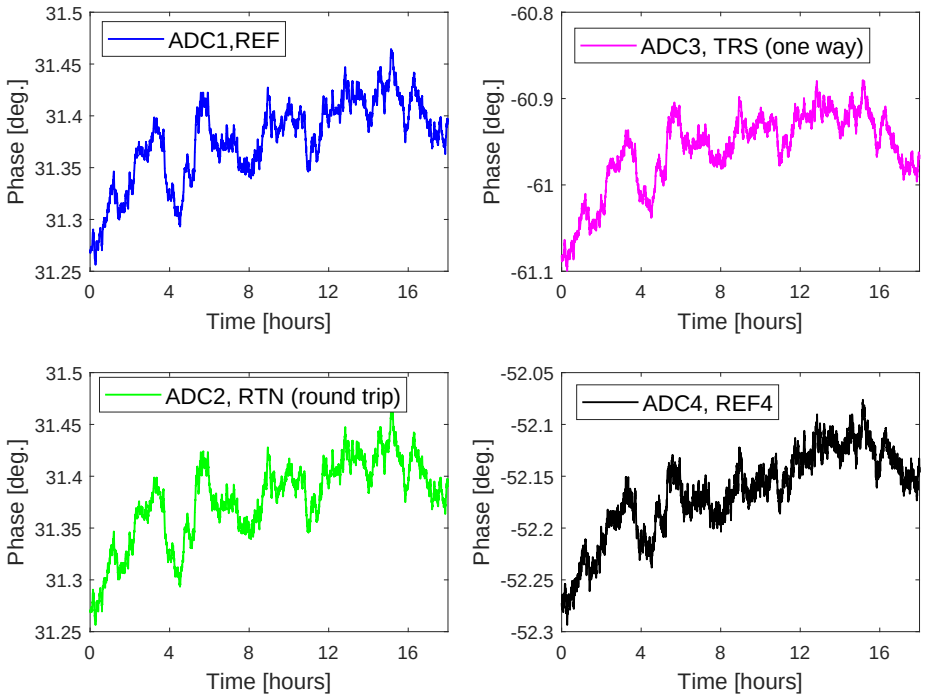

Figure 6.25: SMOC scheme under temperature change: phase drift measured by ADC directly with SMOC scheme.

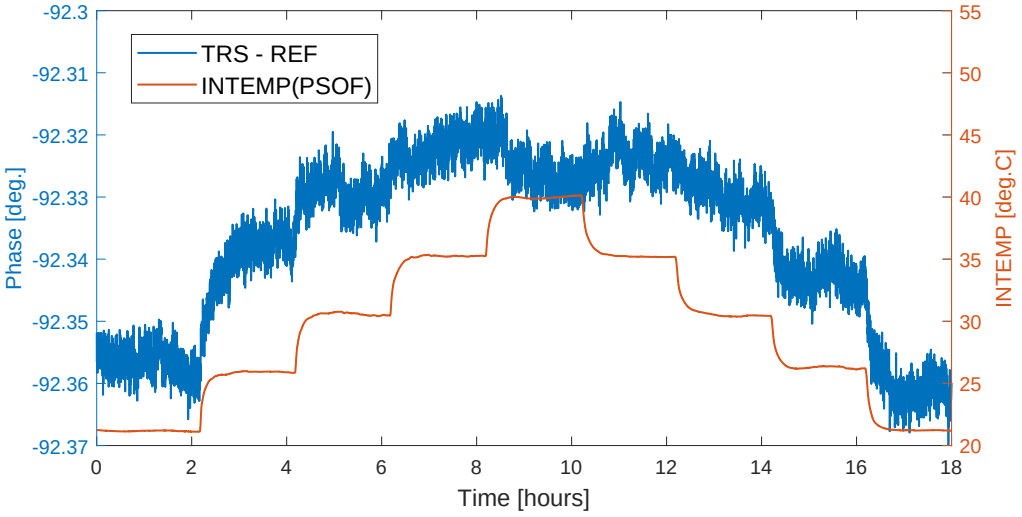

Figure 6.28: SMOC scheme under temperature change: correlation between the TRS phase and the temperature change near PSOF (INTEMP(PSOF)).

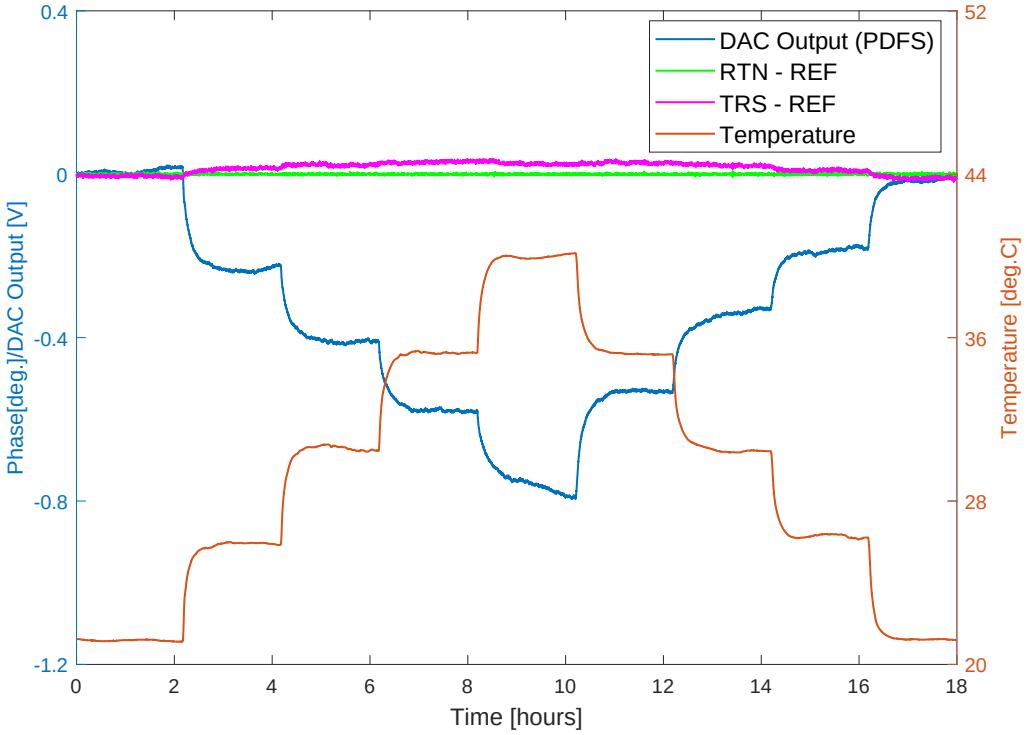

Figure 6.26: SMOC scheme under temperature change: Temperature change near PSOF and the long-term phase drift of the RTN and TRS signals with PDFS compensation.

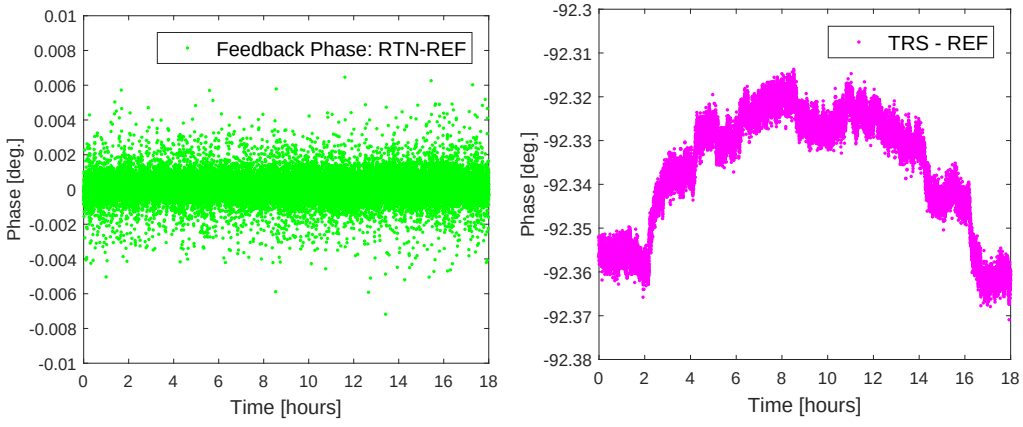

(a) RTN phase stability for 18 h.

(b) TRS phase stability for 18 h.

Figure 6.27: SMOC scheme under temperature change: RTN and TRS phase stability for 18 h with feedback.

In this case, different wavelengths are used for the forward path ($\lambda 1$) and backward path ($\lambda 2$). The optical length is exactly the same for both paths. According to Eq. (4.1), the transmission time delay is influenced by the wavelength. Owing to the wavelength difference between the two paths, the phase change in the forward path ($\Delta\phi_{for}$) is different from that in the backward path ($\Delta\phi_{back}$). The phase difference ($\Delta\phi_{diff}$) and the wavelength difference ($\Delta\lambda$) between them is

$$\Delta\phi_{diff} = \Delta\phi_{for} - \Delta\phi_{back} \tag{6.5}$$

$$\Delta\lambda = \lambda 1 - \lambda 2 \tag{6.6}$$

The TRS and RTN phase drift can be represented as

$$\Delta\phi_{TRS} = \Delta\phi_{for} \tag{6.7}$$

$$\begin{aligned}\Delta\phi_{RTN} &= \Delta\phi_{for} + \Delta\phi_{back} \\ &= 2\Delta\phi_{for} - \Delta\phi_{diff}\end{aligned} \tag{6.8}$$

With feedback control, we have $\Delta\phi_{RTN} = 0$; thus, the TRS phase drift can be derived as

$$\Delta\phi_{TRS} = \frac{1}{2}\Delta\phi_{diff} \tag{6.9}$$

In conclusion, the residual TRS phase drift is determined by the phase difference between the forward and backward paths. According to Eq.(4.1), the group delay has a negative correlation with the wavelength. In our setup, $\Delta\lambda$ is less than 0; therefore, $\Delta\phi_{diff}$ is more than 0. Thus, the residual TRS phase drift is more than 0, which is consistent with the measurement result shown in Fig. 6.28.

To confirm the wavelength effect on TRS phase stability, wavelengths of 1548.57 nm and 1551.69 nm are applied to the forward and backward paths in the reference phase stabilization system. The setups are presented in Table 6.8. Figure 6.29 describes the transmitted phase stability with compensation under the same temperature change. Compared to setup 1 (purple line) and setup 2 (red line), the transmitted phase stability has positive correlation with the wavelength difference between the two paths. Compared to setup 2 (red line) and setup 3 (blue line), the same wavelength difference was applied, and almost the same TRS phase stability was achieved. However, the forward wavelength and backward wavelengths were switched and the direction of the residual TRS phase drift was also changed. The small phase fluctuation at setup 3 is caused by the measurement error of the phase monitor system, not the real fluctuation of the TRS phase. Thus, smaller wavelength difference is recommended to improve the transmitted phase stability.

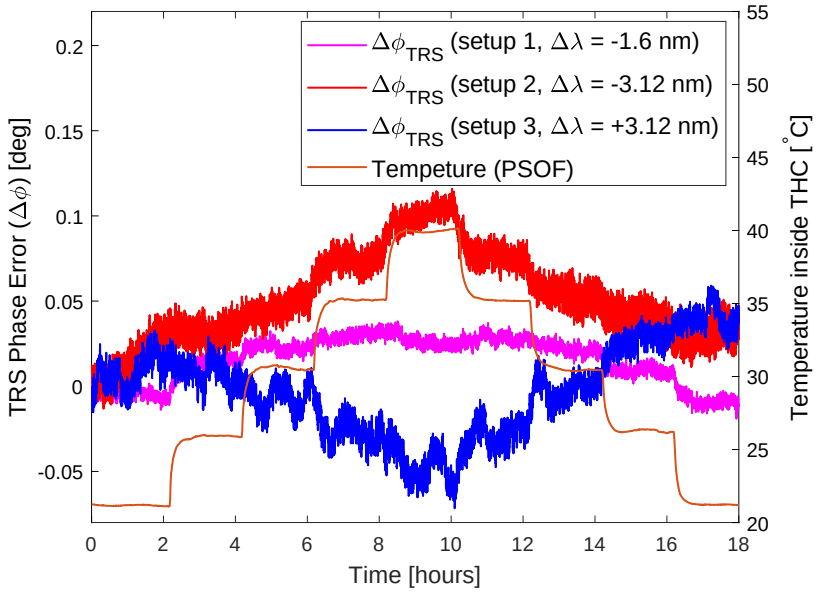

Figure 6.29: Transmitted phase stability using different wavelengths for the forward and backward paths with feedback control.

Table 6.8: Transmitted phase stability using different wavelengths.

Symbol	**Unit**	**Setup 1**	**Setup 2**	**Setup 3**
$\lambda 1$	nm	1550.12	1548.57	1551.69
$\lambda 2$	nm	1551.72	1551.69	1548.57
$\Delta\lambda$	nm	-1.6	-3.12	+3.12
$\Delta\phi_{TRS}$	fs	+56	+126	-127

Long-term Stability with Humidity Change

The same humidity change is considered as in Section 6.1.5. The relative humidity inside the THC is changed from 30%RH to 60%RH at a stable temperature of 30 °C with the step of 10%RH per 10 h. The same feedback parameters as in Section 6.1.5 are applied. The REF, TRS, RTN, and SOPT signals are measured by four ADCs, as shown in Fig. 6.30. The system phase drift is 0.36° (pk-pk). With phase drift compensation, the TRS and RTN phase followed the REF phases very well.

Figure 6.31 shows the relative humidity change, temperature stability, and the long-term phase drift of RTN and TRS signals with PDFS compensation. The relative humidity was changed from 30%RH to 60%RH (ΔH=30%RH) with small fluctuation at 40%RH. The temperature at humidity from 40%RH

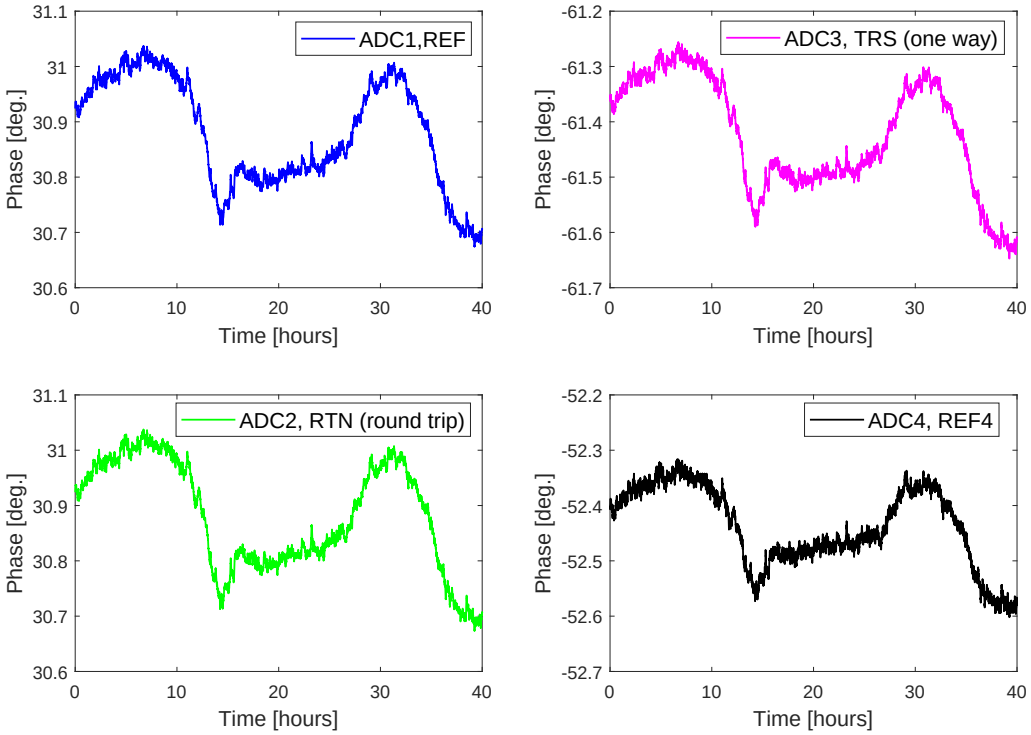

Figure 6.30: SMOC scheme under humidity change: phase drift measured by ADC directly.

to 50%RH is not well-controlled and its stability is 1.7 °C, which is consistent with Section 6.1.5. With phase drift compensation, as shown in Fig. 6.32, the RTN phase is controlled within 0.65 millidegrees (0.63 fs) (rms) and the TRS phase is stabilized to 43.7 millidegrees (42.5 fs) (pk-pk), which fulfilled the requirement.

The possible source of the residual TRS phase drift is the temperature and humidity fluctuation effect on the feedback system (e.g. SMOCs, PDFS, power splitter, amplifier, attenuator) and the long PSOF. In Fig. 6.32(b), there is a large phase jump (30 fs) between 10 h and 20 h. It is found that it is caused by the temperature and humidity fluctuations inside the TC (in red circle) where the feedback system is located, as shown in Fig. 6.33. Moreover, the long-term slow drift in the negative direction was found to depend on the humidity and the small temperature fluctuation near the PSOF, as presented in Fig. 6.34. The correlation coefficients of the TRS phase and humidity, and the TRS phase and temperature are as high as -0.87 and +0.8, respectively, which is due to the wavelength dispersion.

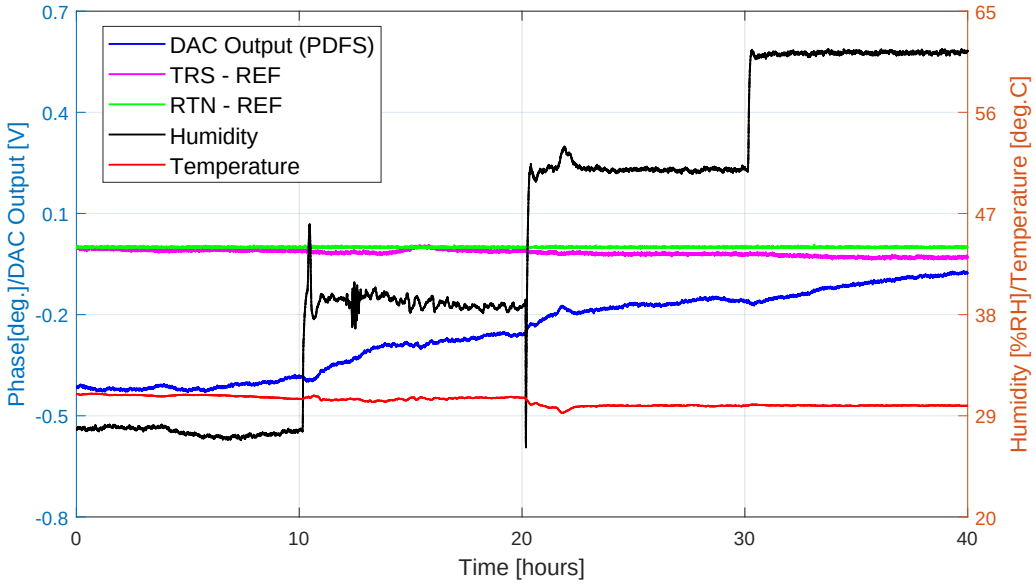

Figure 6.31: SMOC scheme under humidity change: relative humidity change and temperature stability near PSOF and the long-term phase drift of the RTN and TRS signals with PDFS compensation using 1550.12 nm and 1551.72 nm.

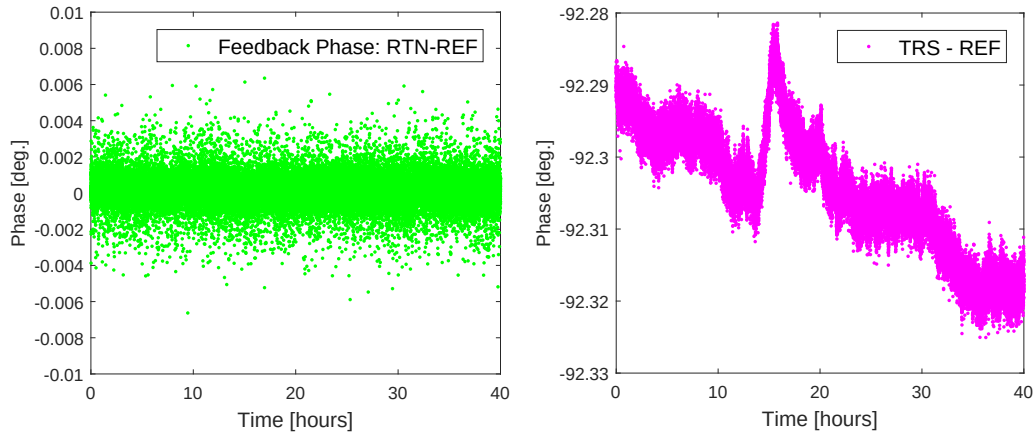

(a) RTN phase stability for 40 h.

(b) TRS phase stability for 40 h.

Figure 6.32: SMOC scheme under humidity change: RTN and TRS phase stability for 40 h with feedback.

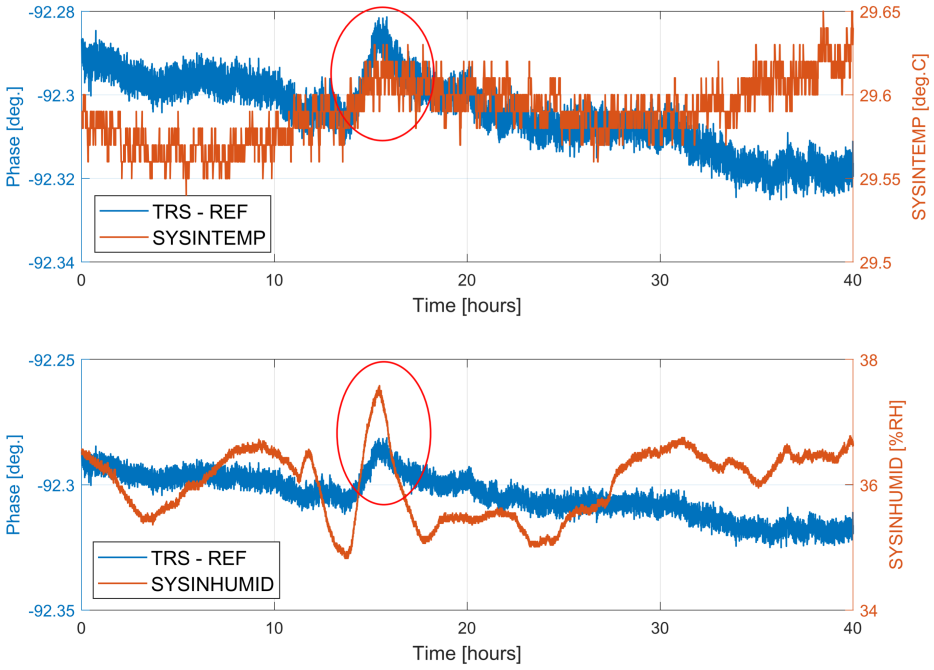

Figure 6.33: SMOC scheme under humidity change: correlation between TRS phase and relative humidity and TRS phase and temperature change inside TC where the phase stabilization system is located.

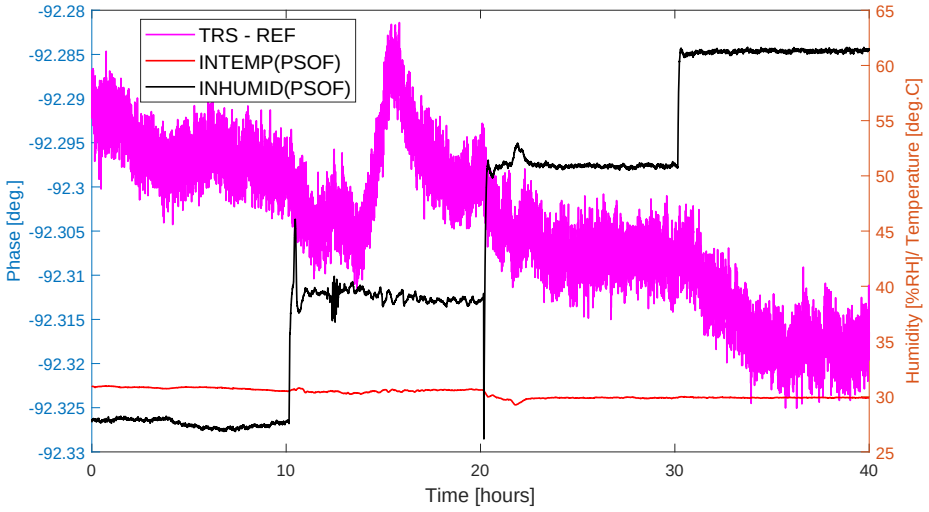

Figure 6.34: SMOC scheme under humidity change: correlation between TRS phase and relative humidity and TRS phase and temperature change inside THC (near PSOF).

Long-term Stability with Free Temperature and Humidity Change

In this experiment, the PSOF is exposed in the test hall where the temperature is controlled by air conditioner and the humidity is not controlled. Figure 6.35 shows the temperature and humidity changes in the test hall and the long-term TRS phase stability with PDFS compensation. The temperature and humidity fluctuations in the test hall are 2.11 °C and 10.74%RH, respectively. The feedback phase (RTN-REF) is stabilized within 0.62 millidegree (rms) at 2856 MHz corresponding to 0.61 fs. The long-term TRS phase is controlled within 46.5 millidegrees (pk-pk) corresponding to 45 fs, which fulfilled the requirement of 0.1° (rms).

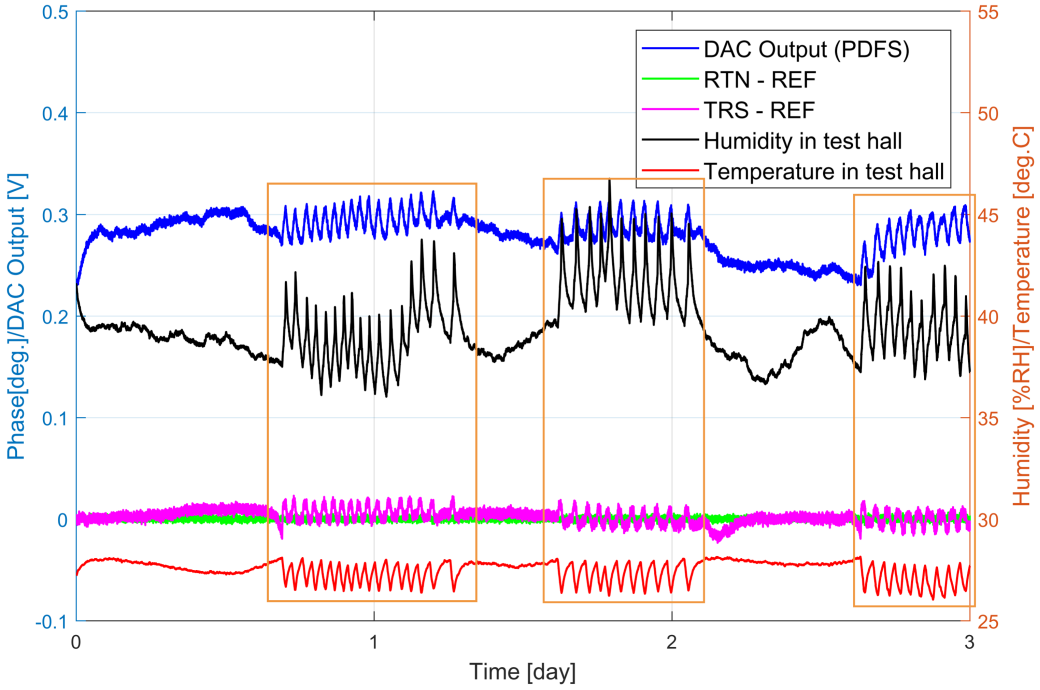

Figure 6.35: SMOC scheme: temperature and humidity changes in the test hall and the long-term TRS phase stability with PDFS compensation for three days.

In Fig. 6.35 demonstrates that the TRS phase includes the smooth slow drift as well as the oscillated phase drift (yellow boxes). The oscillated phase drift is caused by switching the working state of the air conditioner. In the yellow boxes, the air conditioner works as a cooler to control the temperature within ±1 °C and it is fluctuated. Otherwise, the air conditioner works as a heater and the temperature is neither fluctuated nor controlled.

For the oscillated phase drift, both the temperature and humidity fluctuations affected the PSOF. The correlation coefficients of the phase and temperature and phase and humidity are -0.24 and -0.09, respectively, which means the correlation is very weak. In contrast, the feedback system is only temperature stabilized, not humidity controlled. As shown in Fig. 6.36, the humidity fluctuation inside the TC influenced the RF/optical components used for the phase stabilization system. The correlation coefficient between the phase and humidity is -0.58. Although the humidity fluctuation is only 2.76%RH, they are moderately correlated.

The smooth slow drift is caused by the temperature fluctuation inside the TC. The temperature fluctuation is as small as 0.13 °C, however, the correlation coefficient between the phase and temperature is up to -0.46, which indicates that they are moderately correlated.

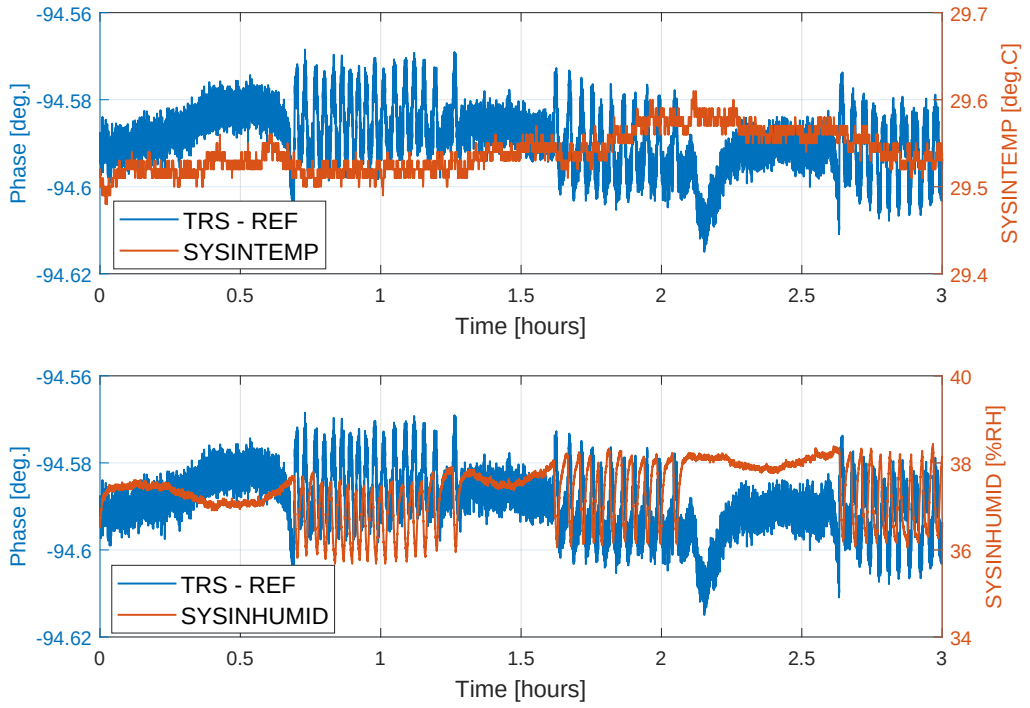

Figure 6.36: SMOC scheme: temperature and humidity changes in the test hall and the long-term TRS phase stability with PDFS compensation for four days.

Summary for SMOC Scheme

We evaluated the performance of the phase stabilization system by changing the temperature (TEMP) only, humidity (HUMID) only, and both temperature and humidity near PSOF. The measurement result is summarized in Table 6.9. The long-term jitter is as small as 10 fs (pk-pk). The TRS phase is stabilized within 56 fs (pk-pk) corresponding to 0.57 millidegrees at 2856 MHz, which fulfilled the reference phase stability requirement. The performance of the SMOC scheme with different wavelengths is comparable with the scheme with the WDM technique. This scheme can also be one of the candidates for the reference phase stabilization of the SuperKEKB injector LINAC.

Table 6.9: Summary of the long-term performance of the SMOC scheme.

	TEMP Change	**HUMID Change**	**TEMP/HUMID Change**
Time [hour]	18	40	72
TEMP [°C]	20-40	30	25-30
HUMID [%RH]	40	30-60	35-45
ΔT [°C]	20	–	2.11
ΔH [%RH]	–	30	10.74
RTN [fs] (rms)	0.67	0.63	0.61
TRS [fs] (pk-pk)	56	43	45

6.3 Comparison of Different Techniques

The phase stabilization system with WDM technique and optic circulator is implemented and tested under temperature and humidity change. Table 6.10 shows a summary of the different techniques. In conclusion, both CWDM technique and circulator scheme with different wavelength and PDFS compensation can achieve high stability of 50 fs (pk-pk) level, which fulfilled the requirement of SuperKEKB injector LINAC. Both are easy to implement and the cost is almost the same. The WDM technique is already applied in the SuperKEKB ring; however, this is the first time that a phase stabilization system is proposed and implemented using circulator with high stability. Both schemes are recommended for the SuperKEKB injector LINAC. Although the PDFS can compensate most of the phase drift, it is recommended to use VODL for coarse control and PDFS for precise control.

Table 6.10: Summary of the long-term performance with DWDM technique and circulator (wavelength: 1550.12 nm, 1551.72 nm, PDFS for length control).

Scheme	**Item Change**	**TEMP Change**	**HUMID Change**	**TEMP/HUMID**
	Time [h]	18	40	96
	TEMP [°C]	20-40	30	25-30
	HUMID [%RH]	40	30-60	40-50
	ΔT [°C]	20	–	2.55
	ΔH [%RH]	–	30	7.71
CWDM	RTN [fs] (rms)	0.66	0.62	0.59
	TRS [fs] (pk-pk)	35	56	44
SMOC	RTN [fs] (rms)	0.67	0.63	0.61
	TRS [fs] (pk-pk)	56	43	45

The wavelength difference between the forward and backward paths induced an unbalanced phase drift between the forward line (ϕ_{for}) and backward line (ϕ_{bak}). It implies the forward phase is unequal to the backward phase ($\phi_{for} \neq \phi_{bak} \neq \frac{1}{2}\phi_{rtn}$). Although the returned phase can be compensated perfectly, a small residual phase still remains in the TRS phase. To avoid this, a small difference between the forward and backward paths is recommended. In our case, wavelengths of 1550.12 nm and 1551.72 nm are selected.

Chapter 7

Phase Drift Compensation between Injector LINAC Master Oscillator and Ring Master Oscillator for Stable Beam Injection at SuperKEKB

Results presented in this chapter have already been published in [71].

7.1 Introduction and Motivation

The SuperKEKB injector LINAC that includes the positron damping ring delivers low emittance electron and positron beams to the main rings. The beam injection phase from LINAC to the rings should be stabilized for long-term stable beam injection. Low emittance beams are produced and delivered by the injector LINAC [2]. As shown in Fig. 7.1, the injector LINAC has two electron guns: a photo-cathode RF gun for low emittance electron beams and a thermionic gun for positron production. The beams are accelerated by 2856 MHz RF accelerating structures to 7 and 4 GeV for electrons and positrons, respectively. The 1.1 GeV positron damping ring was constructed in the middle of LINAC for low emittance beams. The positron beam extracted from the DR is reinjected into the 2856 MHz RF accelerating structures. To shorten the bunch length and precisely put the beam on the phase at 2856 MHz, the bunch compression system comprising a 2856 MHz accelerating structure and an arc section is placed on the beam transport line from DR to LINAC.

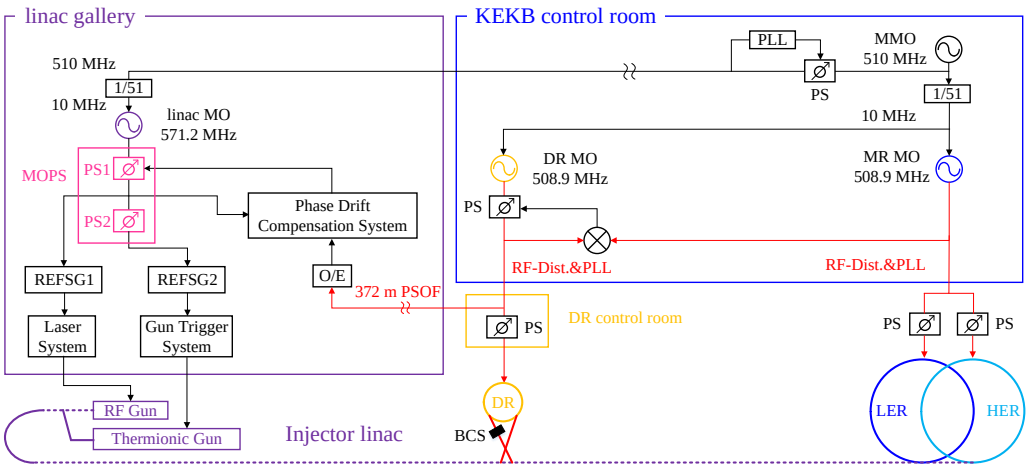

Figure 7.1: Block diagram of synchronization system for LINAC, DR, and MR. PS: phase shifter, MOPS: master oscillator phase shifter, RF-Dist.: RF reference distribution system.

Figure 7.1 describes the synchronization system for the injector LINAC, DR, and MR. The injector linac, DR, and MR have their own independent MO that belong to the commercial Agilent E8663 series [72]. They are synchronized with a 10 MHz trigger generated by the main MO (MMO) signal of 510 MHz by dividing with 51. The MMO, DR MO, and MR MO are located at the SuperKEKB center control room. The DR MO and MR MO are operated at 508.9 MHz and the phase drift between them is controlled within $\pm$ 0.1° (pk-pk) by a phase-locked loop (PLL) [14]. DR MO and MR MO are collectively called RMO in this chapter. The RF reference signals are distributed to the DR and MR through PSOF.

The LMO is operated at 571.2 MHz and located in the LINAC gallery. The 2856 MHz RF reference signal is generated by the LMO [73]. A 510 MHz signal from the MMO is transmitted to LINAC with the coaxial cable for synchronization. The phase drift of the long coaxial cable is compensated by PLL [74]. However, LMO and RMO are only synchronized with the 10 MHz trigger but without phase regulation. A phase drift of several degrees was observed between the two MOs by the phase monitor [72]. This MO phase drift significantly affected the beam energy stability after the BCS cavity in RTL owing to a five times larger phase for 2856 MHz. Furthermore, the beam injection phase tuning from the LINAC to MR had to be conducted frequently because the beam injection background has been a critical problem for the SuperKEKB Belle II detector [75]. To maintain a stable beam injection, the MO phase drift compensation system is developed. The phase stability

between the LMO and RMO is required to be less than ± 0.1° (pk-pk) at 571.2 MHz.

7.2 Direct Sampling Technique

For the long-term phase drift measurement, the long-term stability of the phase monitor system is more important than the phase detection bandwidth and response latency. To remove the effects of temperature and humidity drift in the measurement system, it is important to make the measurement system common for signals with different frequencies. The direct sampling technique, therefore, is adopted for phase detection. In this method, the input analog RF signal is directly digitized by an ADC. After the digital down-conversion, the IQ components of the RF signals are obtained [38].

In the direct sampling technique, the sampling rate f_s and the measured RF signal f_{RF} must satisfy [38, 41, 40]

$$f_s = \frac{f_{RF}}{K + \frac{N}{M}}, K = 0, 1, 2, 3... \tag{7.1}$$

where M is an integer greater than 3, N and K are integers, and M and N are prime to each other. The phase advance $\Delta\varphi$ between the two adjacent samples can be represented as

$$\Delta\varphi = (K + \frac{N}{M}) \cdot 2\pi = \frac{f_{RF}}{f_s} \cdot 2\pi \tag{7.2}$$

In our case, two different frequency signals should be detected by the same sampling rate. The sampling frequency should satisfy

$$\frac{f_1}{f_s} = K_1 + \frac{N_1}{M_1} \tag{7.3}$$

$$\frac{f_2}{f_s} = K_2 + \frac{N_2}{M_2} \tag{7.4}$$

where subscripts 1 and 2 denote LMO and RMO, respectively. The frequency ratio of LMO (571.2 MHz) and RMO (508.9 MHz) is 55:49; thus, f_2 can be expressed by f_1 as

$$\frac{f_2}{f_s} = \frac{49}{55} \cdot \frac{f_1}{f_s} = \frac{49}{55} \cdot (K_1 + \frac{N_1}{M_1}) \tag{7.5}$$

Under the condition that $K_1M_1 + N_1 = 55$, we have $f_1/f_s = 55/M_1$ and $f_2/f_s = 49/M_1$.

The I and Q components are calculated using Eqs. (3.10) and (3.11), respectively. The RF phase is obtained by $\phi = \arctan(Q/I)$.

7.3 Sampling Clock Generation

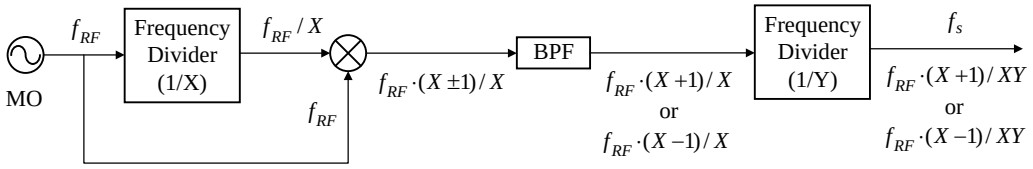

Figure 7.2: Block diagram of sampling clock generation for direct sampling technique.

Figure 7.2 shows the block diagram of sampling clock generation for the direct sampling technique [77, 78]. First, the RF signal (f_{RF}) generated by MO is divided by X to obtain f_{RF}/X. Then, f_{RF}/X is mixed with f_{RF} to obtain another frequency $f_{RF}\cdot(X\pm1)/X$. This output frequency is filtered by a BPF to obtain the frequency $f_{RF}\cdot(X+1)/X$ or $f_{RF}\cdot(X-1)/X$. Finally, the selected frequency is divided by Y using another frequency divider to generate the required sampling rate f_s, which can be represented as

$$f_s = \frac{f_{RF}}{\frac{XY}{X\pm1}} \tag{7.6}$$

where X and Y are both integers.

In our case, the sampling clock is generated based on LMO. From simultaneous Eqs. (7.3) and (7.6), it can be concluded that $K_1M_1+N_1 = XY = 55$ and $M_1 = X \pm 1$. Thus, X and Y are either 5 or 11. The possible combinations of the sampling rate are summarized in Table 7.1. According to the non-IQ algorithm [79], the coefficients $K_{1,2}$, $N_{1,2}$, and $M_{1,2}$ for IQ estimation are listed in Table 7.2. Combination 2 with $M_1 = 2$ and $N_1 = 1$ does not satisfy the IQ sampling condition.

The sampling clock is generated by two frequency dividers (AD9516, Analog Devices, Inc.) and the ADC performance is very sensitive to the clock jitter. According to the non-IQ algorithm, the clock-jitter-induced measurement errors can be digitally reduced by averaging over M samples [38]. Thus, the 124.63 MHz sampling rate is chosen for the phase monitor system owing to lower jitter and larger M ($M_1 = M_2 = 12 > 6, 4$). The integral jitter of the sampling clock is measured using the signal source analyzer (E5052B, Agilent Technologies) in the laboratory and then applied to the injector LINAC. Figure 7.3 shows the SSB phase noise power spectrum of the 124.63 MHz sampling clock. The integral jitter is 126.48 fs corresponding to 5.7 millidegrees

from 10 Hz to 10 MHz. The center frequency of the BPF used for the clock generation is 623 MHz and the bandwidth is ±10 MHz. It is a waterproof-type BPF that relatively reduces the humidity effect on the phase monitor system. It is customized by Sogo Electronics, Inc. [76].

Table 7.1: Possible combinations of the sampling rate.

Combination	**Mixer**	X	Y	M_1	**Clock [MHz]**
1	+	11	5	12	124.63
2	-	11	5	10	103.85
3	+	5	11	6	63.31
4	-	5	11	4	41.54

Table 7.2: Possible combinations for the coefficients of non-IQ algorithm for LMO and RMO.

Combination	M_1	K_1	N_1	M_2	K_2	N_2
1	12	4	7	12	4	1
2	2	5	1	10	4	9
3	6	9	1	6	8	1
4	4	13	3	4	12	1

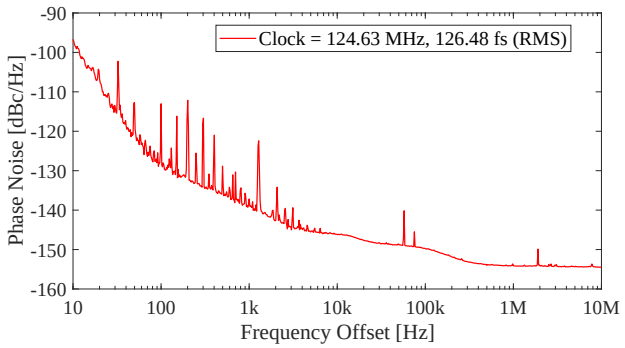

Figure 7.3: SSB phase noise power spectrum of sampling clock.

7.4 Phase Monitor System

The configuration of the phase monitor system is shown in Fig. 7.4. The 571.2 MHz signal generated by the SG, which is split into two: one is for sampling clock generation and the other is fed to the MO phase shifter (MOPS)

used for the beam injection phase adjustment to HER or LER [80]. The output signal of MOPS is monitored. The MOPS and phase monitor system are situated inside the temperature stabilized chamber with 28±0.1 °C to reduce the phase drift of the RF components.

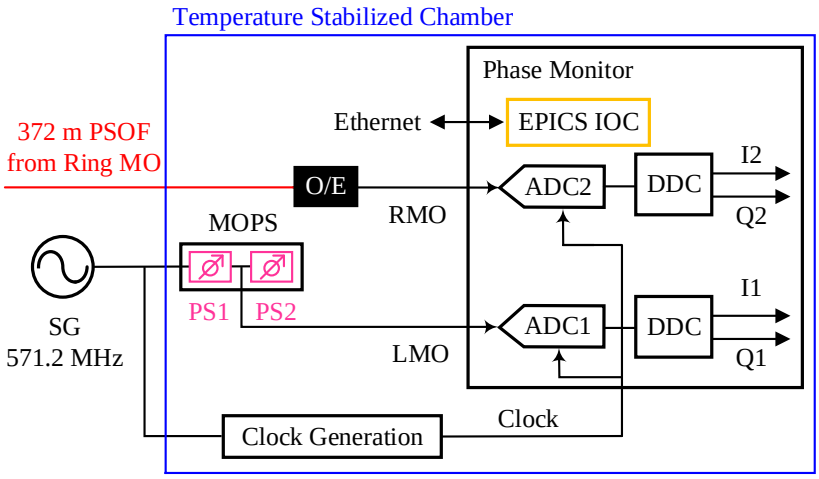

Figure 7.4: Phase monitor system for LMO and RMO.

The RF reference signal of the RMO is delivered from the DR control room to the LINAC gallery through the 372 m phase stabilized optical fiber (PSOF). The PSOF is provided by Furukawa Electric Co., Ltd. [53] with excellent thermal propagation time delay, as low as 0.4 ppm/°C from 25 °C to 30 °C [81]. This range covers the temperature changes in the LINAC gallery. A majority of the PSOF is distributed inside the gallery where the temperature is regulated at 28±1 °C by the air conditioner. The PSOF phase drift caused by the temperature fluctuation is estimated to be less than 1.5 ps (pk-pk) corresponding to 0.27° for RMO. The optical signal from the RMO is converted to the electrical signal by an O/E and then monitored.

The phase monitor was implemented in a digital board based on MTCA.0 standard. The same board is used in [14, 78, 82, 83]. This board is equiped with Xilinx Virtex-5 FXT FPGA, two 14-bit ADCs (400 MSPS high-speed, 1.44 GHz input bandwidth, ADS5474), and embedded with an input/output controller (IOC) application based on Experimental Physics and Industrial Control System (EPICS). The LMO and RMO signals are digitized by ADCs with a sampling rate of 124.63 MHz. The ADC samples for the LMO and RMO are described in Fig. 7.5. Finally, the IQ components are obtained by DDC based on Eq. (3.10) and (3.11).

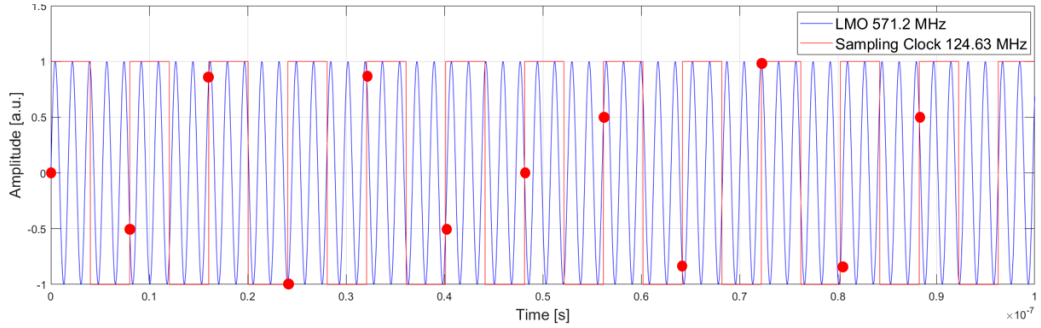

(a) ADC samples for LMO signal.

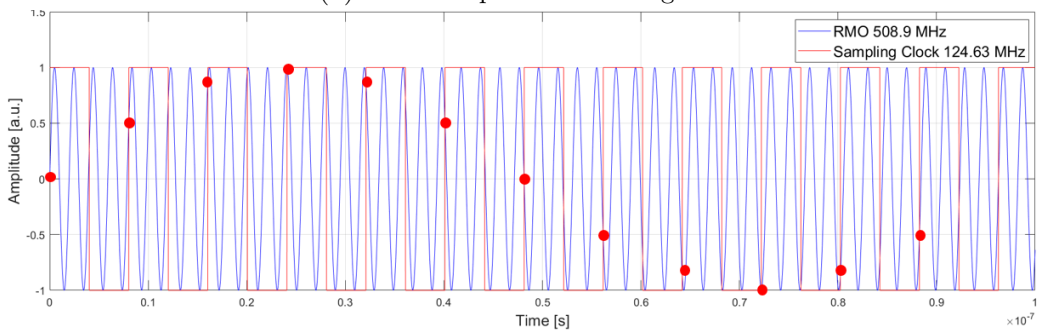

(b) ADC samples for RMO signal.

Figure 7.5: ADC samples for LMO and RMO signals.

7.4.1 Short-term Stability

Short-term phase stability without digital filter is presented in Fig. 7.6. The phase stabilities of LMO (571.2 MHz) and RMO (508.9 MHz) are 0.078° (rms) and 0.064° (rms), respectively. To improve the phase stability, a digital LPF with a bandwidth of 100 Hz is applied to suppress the clock jitter and ADC noise [43].

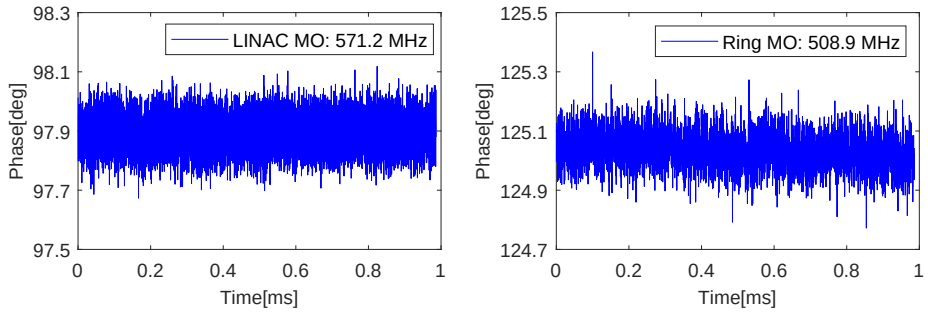

Figure 7.6: Short-term phase stability of LMO and RMO.

7.4.2 Long-term Phase Drift

The long-term MO phase difference is shown in Fig. 7.7. The RF phases of LMO (ϕ_{LMO571}) and RMO (ϕ_{RMO509}) are calculated at 571.2 MHz and 508.9 MHz, respectively. After the RMO phase is normalized to the LMO frequency, the phase difference ($\phi_{DIFF571}$) is calculated as

$$\phi_{RMO571} = 571.2/508.9 \cdot \phi_{RMO509} \tag{7.7}$$

$$\phi_{DIFF571} = \phi_{RMO571} - \phi_{LMO571} \tag{7.8}$$

where ϕ_{RMO571} is the RMO phase represented at 571.2 MHz.

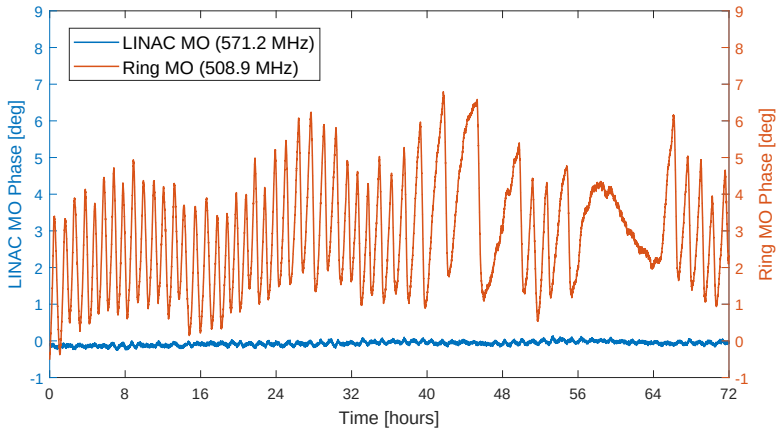

(a) Phase drift of LMO (blue) and RMO (orange).

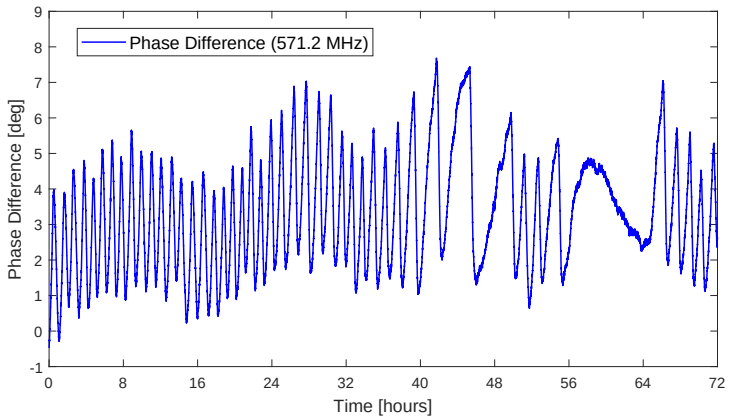

(b) Phase difference between LMO and RMO.

Figure 7.7: Phase difference between LMO and RMO for three days.

As shown in Fig. 7.7(a), the LMO phase drift is 0.39° (pk-pk) at 571.2 MHz and the RMO phase drift is 7.31° (pk-pk) at 508.9 MHz. Because the sampling clock was generated by LMO, the phase drift of LMO is much smaller

than that of RMO. The phase difference between LMO and RMO is observed to be 8.16° (pk-pk) over three days, as shown in Figure 7.7(b). The period of the phase difference varies from 1 to 5 h. As mentioned above, the RMO is located in the KEKB control room where the temperature is controlled within ±1 °C by the air conditioner. However, a strong periodic temperature fluctuation is caused by the working condition of the air conditioner. In addition, the period of this temperature fluctuation matches that of the MO phase difference. Thus, the MO phase difference is correlated with the room temperature of the KEKB control room.

7.5 MO Phase Difference Effects on Beam Performance at BCS

The layout of the beam transport lines between the injector LINAC and the DR is shown in Fig. 7.8 [84]. Figure 7.9 shows the horizontal beam positions of two BPMs. BPM1 is located at the first arc section after DR extraction. BPM2 is located at the second arc section after the 2856 MHz accelerating structure of BCS. There is no slow drift at BPM1; however, it shows a clear slow drift at BPM2. As shown in Fig. 7.8, the extracted positron beam from the DR is accelerated by the BCS cavity operated at 2856 MHz. This 2856 MHz signal is generated by LMO but the RF of the DR is provided by the RMO. It is found that the slow drift of the horizontal beam position at BPM2 depends on the phase difference between LMO and RMO.

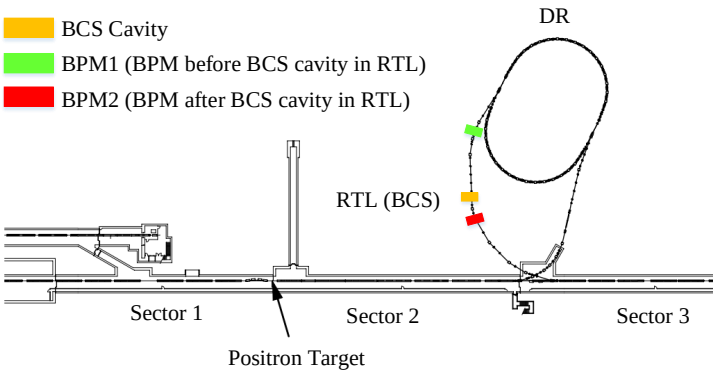

Figure 7.8: Layout of beam transport lines between injector LINAC and DR. Locations of two BPMs are marked in the beam transportation line.

To confirm the relationship between the BCS RF phase and the horizontal beam position, the RF phase was scanned. Figure 7.10 shows the mea-

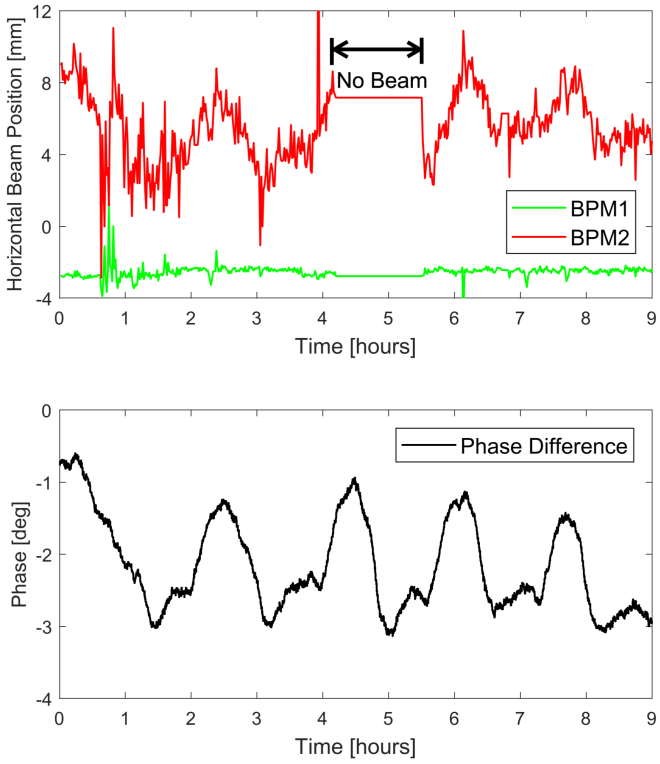

Figure 7.9: Horizontal beam position at BPM1 and BPM2 (top) and the phase difference between LMO and RMO (bottom) without phase drift compensation system for 9 h.

surement result. The slope of the linear fitting equation is $-0.517\,\mathrm{mm}/^\circ$ at 2856 MHz. In Fig. 7.9, slow drift in the horizontal beam position is observed approximately at 6 mm. The 6 mm deviation corresponds to 11.6° BCS phase change at 2856 MHz (pk-pk). Meanwhile, the observed MO phase difference is 2.3° at 571.2 MHz (pk-pk), which corresponds to 11.5° at 2856 MHz. These two results are consistent. The MO phase difference is too large to satisfy the requirement of ± 0.1° (pk-pk) at 571.2 MHz; therefore, the phase drift compensation system is developed.

7.6 Phase Drift Compensation

The LINAC RF phase should be shifted based on the injection mode of HER and LER at the 50 Hz repetition rate. However, a fast phase change is not allowed for the laser system of the photo cathode RF gun, as shown in Fig. 7.1. MOPS is installed to satisfy the requirement of the laser system and

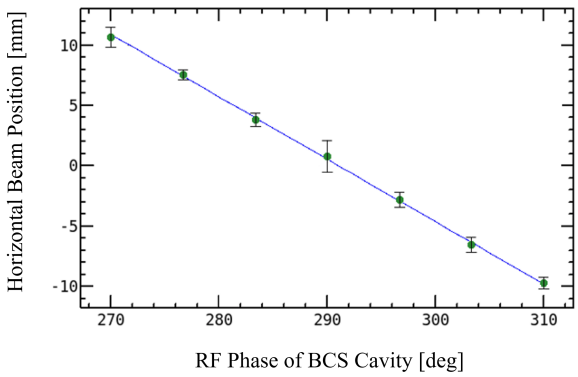

Figure 7.10: Horizontal beam position as a function of 2856 MHz RF phase of BCS cavity. The slope is $-0.517\,\mathrm{mm}/^\circ$.

the injection phase adjustment [80]. MOPS consists of two phase shifters, PS1 and PS2. PS1 is located upstream and fixed at the HER injection phase. The PS1 output signal is sent to the laser system. PS2 is located downstream and is changed every 20 ms depending on injection modes. For MO phase drift compensation, the LMO phase is changed to follow the RMO phase using MOPS.

As mentioned above, MOPS is used for beam injection phase adjustment as well as phase drift compensation. Thus, the monitored phase drift of LMO includes the injection phase change. For phase drift evaluation, the amount of injection phase change is removed by calculation. The MO phase difference is fed back to MOPS through the EPICS record. A proportional–integral (PI) controller is applied for precise feedback control. Figure 7.11 shows the long-term phase difference between LMO and RMO with compensation. The LMO successfully follows RMO and the phase difference between them is compensated within 0.018° (rms) at 571.2 MHz, which fulfilled the phase stability requirement of ± 0.1° (pk-pk).

The horizontal beam position results with MO phase drift compensation are shown in Fig. 7.12. The large slow drift of the horizontal beam position at BPM2 is compensated. The energy jitter with the stability of 0.7 mm (rms) still remains, however, it is not caused by the MO phase difference. The possible sources are the klystron high voltage fluctuation, the LLRF control unit and the measurement error of BPM2. Thus, the slow drift of the beam energy is stabilized by the MO phase drift compensation system. This system is successfully used in the SuperKEKB operation.

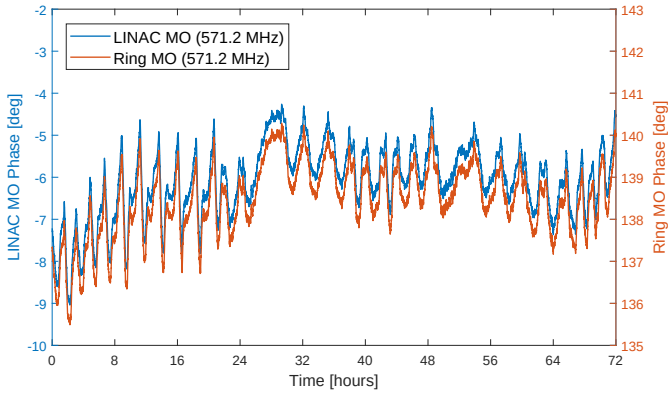

(a) Phase drift of LMO (blue) and RMO (orange).

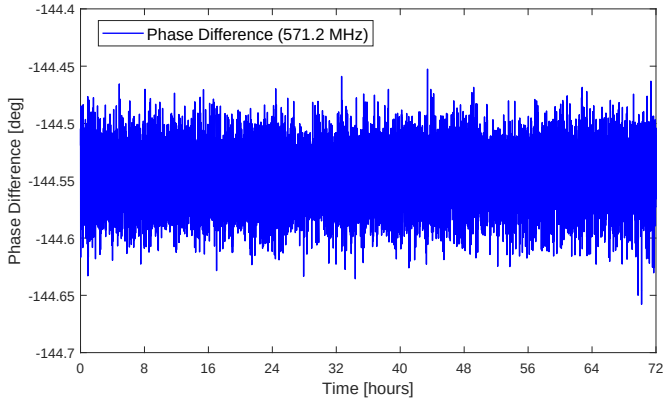

(b) Phase difference between LMO and RMO.

Figure 7.11: Phase difference between LMO and RMO with compensation.

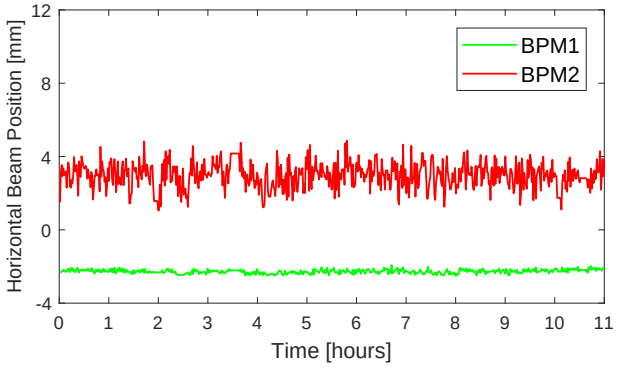

Figure 7.12: Horizontal beam position at BPM1 and BPM2 with the phase drift compensation system for 11 h.

Chapter 8

Summary and Future Prospects

This thesis mainly consists of two parts, i.e., the phase drift compensation system for the RF reference distribution system with optical link at SuperKEKB injector LINAC and the phase drift compensation between LINAC MO and RMO.

RF Reference Phase Stabilization at injector LINAC

- The requirement of RF reference phase stability was estimated to be as 0.2° (rms) at 2856 MHz according to the requirement of the energy spread at the end of injector LINAC, which is 0.07%. The long-term phase drift requirement was 0.1° (rms) at 2856 MHz corresponding to 100 fs.

- The timing jitter and the long-term phase drift in the optical link were first measured at injector LINAC. A phase drift of 5° to 6° was observed in the transmitted phase at each sector, which cannot fulfill the requirement.

- It was found that the humidity effect was quite significant. The temperature and humidity coefficients of the PSOF, E/O, and O/E modules were measured. These coefficients can be used to estimate the phase drift caused by the temperature and humidity fluctuations.

- Reference tracking method was applied to compensate the phase drift of the monitor system. The long-term stability can achieve 0.03° (pk-pk) at 2856 MHz corresponding to 28 fs.

- A RF reference phase stabilization system using WDM technique or optic circulator was implemented and the performance was found to be

comparable. With PDFS compensation, the RF reference phase was stabilized to 50 fs (pk-pk) level, which fulfilled the requirement.

In the near future, the RF reference phase stabilization system will be implemented in injector LINAC and both schemes (WDM technique, optic circulator) of the phase stabilization system can be the candidates. The possible configuration of the RF reference phase stabilization system for SuperKEKB injector LINAC is shown in Fig. 8.1.

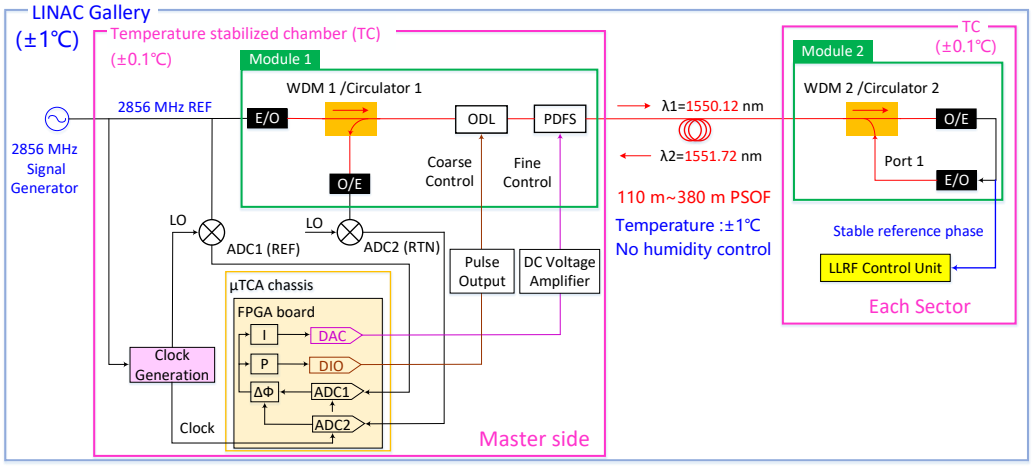

Figure 8.1: Possible configuration of the RF reference phase stabilization system for SuperKEKB injector LINAC.

- For optical length control, VODL is recommended for the coarse control and large phase adjustment range in real RF operation.
- The optical components should be temperature stabilized and sealed with stable humidity to improve the transmitted phase stability.

Phase Drift Compensation between LINAC MO and RMO

- A phase monitor system was implemented. The LMO (571.2 MHz) and RMO (508.9 MHz) were directly sampled by ADC using the direct sampling technique with a common sampling rate. A phase drift of more than 8° (pk-pk) was observed between the LMO and RMO.
- A phase drift compensation system was implemented and the MO phase drift was stabilized within 0.018° (rms) at 571.2 MHz, which fulfilled the requirement of ±0.1 MHz (pk-pk). The system performance was

confirmed by the beam energy stability after the BCS cavity. This system is successfully used in SuperKEKB operations.

Appendix A

Temperature and Humidity Coefficients Measurement of Coaxial Cables

The coaxial cable is widely used for transporting high performance measurement signal (e.g., phase monitor system) and stable machine synchronization signals (e.g. RF reference distribution). The RF signal suffers time delay while passing through the coaxial cable. The characteristics of the coaxial cable directly affect the propagation time delay (phase drift) due to the fluctuations in temperature and humidity. A coaxial cable with a small propagation time delay is necessary for abhigh precision phase monitor system.

Phase drift is a slow change in the phase length of the coaxial cable. It can be expressed in degrees by

$$\Delta\phi_{coax} = \frac{360fl\sqrt{\varepsilon_r}}{c} \tag{A.1}$$

where ϕ_{coax} is the phase drift in degrees, f is the signal frequency, l is the cable length, c is the light speed in vacuum, and ε_r is the dielectric constant of the dielectric material filling the space between the center and the outer conductor of the coaxial cable.

To measure the temperature and humidity coefficients of the coaxial cable, a similar setup, as shown in Fig. A.1, is used. The coaxial cable (10 m) is situated inside the temperature and humidity controlled chamber to change the temperature and humidity. The phase change is measured by port 3 and port 4 (S43) of the network analyzer, which is located inside the temperature stabilized chamber. To reject the system phase drift, a same length (5 m) of coaxial cable is adopted and its phase drift is monitored by port 1 and port 2 (S21) for reference.

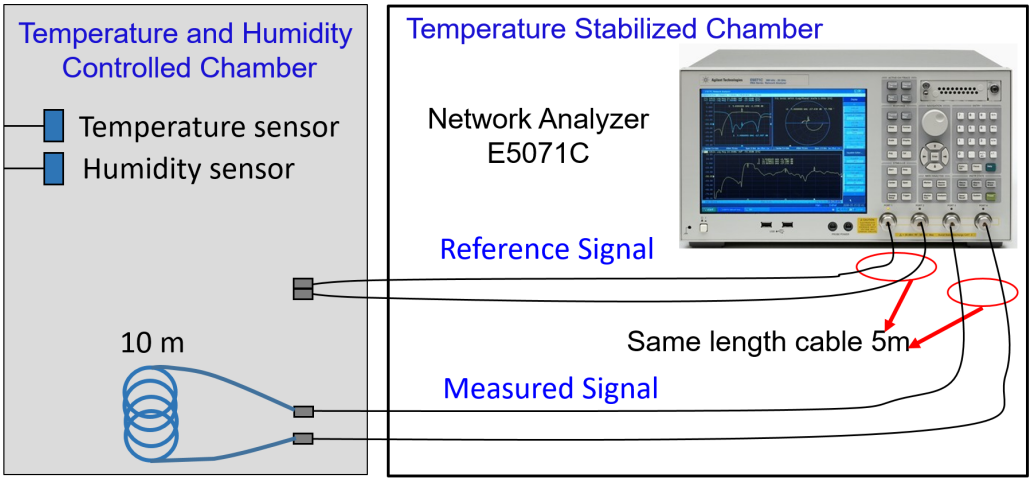

Figure A.1: Measurement setup for coaxial cables.

Several types of coaxial cable, which are widely used in our laboratory, are purchased from different manufacturers. The measurement result is shown in Table A.1. The property of the Andrew cable and the HUBER+SUHNER cable are very good in comparison to others. The HUBER+SUHNER cable is widely used in the phase monitor system at injector LINAC owing to its flexural characteristics.

Table A.1: Temperature and humidity coefficient of Coaxial Cables.

Manufacturer	Candox	Andrew	HUBER+SUHNER	Candox	Candox
Type	5B-008X-23	FSJ1RK-50B	S-04272-B	5B-020-33	5B-045-94
Photo					
Length	10 m	7 m	10 m	10 m	10 m
Temperature Range			25°C - 40°C		
Temperature Coefficient	145 ps/km/°C	24 ps/km/°C	-30 ps/km/°C	84 ps/km/°C	-19 ps/km/°C
Humidity Range			50%RH -70%RH		
Humidity Coefficient	-23 ps/km/%RH	-0.5 ps/km/%RH	-0.25 ps/km/%RH	-3.7 ps/km/%RH	-2.5 ps/km/%RH

Abbreviations

rms	Root mean square
pk-pk	Peak to peak
RF	Radio frequency
LINAC	Linear accelerator
MO	Master oscillator
LMO	LINAC master oscillator
PSOF	Phase-stabilized optical fiber
WDM	Wavelength division multiplexing
DR	Damping ring
RMO	Ring MO
HER	High-energy ring
LER	Low-energy ring
SHB	Sub-harmonic buncher
SLED	SLAC energy doubler
SB	Sub-booster klystron
SSA	Solid state amplifier
RSG	Reference signal generator
BL	Bunch length
SACLA	SPring-8 Angstrom compact laser
CW	Continuous wave
SG	Signal generator
E/O	Electrical/optical converter
O/E	Optical/electrical converter
LLRF	Low level radio frequency
NIM	Nuclear instrument module
FPGA	Field programmable gate array
ADC	Analog-to-digital converter
I	In-phase component
Q	Quadrature-phase component
IIR	Infinite impulse response
LPF	Low-pass filter
VODL	Variable optical delay line
VVM	Vector volt meter
ECLD	External cavity laser diode
AOM	Acoustic optical modulator
PBS	Polarization beam splitter
PDFS	Piezo-driven fiber stretcher

FRM	Faraday rotating mirror
BPF	Band-pass filter
PD	Photo-diode
PFD	Phase frequency discriminator
PID	Proportional–integral–derivative controller
XFEL	X-Ray free-electron laser
DESY	Deutsches Elektronen-Synchrotron
RFS	RF station
BPM	Beam position monitor
MLO	Master laser oscillator
PRDS	Phase reference distribution system
L2RF	Laser-to-RF
FSD	Free-space distribution
LSU	Link stabilization unit
PM	Polarization-maintaining
OXC	Optical cross-correlator
ODL	Optical delay line
PARL	Phase averaging reference line
NLC	Next Linear Collider
SF	Suppression factor
REF	Reference signal
SSB	Single side band
IF	Intermediate frequency
LO	Local oscillator
SR	Sampling rate
DSP	Digital signal processor
SNR	Signal-to-noise ratio
DDC	Digital down conversion
NCO	Numerically controlled oscillator
FD	Frequency divider
μTCA/MTCA	Micro telecommunications computing architecture
AMC	Advanced mezzanine card
DAC	Digital-to-analog converter
DIO	Digital input/output
REFn	Reference signal of board$n$
SOPTR	Returned signal of the short optical link
SBnOPTR	Returned signal of the optical link at sector n
SOPT	Phase drift of the short optical link
SBnOPT	Phase drift of the optical link at sector n
SBnTRS	Transmitted phase drift of the optical link at sector n

LCP	Liquid crystal ploymer
RH	Relative humidity
SBnH	Humidity inside the chamber at sector n
SBnGT	Temperature in LINAC gallery at sector n
BBB	Beagle Bone Black
NA	Network analyzer
THC	Temperature and humidity controlled chamber
TC	Temperature stabilized chamber
DUT	Device under test
CAL	Calibrated phase drift
SIG	Signal to be measured
TPE	Temperature induced phase error
SREF	Reference of the short optical link
SSIG	Phase drift of the short optical link
SCAL	Calibrated phase drift of the short optical link
STPE	Temperature induced phase error of the short optical link
CSCAL	Corrected SCAL phase
TTC	Two-tone calibration
LBNL	Lawrence Berkeley National Laboratory
DCM	Drift compensation module
RTC	Reference tracking
PCB	Printed circuit board
cERL	Compact energy recovery linac
DSBSC	Double side-band suppressed carrier
VCXO	Voltage-controlled crystal oscillator
FLASH	Free Electron Laser in Hamburg
CLK	Clock
REFn	Reference phase measured by ADCn
RTCn	Reference tracking between ADCn and ADC1
CWDM	Coarse wavelength division multiplexing
DWDM	Dense wavelength division multiplexing
TRS	Transmitted signal
RTN	Returned signal
I	Integral controller
PZT	Piezoelectric ceramics
TTL	Transistor-transistor logic
CH	Channel
PDL	Polarization dependent loss

SYSINTEMP	Temperature inside the TC (feedback system located)
SYSINHUMID	Humidity inside the TC (feedback system located)
INTEMP(PSOF)	Temperature inside the THC (POSF located)
INHUMID(PSOF)	Humidity inside the THC (POSF located)
TEMP	Temperature
HUMID	Humidity
SMOC	Single mode optic circulator
FC	Fiber-optic connector
APC	Angled physical contact fiber connector
FFT	Fast Fourier transform
BCS	Bunch compression system
RTL	DR to LINAC
PS	Phase shifter
MOPS	Master oscillator phase shifter
RF-Dist.	RF reference distribution system
MMO	Main master oscillator
PLL	Phase-locked loop
EPICS	Experimental Physics and Industrial Control System
PI	proportional-integral controller

List of Figures

List of Tables

Bibliography

[1] Y. Ohnishi *et al.*, Accelerator design at SuperKEKB, Prog. Theor. Exp. Phys., 03A011 (2013).

[2] M. Akemoto *et al.*, The KEKB injector linac, Prog. Theor. Exp. Phys., 03A002 (2013).

[3] M. Kikuchi, Reverse-bend FODO lattice applied to damping ring for SuperKEKB, Nucl. Instrum. and Methods in Phys. Research A, 556 (2006).

[4] M. Kikuchi *et al.*, Design of positron damping ring for SUPER-KEKB, in *Proceedings of International Particle Accelerator Conference (IPAC'2010), Kyoto, Japan*, TUPEB054, p. 1641.

[5] Belle II detector, `https://www.belle2.org/`

[6] Y. Yano *et al.*, RF control system for SuperKEKB injector linac, in *Proceedings of 11th Annual Meeting of Particle Accelerator Society of Japan (PASJ'2014), Aomori, Japan*, SAP054, p. 624.

[7] Z. D. Farkas, *et al.*, SLED: a method of doubling SLAC's Energy, in *Proceedings of 9th International Conference on High Energy Accelerators 1974, California, USA*, p. 576.

[8] T. Miura *et al.*, LLRF control unit for SuperKEKB injector LINAC, in *Proceedings of International Particle Accelerator Conference (IPAC'2018), Vancouver, Canada*, WEPAK018, p. 2134.

[9] Kazunori Akai, Kazuro Furukawa, Haruyo Koiso, on behalf of the SuperKEKB accelerator team, SuperKEKB collider, Nuclear Inst. and Methods in Physics Research, A 907 (2018),pp. 188–199.

[10] Kazunori Akai, Kazuro Furukawa, Haruyo Koiso, on behalf of the SuperKEKB accelerator team, Injector Linac Experiences at KEKB / SuperKEKB, in *Oral presentation of the second annual meeting of the Future Circular Collider study (FCC'2016), Rome, Italy.*

[11] Y. Ogawa *et al.*, Wake field issues concerning the KEKB factory injector linac, in *Proceedings of the 1994 International Linac Conference, Tsukuba, Japan*, p. 535-536.

[12] P. B. Wilson, High energy electron linacs: Applications to storage ring RF systems and linear colliders, SLACPUB-2884 (1982).

[13] Thomas Schilcher, Vector sum control of pulsed accelerating fields in Lorentz force detuned superconducting cavities, PhD thesis, 1998.

[14] T. Kobayashi *et al.*, RF Reference Distribution System for SuperKEKB, in *Proceedings of 10th Annual Meeting of Particle Accelerator Society of Japan (PASJ'2013), Nagoya, Japan*, SUP094, p. 1159.

[15] T. Kobayashi *et al.*, RF reference distribution system for J-PARC linac, Nuclear Instruments and Methods in Physics Research A 585 (2008) p. 12–19.

[16] K. Sato *et al.*, Development of actively controlled ultra phase stable reference signal transfer system, in *Proceedings of the meeting on engineering and technology in basic research (1999)*, KEK Proc, 99-16, MET043, p. 153-156.

[17] T. Naito *et al.*, Development of Timing Distribution System with Femtosecond Stability, in *Proceedings of International Particle Accelerator Conference (IPAC'2011), San Sebastián, Spain*, MOPC146, p. 421-423.

[18] H. Maesaka *et al.*, Design and performance of the optical fiber length stabilization system for SACLA, in *Proceedings of International Particle Accelerator Conference (IPAC'2014), Dresden, Germany*, WEOBB01, p. 1906-1908.

[19] Y. Otake *et al.*, Timing and low-level rf system for an x-ray laser, Physical Review Accelerators and Beams 19, 022001 (2016).

[20] R. Wilcox *et al.*, Stable Transmisson of radio frequency signals on fiber links using interferometric delay sensing, in *Proceedings of Beam Instrumentation Workshop (BIW'2010), Santa Fe, New Mexico, US*, TUPSM081, p. 372-374.

[21] J. Frisch, D. G. Brown, and E. L. Cisneros, Performance of the prototype NLC RF phase and timing distribution system, in *Proceedings of the 9th Beam Instrumentation Workshop (BIW 2000), Cambridge, MA*, May 8 – 11, 2000.

[22] K. Czuba *et al.*, Overview of the RF synchronization system for the European XFEL, in *Proceedings of International Particle Accelerator Conference (IPAC'2013), Shanghai, China*, WEPME035, p. 3001-3003.

[23] M. Ferianis *et al.*, All-optical femtosecond timing system for the FERMI@ELETTRA FEL, in *Proceedings of 33rd International Free Electron Laser Conference (FEL'2011), Shanghai, China*, FROAI2, p. 641-647.

[24] D. Barrientos, J. Molendijk, Phase Stabilization over a 3 km Optical Link with Sub-picosecond Precision for the AWAKE Experiment, 2016 IEEE-NPSS Real Time Conference (RT), DOI: 10.1109/RTC.2016.7543132.

[25] T. Kakuta, S. Tanaka, LPC coated optical fiber with zero thermal coeffient of transmission delay time, in *Proceedings of International Wire and Cable Symposium*, 1987, pp. 234–240.

[26] Y. Okada *et al.*, Direct Sampling of RF Signal for 1.3 GHz Cavity, in *Proceedings of Particle Accelerator Conference (IPAC'2009), Vancouver, British Columbia, Canada*, WE5PFP088 , p. 2216-2218.

[27] Y. Otake *et al.*, Timing and low-level rf system for an x-ray laser, Physical Review Accelerator and Beams 19, 022001 (2016).

[28] P. Hariharan, Optical Interferometry, 2nd edition. (Elsevier, New York, 2003), p. 24.

[29] Massimo Altarelli *et al.*, The European X-Ray Free-Electron Laser Technical Design Report. `https://xfel.desy.de/localfsExplorer_read?currentPath=/afs/desy.de/group/xfel/wof/EPT/TDR/XFEL-TDR-final.pdf`

[30] F. Zummack *et al.*, Custom optomechanics for the optical synchronization system at the European XFEL, in *Proceedings of International Particle Accelerator Conference (IPAC'2017), Copenhagen, Denmark*, THPAB110, p. 3976-3978.

[31] T. Lamb *et al.*, Design and operation of the integrated 1.3 GHz optical reference module with femtosecond precision, in *Proceedings of Particle Accelerator Conference (IPAC'2017), Copenhagen, Denmark*, THPAB105 , p. 3963-3965.

[32] J.Mueller, DESY Friday Seminar, Nov. 2018.

[33] Ed Cullerton, Brian Chase, 1.3 GHz Phase Averaging Reference Line, in *oral presentation of low level RF workshop (LLRF'2011), Hamburg, Germany.*

[34] Ed Cullerton, 1.3 GHz Phase Averaging Reference Line for Fermilab's NML, in *oral presentation of the 5th Low-Level Radio Frequency workshop (LLRF'2011), Hamburg, Germany*, Oct. 17-20, 2011. `https://indico.desy.de/indico/event/3391/session/6/contribution/27/material/slides/0.pptx`

[35] Ed Cullerton, B. Chase, The Design and Performance of the Fermilab ASTA Phase Averaging 1300 MHz Phase Reference Line, in *Presentation of the 6th Low-Level Radio Frequency workshop (LLRF'2013), California, USA*, Oct. 1-4, 2013. `https://conferences.lbl.gov/event/27/session/23/contribution/79/material/poster/0.pdf`

[36] B. Chase and E. Cullerton, 1.3 GHz Phase Averaging Reference Line for Fermilab's NML ASTA Program, in *Beams-doc-3806-v2.*

[37] Dominik Sikora, K. Czuba *et al.*, Phase Drift Compensating RF Link for Femtosecond Synchronization of E-XFEL, Real Time Conference 2018, Contribution no 566.

[38] T. Schilcher, RF Application in Digital Signal Processing, in *Proceedings of CERN Accelerator School on Digital Signal Processing, (CAS2007), Sigtuna, Sweden, 2007*, p. 249.

[39] P. Poshala, Why Oversample when undersampling can do the job? Texas Instruments, Application Rep. SLAA594A, (2013).

[40] Z. Geng, S. N. Simrock, Evaluation of fast ADCs for direct sampling RF filed detection for the European XFEL and ILC, in *Proceedings of Linear Accelerator Conference (LINAC'2008), Victoria, Canada*, THP102, p. 1030.

[41] M. Grecki, T. Jezynski, and A. Brandt, Estimation of IQ vector components of RF field–theory and implementation, in *Proceedings of 12th*

Mixed Design of Integrated Circuits and Systems (MIXDES'05, Krakow, Poland, 2005, p. 783.

[42] S. Jablonski *et al.*, 2π low drift phase detector for high-precision measurements, IEEE transactions on nuclear science, vol. 62, NO. 3, (2015)

[43] F. Qiu *et al.*, Progress in the work on the tuner control system of the cERL at KEK, in *Proceedings of International Particle Accelerator Conference (IPAC'2016), Busan, Korea*, WEPOR033, p. 2743.

[44] TAMAGAWA ELECTRONICS CO.,LTD, `http://www.tmele.jp/english_top.htm`

[45] N. Liu *et al.*, The consideration of RF phase reference distribution system for the injector LINAC of SuperKEKB, in *Proceedings of 14th Annual Meeting of Particle Accelerator Society of Japan (PASJ'2017), Hokkaido, Japan*, WEP065, pp. 1015-1018.

[46] A. H. Hartog, A. J. Conduit, D. N. Payne, Variation of pulse delay with stress and temperature in jacketed and unjacketed optical fibres, Optical and Quantum Electronics 11 (1979), pp. 265-273.

[47] G. A. McBEAN, J. A. ELLIOTT, Pressure and humidity effects on optical refractive-index fluctuations, Boundary-LayerMeteorology 20 (1981), pp. 101-109.

[48] B. R. Bean, E. J. Dutton, Radio Meteorology, Nat. Bur. Standards Monograph 92 (1966), pp. 435.

[49] C. A. Friehe, J. C. LaRue, F. H. Champagne, C. H. Gibson, and G. F. Dreyer, Effects of Temperature and Humidity Fluctuation on the Optical Refractive Index in the Marine Boundary, J. Optical Sot. Amer. 65 (1975), pp. 1502-1511.

[50] H. C. Martin, Humidity and Temperature Microstructure near the ground, Quart. J. Roy. Meteorol. Sot. 98, pp. 440-446

[51] T. Kakuta, S. Tanaka, LPC coated optical fiber with zero thermal coefficient of transmission delay time, in *Proceedings of International Wire and Cable Symposium, 1987*, pp. 234–240.

[52] T. Kobayashi *et al.*, RF Reference Distribution System for J-PARC linac, Nucl. Instrum. Methods Phys. Res. A, 585 (2008), pp. 12–19.

[53] Furukawa Electric, `https://www.furukawa.co.jp/en`

[54] J. Wang and K. Petermann, Small signal analysis for dispersive optical fiber communication systems, J. Lightw. Technol., vol. 10, no. 1, pp. 96–100, Jan 1992.

[55] M. J. Hamp, J. Wright, M. Hubbard, and B. Brimacombe, Investigation into the temperature dependence of chromatic dispersion in optical fiber, IEEE Photon. Technol. Lett., vol. 14, no. 11, pp. 1524–1526, Nov 2002.

[56] Candox System Inc., `http://www.candox.co.jp/index.shtml`

[57] HUBER+SUHNER, `https://www.hubersuhner.com/en`

[58] G. Huang *et al.*, Signal processing for high precision phase measurements, in *Proceedings of Beam Instrumentation Workshop (BIW'2010), Santa Fe, New Mexico, US*, TUPSM082, p. 375-378.

[59] Szymon Jablonski, Krzysztof Czuba, Frank Ludwig, and Holger Schlarb, 2π Low Drift Phase Detector for High-Precision Measurements, IEEE Transactions on Nuclear Science, Vol. 62, NO. 3, JUNE 2015, p. 1142-1148.

[60] U. Mavrič *et al.*, Drift Compensation Module for Pulsed or CW Machines at 1.3GHz, 3.0 GHz and 3.9 GHz, in *Poster presentation of Low Level Radio Frequency Workshop 2015 (LLRF'2015), Shanghai, China.*

[61] Frank Ludwig and U. Mavrič, Field detection and Drift calibration for the European XFEL, in *Oral presentation of Low Level Radio Frequency Workshop 2015 (LLRF'2015), Shanghai, China.*

[62] Frank Ludwig *et al.*, Drift calibration for the European XFEL, in *Oral presentation of Low Level Radio Frequency Workshop 2017 (LLRF'2017), Barcelona, Spain.*

[63] Mini-Circuits, `https://ww3.minicircuits.com/homepage/homepage.html`

[64] "Spectral grids for WDM applications: CWDM wavelength grid", *ITU Standard g.694.2*, Dec. 2003.

[65] "Spectral grids for WDM applications: DWDM frequency grid", *ITU Standard g.694.1*, Feb. 2012.

[66] N. Liu *et al.*, Performance evaluation of the RF reference phase stabilization system on fiber-optical link for KEK e-/e+ injector LINAC, in *Proceedings of Linear Accelerator Conference (LINAC'2018), Beijing, China*, MOPO107, pp. 230-232.

[67] Miniature motorized optical variable delay line of General Photonics Corporation, http://www.generalphotonics.com/index.php/product/mdl-002-delay-line/

[68] Variable optical delay line (ODL-340) of Santec Corporation, http://www.santec.com/jp/wp-content/uploads/ODL-340-C-E-v121005.pdf

[69] Piezo-driven fiber stretcher of General Photonics Corporation, http://www.generalphotonics.com/wp-content/uploads/2015/04/FST-001.pdf

[70] Thorlabs Inc., https://www.thorlabs.com/

[71] N. Liu *et al.*, Phase drift compensation between injector linac master oscillator and ring master oscillator for stable beam injection at SuperKEKB, Phys. Rev. Accel. Beams 22, 072002 (2019).

[72] T. Kobayashi *et al.*, LLRF control and master oscillator system for damping ring at SuperKEKB, in *Proceedings of International Particle Accelerator Conference (IPAC'2018), Vancouver, Canada* (JACoW, Vancouver, Canada, 2018), WEPAL001, p. 2137.

[73] T. Matsumoto *et al.*, Low-lever RF system for the SuperKEKB injector LINAC, in *Proceedings of International Particle Accelerator Conference (IPAC'2018), Vancouver, Canada* (JACoW, Vancouver, Canada, 2018), WEPAK017, p. 2132.

[74] H. Hayano, E. Ezura, The RF Reference Line for TRISTAN, in *Proceedings of IEEE Particle Accelerator Conference (PAC'1987), Washington, USA* (JACoW, Washington, USA, 1987), p. 1663.

[75] P.M. Lewis *et al.*, First measurements of beam backgrounds at SuperKEKB, Nucl. Instrum. Methods Phys. Res. A, 914 (2019), pp. 69-144.

[76] Sogo Electric Inc., http://www.sogoel.co.jp/english.html

[77] T. Matsumoto *et al.*, Simultaneous measurement of RF signal and LO signal using direct sampling detection technique, in *Proceedings of 14th Annual Meeting of Particle Accelerator Society of Japan (PASJ'2017), Hokkaido, Japan* (Japan Accelerator Society, Hokkaido, Japan, 2017), TUP063, p. 493.

[78] S. B. Wibowo *et al.*, Digital low level rf control system for the International Linear Collider, Phys. Rev. Accel. Beams 21, 082004 (2018).

[79] L. Doolittle, Digital low-level RF control using non-IQ sampling, in *Proceedings of Linear Accelerator Conference (LINAC'2006), Knoxville, USA* (JACoW, Knoxville, USA, 2006), THP004, p. 568.

[80] T. Miura *et al.*, Phase shifter for RF reference signal in SuperKEKB injector LINAC, in *Proceedings of 15th Annual Meeting of Particle Accelerator Society of Japan (PASJ'2018), Nagaoka, Japan* (Japan Accelerator Society, Nagaoka, Japan, 2018), THP106, p. 1136.

[81] T. Kobayashi *et al.*, RF reference distribution system for the 400-MeV proton linac of the KEK/JAERI joint project, in *Proceedings of Linear Accelerator Conference (LINAC'2002), Gyeongju, Korea* (JACoW, Gyeongju, Korea, 2002), MO463, p. 187.

[82] J. Mizuno *et al.*, A New FPGA Board with Fast ADCs for Direct RF Sampling, in *Proceedings of 8th Annual Meeting of Particle Accelerator Society of Japan (PASJ'2011), Tsukuba, Japan* (Japan Accelerator Society, Tsukuba, Japan, 2011), MOPS106, p. 609.

[83] T. Miura *et al.*, Low-level RF system for cERL, in *Proceedings of International Particle Accelerator Conference (IPAC'2010), Kyoto, Japan* (JACoW, Kyoto, Japan, 2010), TUPEA048, p. 1441.

[84] N. Iida *et al.*, Design of the positron transport system for SUPERKEKB, in *Proceedings of International Particle Accelerator Conference (IPAC'2010), Kyoto, Japan* (JACoW, Kyoto, Japan, 2010), THPD004, p. 4284.

Acknowledgments

I would like to thank everyone who supported me during my Ph.D. study. First, I thank my supervisor Takako Miura. She considerably supported my topic and gave me several opportunities to study abroad. Second, I thank Toshihiro Matsumoto for his advise and encouragement. The in-depth discussion with him were the source of valuable insights. I would also like to thank Shinichiro Michizono for his helpful suggestions. Finally, I thank Feng Qiu for the invitation to apply for the Ph.D course at KEK. His support made my study in Japan possible.

From the DESY MSK group, I would like to thank Mathieu Omet for the opportunity of a long-term internship at DESY. I also thank Holger Schlarb, Uros Mavric, Frank Ludwig, Heinz Pryschelski, Thorsten Lamb, and Julien Branlard for their support on my research and ensuring that I had a good time during my stay at Hamburg, Germany.

I thank all my colleagues, Baiting Du, Muhammad Abdul Rahman, and Di Wang, and friends for their support during my stay in Japan.

I am thankful to my family for always encouraging and understanding me, and especially my husband, for his continued support and thoughtful kindness.

Na Liu

Declaration

I declare that I wrote this preliminary Ph.D. thesis independently and without any other references and resources than stated in the bibliography.

Tsukuba, September 2019